



T.C.

ULUDAĞ UNIVERSITY

INSTITUTE OF NATURAL AND APPLIED SCIENCE

MUON BACKGROUND STUDIES FOR CLIC BEAM DELIVERY SYSTEM

Fatma Belgin PİLİÇER

Asst. Prof. Zerrin KIRCA

(Supervisor)

Ph. D. Thesis

DEPARTMENT OF PHYSICS

BURSA – 2017

All rights reserved

APPROVEL OF THE THESIS

This work named "Muon Background Studies for CLIC Beam Delivery System" by Fatma Belgin PİLİÇER has been approved as a dissertation for the degree of **Doctor of Philosophy in Physics Department, Uludağ University** by the below mentioned Examining Committee Members.

Supervisor: Asst. Prof. Zerrin KIRCA

Head: Asst. Prof. Zerrin KIRCA
Uludağ University, Science-Art Faculty,
Physics Department

Signature


Member: Prof. Serkant Ali ÇETİN
Bilgi University, Faculty of Engineering and Natural Sciences,
Department of Energy Systems Engineering

Signature


Member: Assoc. Prof. Bilgen OSMAN
Uludağ University, Science & Art Faculty,
Chemistry Department

Signature


Member: Assoc. Prof. Cem Salih ÜN
Uludağ University, Science & Art Faculty,
Physics Department

Signature


Member: Asst. Prof. Oktay CEBECİOĞLU
Kocaeli University, Science & Art Faculty,
Physics Department

Signature




Approved

Prof. Ali BAYRAM
Institute Director

.. / .. / ...

I declare that this thesis follows the thesis preparation rules of Uludağ University Institute of Natural and Applied Science. I hereby declare that

- all information in this document has been obtained in accordance with academic rules
- all visual, audial and written information and results have been presented in academic ethical rules,
- all citations and materials have been referenced as required by academic rules,
- all cited materials have been presented as reference
- used sources and materials have not been altered
- this thesis has not been submitted for any degree or any other purposes.

.. / .. /

Signature

Fatma Belgin PİLİÇER

ÖZET

CLIC DEMET TAŞINIM HATTI İÇİN MUON ARD ALAN ÇALIŞMALARI

Doktora Tezi

Fatma Belgin PİLİÇER

Uludağ Üniversitesi

Fen Bilimleri Enstitüsü

Fizik Anabilim Dalı

Danışman: Yrd. Doç. Zerrin KIRCA

Kompakt Doğrusal Çarpıştırıcı (Compact Linear Collider - CLIC) yüksek hassasiyette sahip olup kütle merkezi enerjisi TeV mertebesine ulaşılması planlanan, elektron ve pozitronları çarpıştırmak amacıyla tasarlanan bir makinedir. CLIC projesi bilinen ve yeni fizik süreçleri hakkında yüksek hassasiyetlerde ölçümlere olanak sağlayacaktır. Temiz ve hassas ölçümler yapabilmek için en önemli husus ard alanların ortadan kaldırılmasıdır. Algıç ölçümlerini ve veri analizlerini etkileyen çeşitli ard alan kaynakları bulunmaktadır. Bu ard alan kaynaklarından birisi de demet taşınım hattı (DTH) boyunca oluşan müonlardır. Bu tezde öncelikle müon ardalanı oluşumuna sebep olan demet etrafındaki hale parçacıklarının miktarları hesaplanmış ve ardalan oluşturan müonların oluşum mekanizmaları incelenmiş ve benzetişimleri yapılmıştır. Ardından DTH hattı ve hatta yeralan elemanlar incelenip analiz edilerek BDSIM (Beam Delivery SIMulation) ile benzetişimi yapılmıştır. Hale parçacıklarının miktarları ile orantılı olarak hat boyunca oluşan ard alan müonların oluşum noktaları enerjileri gibi parametreler belirlenmiştir. Son olarakta oluşan müonları azaltarak etkileşme bölgesine ulaşmalarını engellemek için manyetik alanlı müon zırhları dizayn edilerek hat boyunca belirlenen uygun bölgelere yerleştirilmiş ve etkileşme bölgesine ulaşan müon miktarlarındaki azalma incelenmiştir. Farklı manyetik alanlar ve farklı kalınlıklar için müon zırhları belirlenmiş ve müon miktarlarındaki azalmalar karşılaştırılmıştır.

Müon ard alanının temel sebebi demet etrafında oluşan hale parçacıklarıdır. Ana demetin etrafındaki hale parçacıkları betatron kolimasyon bölgesinde saçıcılar yardımı ile soğuruculara yönlendirilerek soğurulurken, elektromanyetik süreçlerle ikincil parçacık olarak müon oluşumuna sebep olurlar. Oluşan yüksek enerjili müonların durdurulması oldukça zordur ve oluşan müonların betatron kolimasyonu bölgesinden etkileşme bölgesine doğru hareket etmesi algıç bölgesinde istenilmeyen bir ard alan oluşumuna sebep olmaktadır. Algıcın çeşitli bölgelerine ulaşan müonlar, iz algıcı kısmında iş yükünü (occupancy) arttırabilir ve/veya kalorimetre bölümünde enerji çözünürlüğünü etkileyerek incelenmek istenen süreci perdeleyen etkili bir ard alan oluşturabilirler. Bu sebeple, müon ard alanı ortadan kaldırılmalı veya makul seviyelere düşürülmelidir.

Hale parçacıklarının oluşumunun çeşitli sebepleri vardır. Ancak bilinen en baskın süreç demet-gaz saçılmalarıdır. Demet-gaz saçılmalarının, Dr. Helmut Burkhardt tarafından yazılan HTGEN adlı kod ile benzetişimi yapılarak, hale parçacıklarının miktarı ve dağılımı

hakkında hesaplamalar yapılmıştır. Bunun yanında müon oluşum süreçleri GEANT4 kodu ile detaylı olarak incelenmiştir. HTGEN ile elde edilen hale parçacıkları dağılımları BDSIM adlı programda girdi dosyası olarak kullanılmış ve bu hale parçacıklarının DTH boyunca takibi yapılmıştır. Müonların etkileşme bölgesine ulaşma oranları incelenmiştir. Etkileşme bölgesine ulaşan müon miktarlarını azaltmak için toroidal manyetik alanlı müon zırhları kullanılmış ve müonlar tünel duvarlarına doğru saptırılmıştır. Farklı müon zırh parametreleri için müon azalma oranları detaylı bir şekilde incelenmiştir.

Tezin ilk bölümünde CLIC projesinin araştıracağı fizik hakkında kuramsal temeller, hızlandırıcı, DTH ve algıç kısımları ile ilgili genel bilgiler verilmiştir. 2. Bölümde, doğrusal çarpıştırıcıların optik elemanları ve hale oluşum mekanizmaları hakkında detaylı bilgi verilmektedir. 3. bölümde ise hale ve müon oluşum süreçleri için yapılan benzetişimler ve hesaplamalar verilmiştir. Son olarak, 4. Bölümde ise hesaplanan müon miktarları ve azalma oranları, daha önce yapılan çalışmalar ile karşılaştırılarak sonuçlar detaylı şekilde incelenmiştir. Bu doktora tezi, DTH boyunca oluşan müon ard alanlarına ve bunların istenilen oranlara azaltılması konusuna odaklanmıştır. CLIC Kavramsal Tasarım Raporunda (Conceptual Design Report - CDR) belirtilen DTH hattı detaylı olarak incelenmiştir. Öncelikle müon oluşum mekanizmaları belirlenmiştir. Müon ard alanı potansiyeli Monte Carlo tabanlı benzetişim programları ile öngörülmüştür. Müon ard alanının azaltılması için manyetik alanlı müon zırh yapılarının kullanılması planlanmıştır. Manyetik alanlı zırhların parametreleri (uzunluk, iç yarıçap, dış yarıçap, manyetik alan ... gibi) belirlenmiştir. DTH üzerinde herhangi bir değişiklik yapılmadan betatron kolimasyon bölgesinde uygun bölgelerdeki sürüklenme boruları etrafına yerleştirilmiştir. Farklı zırh seçenekleri incelenmiş ve müon azalma oranları detaylı olarak birbirleriyle karşılaştırılmıştır.

Anahtar Kelimeler: CLIC, hale parçacıkları, müon ard alanı, BDSIM, manyetik alanlı zırh

2017, xv + 77 sayfa

ABSTRACT

MUON BACKGROUND STUDIES FOR CLIC BEAM DELIVERY SYSTEM

PhD Thesis

Fatma Belgin PİLİÇER

Uludağ University

Graduate School of Natural and Applied Sciences

Department of Physics

Supervisor: Asst. Prof. Zerrin KIRCA

The Compact Linear Collider (CLIC) is being designed to be a high precision machine for colliding beams of electrons with positrons at the TeV energy scale. The CLIC project provides high precision measurements about known and new physics processes. In order to perform clean and precise measurements, it is essential to minimize and understand backgrounds. There are several background sources which effect the analysis of data and detector measurements. One of the important background sources are muons, which are generated along the beam delivery system (BDS), for the detector performance.

The main source of the muon background is the halo particles. These particles have large amplitude, and they are generated around the core beam along the BDS. Among several possible reasons for halo particle generation are optics and equipment related effects which depend on imperfections which are hard to predict and should be small in a well corrected machine. The estimates presented here are based on the halo generation by beam-gas scattering which will always be there and for which good theoretical models exist. The halo generation by beam-gas scattering has been estimated using the HTGEN code (Halo and Tail Generation). Depending on the halo particle estimation, muon background along the BDS and especially in the betatron collimation section have been determined by using Monte Carlo simulation codes.

This Ph.D thesis focuses on the muon background along the BDS and the reduction of them to desired rates. The detailed studies described here are based on the BDS design as described in the Conceptional Design Report of CLIC. The muon background rates that reach the CLIC detector region are predicted using tracking simulations. The muon production mechanisms and their Monte Carlo generation are studied and described in detail. A significant reduction of muon backgrounds can be achieved using magnetized shielding. The shielding blocks can be placed in available drift spaces in the betatron collimation section. The dependence on the muon reduction on the main shielding parameters like length, inner and outer shielding dimension and magnetic field properties have been studied and are described.

Key Words: CLIC, halo particles, muon background, BDSIM, magnetized muon shielding
2017, xv + 77 pages



ACKNOWLEDGEMENTS

First of all, I would like to thank to my supervisor Asst. Prof. Zerrin KIRCA and Prof. İlhan TAPAN for their continuous support and for giving me a great opportunity to be involved in the CLIC project at CERN. I would like to thank all my collaborators at CLIC but especially to Dr. Helmut BURKHARDT for accepting me as a PhD student and spending his valuable time with me to make this study possible. I would also like to thank Dr. Daniel SCHULTE, Dr. Lau GATIGNON, Dr. Konrad ELSENER, Dr. Michele MODENA and Dr. Alexander ALOEV for their valuable discussions and support during my studies at CERN. Also, special thanks to BDSIM developers; Dr. Johem SNUVERICK, Laurie NEVAY and other colleagues since they have an important role about BDSIM problems.

I would like to thank to Prof. Ömer YAVAŞ and TAEK to give me an opportunity to take part of TAEK-CLIC project with Uludağ University group. Additionally, I acknowledge to TÜBİTAK to financially support me during my PhD research (BİDEB 2214- PhD Research Fellow Program).

I would like to thank the rest of my thesis examining committee: Assoc. Prof. Cem Salih ÜN, Assoc. Prof. Bilgen OSMAN, Prof. Serkant Ali ÇETİN, Asst. Prof. Oktay CEBECİOĞLU for their valuable reviews.

I would like to thank my friends especially Dr. Rob VEENHOF, Dr. Adriana MİLİĆ for their encouragements and supports during my studies at CERN.

Last but not least, I would like to thank my parents and brother for their supports during my education. Also, special thanks to my husband Ercan PİLİÇER for his endless support and love. He always has suffered with me during my thesis and has always believed in me.

CONTENTS

	Page
ÖZET	iv
ABSTRACT	vi
ACKNOWLEDGEMENTS	viii
LIST OF FIGURES	xii
LIST OF TABLES	xiii
LIST OF SYMBOLS	xiv
LIST OF ABBREVIATIONS	xv
1. INTRODUCTION	1
1.1. Physics Potentials of CLIC	1
1.2. Compact Linear Collider (CLIC) Accelerator Concept	4
1.2.1. Beam Delivery System	5
1.3. CLIC Detector Concept	7
1.4. Scope of This Thesis	8
2. THEORY	10
2.1. Linear Beam Dynamics	10
2.2. Matrix Elements	12
2.3. Particle Beams and Phase Space	16
2.4. Halo Particles and Generation Mechanisms	20
2.4.1. Particle Related Processes	21
2.4.2. Beam - Gas Inelastic Scattering	24
2.4.3. Processes Related to Optics	25
2.4.4. Other Processes	26
3. ANALYSIS	27
3.1. Simulations of Halo Particles	27
3.2. Muon Production Mechanisms at High Energies	30
3.2.1. Bethe - Heitler Muon Pair Production Process	32
3.2.2. Electron-Positron Annihilation into Muon Pairs	34
3.2.3. Annihilation into Hadrons	38
4. SIMULATION RESULTS	43
4.1. CLIC Beam Delivery System Simulation	43
4.2. Tracking and Optics	45
4.3. Muon Tracks in BDS	48
4.4. Optimization of Magnetized Muon Shielding	53
4.5. Muon Sweeping	58
5. CONCLUSION	64
REFERENCES	66
APPENDICES	72

APPENDIX 1	73
APPENDIX 2	74
CURRICULUM VITAE	76



LIST OF FIGURES

		Page
Figure 1.1	LHC run schedule	2
Figure 1.2	The three highest Higgs boson production mechanisms; Higgsstrahlung process, W^+W^- fusion process and radiation off top quarks.	3
Figure 1.3	The cross section of Higgs production channels with respect to center of mass energies for CLIC collision energy scale [Abramowicz et al 2013]	3
Figure 1.4	Possible location of CLIC complex	4
Figure 1.5	Acceleration System Layout of the CLIC	5
Figure 1.6	Layout of CLIC Beam Delivery System.	6
Figure 1.7	CLIC detector layout	8
Figure 2.1	Overlapping trajectories of several particle while traversing in quadrupoles on the diagnostic section	15
Figure 2.2	Courant Snyder ellipse parameters in phase space [Wiedemann 2007]	17
Figure 2.3	Betatron functions for diagnostic section on BDS	18
Figure 2.4	Betatron and dispersion functions through the BDS	19
Figure 2.5	Schematical representation of halo and core beam	20
Figure 2.6	Match conditions in phase space from left to right; mismatch, perfect match and efficient match	25
Figure 3.1	The estimated halo particles (red) and core beam (green) along the BDS	28
Figure 3.2	The distribution of halo particles at YSP1	29
Figure 3.3	Schematics of pair production and Bremsstrahlung mechanisms	30
Figure 3.4	Cross sections of the muon production processes with respect to incident beam energy up to 1500 GeV	31
Figure 3.5	Schematic representation of muon production process with electromagnetic interaction	32
Figure 3.6	Energy distribution of muons which are produced with GammaToMuPair process	33
Figure 3.7	Angular distribution of muons for different photon energies	34
Figure 3.8	Diagram of annihilation into muon process	34
Figure 3.9	Helicity state of a spin -1/2 particle. The arrows with p represent the direction of motion of the particle and s_p shows spin of the particle	36
Figure 3.10	Schematic representation of the one of the helicity combination for the $e^+e^- \rightarrow \mu^+\mu^-$ process	36
Figure 3.11	Energy distribution of muons from GammaToMuPair and AnnihiToMuPair process for 1.5 TeV electron and positron beam	38
Figure 3.12	The cross section of annihilation into hadrons ($e^+e^- \rightarrow \text{hadrons}$) process with respect to center of mass energy values	39
Figure 3.13	Hadron production processes and change in their cross section \sqrt{s}	40

Figure 3.14	The ratio of cross sections as a function of center of mass energy. .	42
Figure 3.15	The cross section ratio values $R = (e^+e^- \rightarrow hadrons, s) / (e^+e^- \rightarrow \mu^+\mu^-, s)$ collected from the world wide experiments [Olive et al 2014]	42
Figure 4.1	A part of BDS geometry which have been generated with BDSIM	44
Figure 4.2	Comparison of horizontal and vertical RMS beam size results obtained from MAD-X and BDSIM along the beamline	46
Figure 4.3	Estimated particles trajectories along the BDS by using BDSIM .	47
Figure 4.4	Schematics of the spoiler and absorber couple in betatron collimation section	48
Figure 4.5	Sample muon tracks which are generated by hitting to the first spoiler YSP1 through the beamline	49
Figure 4.6	The origin of muons from betatron collimation section to end of BDS and their creation process	50
Figure 4.7	Energy distribution of of the generated muons	51
Figure 4.8	The amount of muons along the BDS	52
Figure 4.9	The comparison of the amount of muons in BDS for both case artificial hitting to first spoiler (green error bars) and using HTGEN distribution at first spoiler (red error bars)	52
Figure 4.10	The schematic of the magnetized muon shielding which has a toroidal magnetic field	53
Figure 4.11	Schematic of the deflected muons from magnetized shielding . . .	55
Figure 4.12	The amount of deflection (left) and deflection angle (right) depending on incident muon energy and magnetic field of shielding . . .	55
Figure 4.13	Changes in magnetic field for different number of Sm-Co (Samarium-Cobalt) blocks [Aloev et al 2016, Aloev et al 2015]	57
Figure 4.14	Magnetic field changes for normal conducting magnet option [Aloev et al 2016, Aloev et al 2015]	58
Figure 4.15	The layout of spoilers, absorbers and magnetized shielding for different options	59
Figure 4.16	Muon fluxes for 0.7 T magnetized shielding when halo particles hit to the first spoiler	60
Figure 4.17	Muon fluxes for 1.2 T magnetized shielding when halo particles hit to the first spoiler	61
Figure 4.18	Muon fluxes for 0.7 T magnetized shielding when halo distribution, which is generated with HTGEN, is used.	63
Figure 4.19	Muon fluxes for 1.2 T magnetized shielding when halo distribution, which is generated with HTGEN, is used.	63

LIST OF TABLES

	Page
Table 1.1	Geometrical description of spoilers and absorbers on BDS. 6
Table 1.2	Main parameters of CLIC acceleration system 7
Table 2.1	Total cross section values evaluated for Bremsstrahlung and Mott Scattering processes 24
Table 3.1	Generated mesons properties 40
Table 3.2	Lifetime of the generated hadrons from $e^+e^- \rightarrow$ hadrons process . 41
Table 3.3	Determined decay distance of generated hadrons from $e^+e^- \rightarrow$ hadrons process 41
Table 4.1	Some parameters about spoilers and absorbers 48
Table 4.2	The estimated amount of muons reaching to the end of BDS de- pending on the magnetized muon shielding parameters by using artificial hit to the YSP1 61
Table 4.3	The estimated amount of muons reaching to the end of BDS de- pending on the magnetized muon shielding parameters by using halo distribution 62

LIST OF SYMBOLS

Symbol	Description
c	Speed of Light
\mathcal{L}	Luminosity
E	Energy
\sqrt{s}	Center of mass energy
\mathbf{k}	Magnetic gradient
k_B	Boltzmann constant
\hbar	Planck's constant
s_0	Initial trajectory in phase space
\mathbf{s}	Trajectory in phase
ϵ	Emittance
ϵ_N	Normalize emittance
θ_{min}	Minimum scattering angle
σ_{mott}	Mott scattering total differential cross section
γ	Lorentz factor
$\beta_{x,y}$	Betatron function for x, y axis
β	Relativistic velocity
M_{QF}	Matrix element of focusing magnet
M_{QD}	Matrix element of defocusing magnet
n_p	Number of photon
$\sigma_{compton}$	Compton scattering total cross section
E_{cms}	Center of mass energy
α	Fine structure constant
r_e	Electron radius
σ_{brems}	Bremsstrahlung cross section

LIST OF ABBREVIATIONS

Abbreviation	Description
BDS	Beam Delivery System
BDSIM	Beam Delivery Simulation
CDR	Conceptional Design Report
CERN	European Organization for Nuclear Research
CLIC	Compact Linear Collider
CLIC-SiD	CLIC - Silicon Detector
CLIC-ILD	CLIC - International Linear Detector
FCC	Future Circular Collider
GEANT4	Geometry And Tracking
HL LHC	High Luminosity Large Hadron Collider
HTGEN	Halo and Tail Generation
IR	Interaction Region
LHC	Large Hadron Collider
MAD	Methodical Accelerator Design
MDI	Machine Detector Interface
TAC	Turkish Accelerator Center
TPC	Time Projection Chamber
PDG	Particle Data Group
PETRA	Positron Electron Tandem Ring Accelerator
PLACET	Program for Linear Accelerator Correction Efficiency Tests
SLAC	Stanford Linear Accelerator

1. INTRODUCTION

Large Hadron Collider (LHC) is a circular accelerator built in a tunnel of 27 km circumference with a varying depth up to 175 m underground. The LHC started its first operation in 2010 by colliding the proton beams of the order of 7 TeV center of mass energy (Run1). In May 2015, the LHC Run2 approximately doubled the energy of Run1 and increased luminosity in order to make more precise measurements and provide better understanding for properties of the Higgs boson. For Run2, the center of mass energy is 13 TeV for the proton beams circulating around the LHC storage ring. For Run3, the center of mass energy is planned to be 14 TeV but the luminosity increases up to $3 \times 10^{34} \text{ cm}^{-2}\text{s}^{-1}$, so it is called High Luminosity - Large Hadron Collider (HL - LHC). After Run3, as shown in Figure 1.1, HL-LHC, by further increase in luminosity from 300 to 3000 fb^{-1} , is planned to run to extend the LHC discovery potential [HL 2016, Butler et al 2015]. Besides the circular collider as LHC, linear colliders are also important to provide high-precision and clean measurements, which are of special importance in new physics studies beyond the Standard Model (BSM). The main advantage of linear collider is to avoid the energy loss of the beams due to the synchrotron radiation which is critical in stabilizing beams. The other perspectives about the advantages of the linear colliders can be found in references [Murayama 1995, Murayama and Peskin 1996, Lukić 2015, Aicheler et al 2012] with an extensive discussion.

1.1. Physics Potentials of CLIC

The Compact Linear Collider (CLIC) project, which will be about 40 km long accelerator system, have been planned to be build at CERN to collide electron and positron beams. The center of mass energy of the collision range are extended from a several hundred GeV to 3 TeV. The lower energy levels are important for the high accuracy measurements of Higgs (125GeV) and top quarks. The higher center of mass energy levels like 1.5 TeV are essential in searching of the new physics phenomena BSM [Aicheler et al 2012]. The

2010				2011				2012				2013				2014				2015				2016				2017				2018				2019			
1	2	3	4	1	2	3	4	1	2	3	4	1	2	3	4	1	2	3	4	1	2	3	4	1	2	3	4	1	2	3	4	1	2	3	4	1	2	3	4
Run 1 7-8TeV, 0.7×10^{34} ($\mu \sim 20$), 25 fb^{-1}												Long shutdown 1				Run 2 13 – 14 TeV, 1.6×10^{34} ($\mu \sim 43$), 150 fb^{-1}												Long shutdown 2 Phase-I install											

2020				2021				2022				2023				2024				2025				2026				2027				2028				2029			
1	2	3	4	1	2	3	4	1	2	3	4	1	2	3	4	1	2	3	4	1	2	3	4	1	2	3	4	1	2	3	4	1	2	3	4	1	2	3	4
Run 3 14 TeV, $2-3 \times 10^{34}$ ($\mu \sim 50-80$), 350 fb^{-1}												Long shutdown 3 Phase-II install				HL-LHC – Run 4 14 TeV, $5 - 7 \times 10^{34}$ ($\mu \sim 140 - 200$), 3000 fb^{-1}												Long shutdown 4											

2030				2031				2032				2033				2034				2035							
1	2	3	4	1	2	3	4	1	2	3	4	1	2	3	4	1	2	3	4	1	2	3	4				
Run 5 14 TeV, $5 - 7 \times 10^{34}$, 3000 fb^{-1}												Long Shutdown 5				Run 6 14 TeV, $5 - 7 \times 10^{34}$, 3000 fb^{-1}											

Figure 1.1. LHC run schedule

work plan of CLIC strongly depends on the results about the Higgs boson from LHC at 14 TeV. Feynmann diagrams for the three highest Higgs boson production mechanisms are represented in Figure 1.2.

At lower center of mass energy stages like 240 GeV Higgsstrahlung process

$$e^+ + e^- \rightarrow Z + H \quad (1.1)$$

starts to dominate. Z is detected in best way by $\mu^+ \mu^-$ decay at tracker part of the detector.

Increasing the center of mass energy $W^+ W^-$ fusion process

$$e^+ + e^- \rightarrow H + \nu_e + \bar{\nu}_e \quad (1.2)$$

becomes significant. $W^+ W^-$ fusion is dominant for $\sqrt{s} > 350 \text{ GeV}$ and it provides accurate measurements of cross section for different decay modes like $\tau\tau$, $\mu\mu$ and qq . The other Higgs boson production processes with respect to the center of mass energy are represented in Figure 1.3.

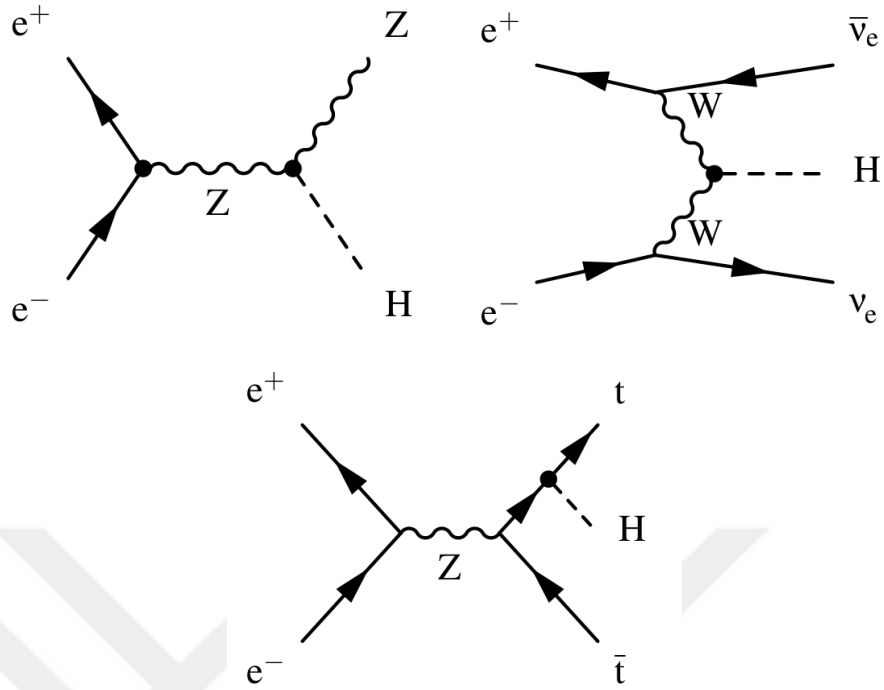


Figure 1.2. The three highest Higgs boson production mechanisms; Higgsstrahlung process, W^+W^- fusion process and radiation off top quarks.

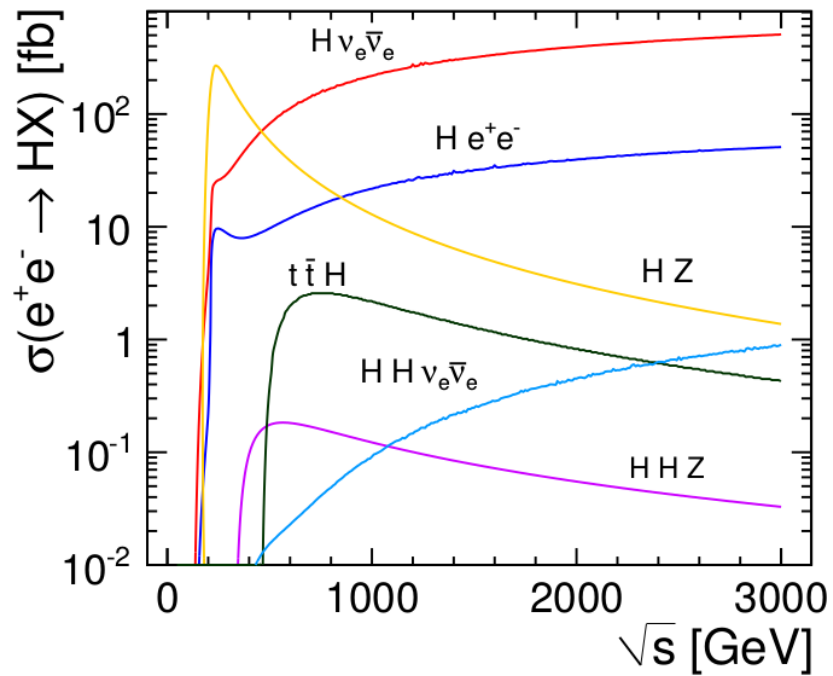


Figure 1.3. The cross section of Higgs production channels with respect to center of mass energies for CLIC collision energy scale [Abramowicz et al 2013]

Higgsstrahlung process is essential for Higgs boson mass and cross section measurements for e^+e^- interactions. For this process, Higgs boson properties are measured by the reconstruction of the tracks of the lepton anti-lepton pairs in tracker detector. This process is generally shown as $Z \rightarrow e^+e^-/\mu^+\mu^-$.

The process $e^+e^- \rightarrow t\bar{t}H$ is crucial to measure the Yukawa which describes the coupling strength between the Higgs boson and massless quark and electron fields. This process can be measured at $\sqrt{s} > 700$ GeV energies. In this process, Yukawa coupling is planned to measure within about 4.5% uncertainty at 1.4 TeV energy range while the Higgs boson decays through $b\bar{b}$ channel [Abramowicz et al 2013].

1.2. Compact Linear Collider (CLIC) Accelerator Concept

CLIC will provide high luminosity with an innovative two-beam acceleration scheme. The possible location of the CLIC acceleration complex are shown as in Figure 1.4 [Boland et al 2016], and infrastructure of the acceleration complex has been schematically given in Figure 1.5.

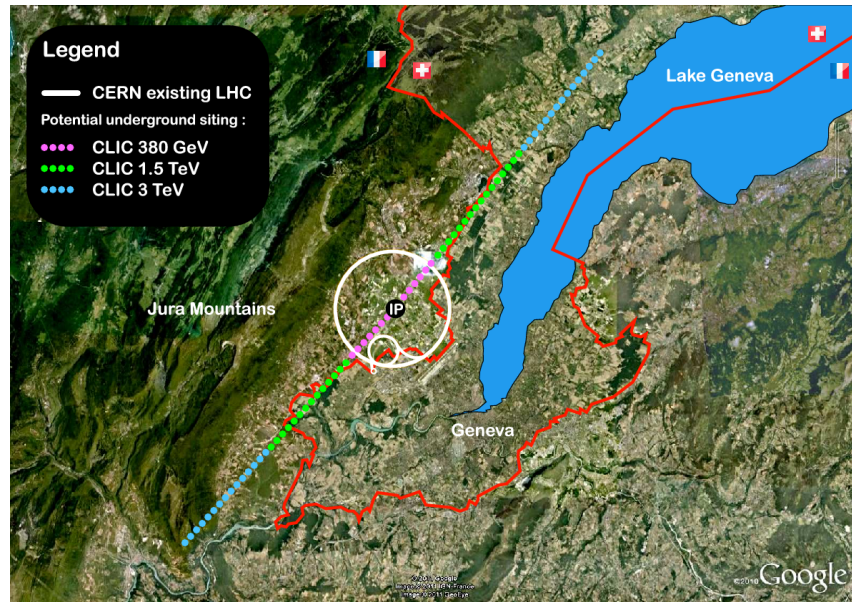


Figure 1.4. Possible location of CLIC complex

The main beams are generated as conventional electron and positron sources. To reduce

emittance, they enter pre-damping and damping rings as shown in the bottom side of Figure 1.5 [Aicheler et al 2012, Boland et al 2016]. The beams, which are accelerated from the rings to the Main Linac, reach up to 9 GeV. The Main Linac uses an RF frequency of 12 GHz with 100 MV/m cavity structures to accelerate the beam to higher energies. The Main Linac Acceleration is provided by the Drive Beam which is powered by klystrons. At the end of the Linac, the beam is transported to the interaction region through the BDS.

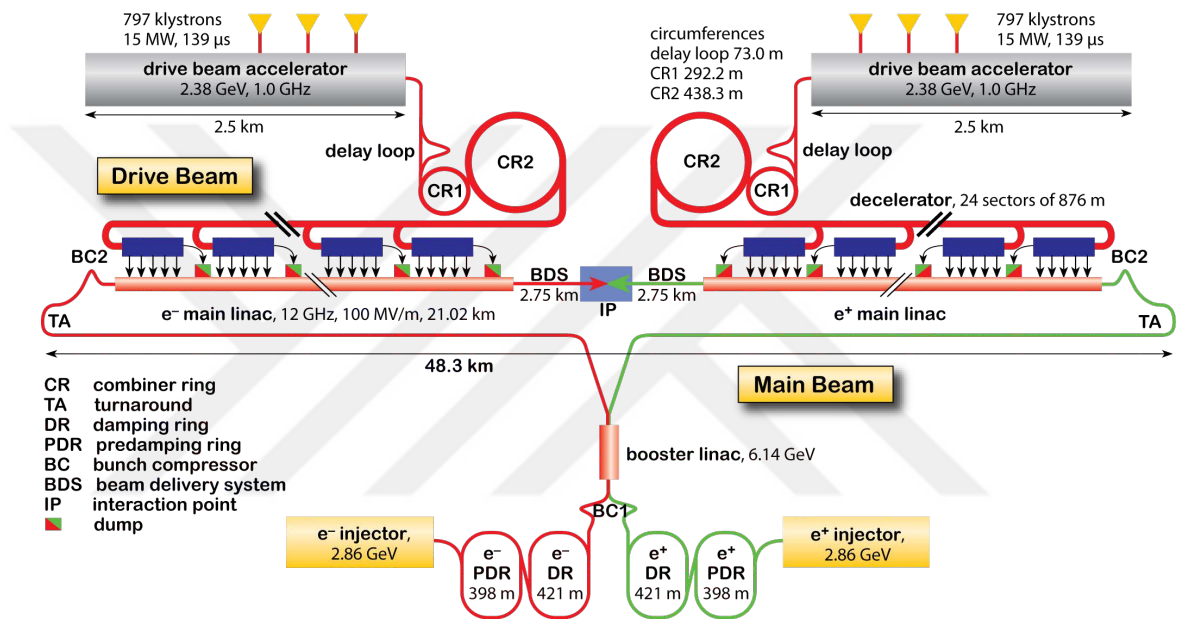


Figure 1.5. Acceleration System Layout of the CLIC

1.2.1. Beam Delivery System

Rather being accelerated, the beams in the BDS are only transported to the interaction region (IR) by removing unwanted beams and backgrounds, and focusing them to the required size. The BDS is about 2800 m long and consists of three main sections which are namely diagnostic, collimation and final focus.

The beam enters the linac and reaches the diagnostic section of the BDS. The beam properties are measured and corrected before it enters to the collimation section. The second section is the energy collimation part to remove off-momentum particles which spread over the tails of momentum plots. When the beam particles reach the betatron

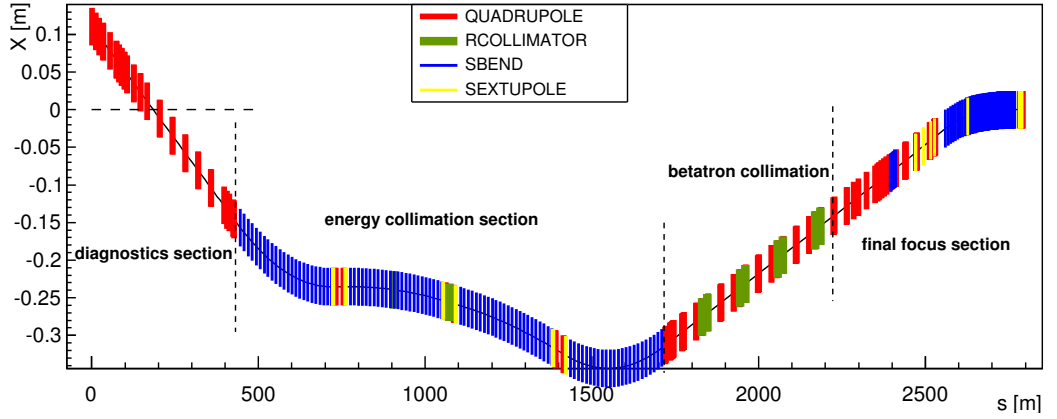
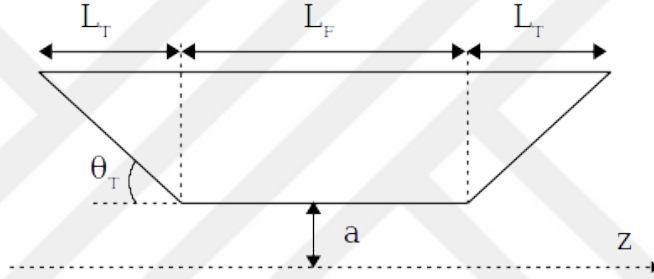


Figure 1.6. Layout of CLIC Beam Delivery System.

Table 1.1. Geometrical description of spoilers and absorbers on BDS.



Name	a_x [mm]	a_y [mm]	θ_T [mrad]	L_F [X_0]	L_T [X_0]	Mat.
YSP 1, 2, 3, 4	8	0.1	88	0.2	90	Ti-Cu
XSP 1, 2, 3, 4	0.12	8	88	0.2	90	Ti-Cu
XAB 1, 2, 3, 4	1	1	250	18	27	Ti
YAB 1, 2, 3, 4	1	1	250	18	27	Ti

collimation section, halo particles around the core beam are removed by the collimators placed in this section. Betatron collimation section is made of four sets of horizontal and vertical spoilers and absorbers whose geometrical description is given in Table 1.1. The betatron collimation section has a critical role since it preserves the downstream of the beam line from the unwanted halo particles which are either coming from the Main Linac or generated in the diagnostic and energy collimation sections [Aicheler et al 2012].

The last part of the BDS is final focus section. It contains strong magnets in order to focus the beam to obtain the required parameters. The beam is almost parallel when it reaches the final strongest doublet at the end of the final focus section and it is focused horizontally

Table 1.2. Main parameters of CLIC acceleration system

Parameter	Symbol	Value	Unit
Center-of-mass energy	E_{cms}	3000	GeV
Main Linac RF frequency	f_{rf}	11.994	GHz
Luminosity	L	5.9	$10^{34} \text{cm}^{-2} \text{s}^{-1}$
No. of particles / bunch	N	3.72	10^9
No. of bunches / pulse	N_b	312	
Bunch separation	δt_b	0.5 (6 periods)	ns
Bunch train length	τ_{train}	156	ns
Beam power / beam	P_b	14	MW
Overall two linac length	l_{linac}	42.16	km
Total beam delivery length	l_{BD}	2×2.75	km
Proposed site length	l_{tot}	48.4	km
Total site AC power	P_{tot}	582	MW
Wall-plug-to-Main-Beam-power efficiency	η_{tot}	4.8	%

to ~ 40 nm and vertically to ~ 1 nm by the strong quadrupole of the BDS. The optics layout of the BDS is shown in Figure 1.6.

1.3. CLIC Detector Concept

In addition to accelerating the beams to higher energies and colliding them, there is another crucial point which is the particles in the CLIC detector environment should be detected effectively and the huge data recorded through these collision events should be evaluated adequately [Linssen et al 2012]. The Conceptual Design Report (CDR) is based on two different detector models CLIC_ILD and CLIC_SiD with a push-pull option. These detectors mainly consist of the same parts except for their tracking detector systems. CLIC_ILD includes silicon trackers as a vertex detector but as an outer tracker it uses a gaseous detector (Time Projection Chamber (TPC)). CLIC_SiD is designed with silicon pixel and strip detectors for both inner and outer tracker parts.

CLIC will be operated with $5.9 \times 10^{34} \text{cm}^{-2} \text{s}^{-1}$ total luminosity for 3 TeV center of mass energy [Linssen et al 2012]. The other parameters about the CLIC acceleration part have been presented in Table 1.2 [Aicheler et al 2012]. In the bunch structure, each pulse contains 312 bunches and each bunch is made of 3.79×10^9 particles. The time interval

between each bunch is about 0.5 ns. This results in very short and frequent bunch crossings during the operation. Due to bunch properties and other reasons, the CLIC_SiD will be chosen instead of both detectors [Elsener 2015]. On the other hand, the CLIC_ILD concept is still an option for ILC project in Japan due to its long bunch length property. The silicon tracker based CLIC detector optimization studies are currently ongoing. The schema of the last proposed detector model is shown in Figure 1.7 [Siegrist, N. and Gerwig H. 2015].

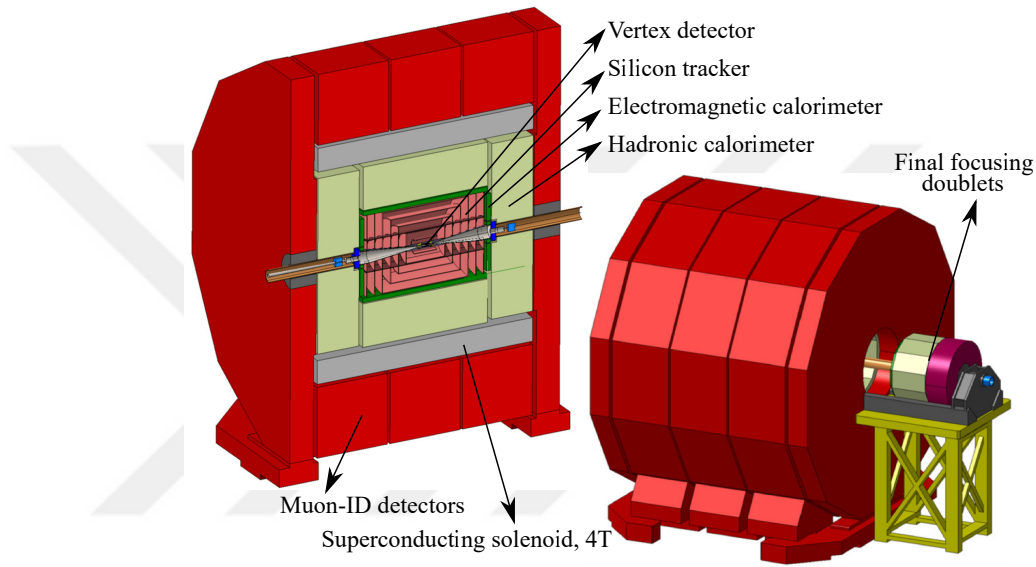


Figure 1.7. CLIC detector layout

1.4. Scope of This Thesis

The aim of this thesis is to evaluate the muon background in the BDS of the CLIC project. The source of the muon background in the BDS comes from halo particles. Therefore the phenomenon of the beam halo is of crucial importance. Halo particles are beam particles but they travel around the core beam due to various reasons. They are mainly removed from the core beam in collimator sections. Beam halo particles create muons as secondary particles with electromagnetic processes mostly around the absorbers in BDS. The important point is that the muons can reach the detector side and principally cause dangerous background by increasing occupancies in the tracker part and effect energy resolution in the calorimeter part. Because of these reasons, the muon background have to

be eliminated or reduced to a reasonable amount.

There are various reasons for halo formation but the well-known dominant process is beam-gas scattering. The beam-gas scattering processes are investigated with HTGEN by Helmut Burkhardt [Ijaz Ahmed 2008]. The results are used in BDSIM [Agapov et al 2006] as a source file and tracked along BDS. The muon generation processes are tracked with GEANT4 Monte Carlo simulation code. For the reduction of muons, magnetized shielding is used and the reduction rate is evaluated in detail for the various cases. The results are discussed with the experts at CERN, on the detector side by Konrad Elsener, and Machine Detector Interface (MDI) and magnet side by Lau Gatignon, Michele Modena, Alexander Alov and others.

This thesis is organized as follows; first chapter gives a brief information about acceleration and detector part of the CLIC project as well as a description of the BDS. In Chapter 2, Linear Collider optics and physics are explained. The halo and muon generation processes are investigated particularly in Chapter 3-4. As a result, in Chapter 5, the muon rates and their reduction efficiency, which are concluded in BDSIM Monte Carlo simulations, are estimated and discussed for the CLIC project at CERN.

2. THEORY

In order to transport the accelerated beams, motion of particles under a magnetic field need to be studied in detail, since the beam optics should be designed and relevant parameters should be determined based on behavior of such particles. Therefore, a beam transport system, which consists of bending and focusing magnets, have been installed. This section begins with the information and formulation of the particle tracking in the beam transport system. Then it continues with the description of halo particle generation, which is one of the important beam loss mechanisms, while particles are transported.

2.1. Linear Beam Dynamics

The particles, which have been accelerated to higher energies, are controlled by electric and magnetic fields. While the electric field is responsible for acceleration of the particles, the beam is shaped and transported with help of the magnetic field. 6 dimensional phase-space elements explain the motion of the particles in these fields. The coordinates of each particle in the phase-space are defined as (x, p_x, y, p_y, s, E) . p_x and p_y are the momenta of the particle and x, y, s are the particle coordinates and E is the energy value of the particle. Generally, instead of giving E value, deviation from the ideal momentum Δp or relative momentum deviation $\Delta p/p$ can be defined [Wiedemann 2007].

Focusing magnetic forces, which affect the charged particles, provide their orbits close to a reference orbit. For relativistic particles ($v \sim c$), effects of the electric field can be ignored and only the magnetic field effect is considered.

The motion of charged particle is governed by Lorentz Force;

$$\vec{F} = q(\vec{E} + \vec{v} \times \vec{B}) \quad (2.1)$$

where q is charge of the particle, \vec{v} is velocity, \vec{E} and \vec{B} represent the electric and magnetic fields respectively. Considering uniform magnetic field B oriented parallel to the particle

motion, there is an equality between Lorentz force and centrifugal force. By neglecting the electric field, it is given as

$$B \cdot r = \frac{p}{q} = \frac{1}{ec} \cdot \beta \cdot E = \frac{10}{3} \cdot \beta \cdot E \quad (2.2)$$

where $B \cdot r$ [T.m] is defined as magnetic rigidity and E is the energy of the particle in GeV. Here, if we define $p = \gamma m v$ and $v = \beta c$, the coefficient of this equation becomes $1/(ec)$ which is roughly equal to $1/0.299$. On the other hand, the motion of particles in periodic systems like magnets on lattice, is determined by Hill's Equation,

$$u'' + K(s)u = 0 \quad (2.3)$$

where u represents the x or y coordinates and $K(s)$ defines the focusing/defocusing strength (depending on the sign) of the magnet at the trajectory s [Wiedemann 2007, Lee 2012].

Assuming that the $K(s)$ is equal to a constant like k_0 , the Equation 2.3 is solved as

$$u(s) = C(s)u(0) + S(s)u'(0) \quad u'(s) = C'(s)u(0) + S'(s)u'(0) \quad (2.4)$$

and for the condition $k_0 > 0$

$$C(s) = \cos(\sqrt{k_0}s) \quad S(s) = \frac{1}{\sqrt{k_0}} \sin(\sqrt{k_0}s) \quad (2.5)$$

and for $k_0 < 0$ [Wiedemann 2007].

$$C(s) = \cosh(\sqrt{|k_0|}s) \quad S(s) = \frac{1}{\sqrt{|k_0|}} \sinh(\sqrt{|k_0|}s) \quad (2.6)$$

2.2. Matrix Elements

The solution of Hill's equation for particles, which travel along the beam line, can be written in a matrix form as in Equation 2.7.

$$\begin{pmatrix} x(s) \\ x'(s) \end{pmatrix} = \begin{pmatrix} Cx(s) & Sx(s) \\ C'x(s) & S'x(s) \end{pmatrix} \begin{pmatrix} x(0) \\ x'(0) \end{pmatrix}, \quad \begin{pmatrix} y(s) \\ y'(s) \end{pmatrix} = \begin{pmatrix} Cy(s) & Sy(s) \\ C'y(s) & S'y(s) \end{pmatrix} \begin{pmatrix} y(0) \\ y'(0) \end{pmatrix} \quad (2.7)$$

The general form of the transfer matrix from point s_0 to s is written

$$\begin{pmatrix} u \\ u' \end{pmatrix}_s = M(s|s_0) \begin{pmatrix} u \\ u' \end{pmatrix}_{s_0} \quad (2.8)$$

where M refers to 2x2 matrix or transfer matrix form of the lattice element whose length (L) is equal to $s - s_0$ [Wiedemann 2007]. The unification of these matrix is written in a more convenient form in Equation 2.9.

$$\begin{pmatrix} x(s) \\ x'(s) \\ y(s) \\ y'(s) \end{pmatrix} = \begin{pmatrix} Cx(s) & Sx(s) & 0 & 0 \\ C'x(s) & S'x(s) & 0 & 0 \\ 0 & 0 & Cy(s) & Sy(s) \\ 0 & 0 & C'y(s) & S'y(s) \end{pmatrix} \begin{pmatrix} x(0) \\ x'(0) \\ y(0) \\ y'(0) \end{pmatrix} \quad (2.9)$$

For example, the transformation matrix for a drift element, which has $L(s - s_0)$ length and no magnetic field, is given as;

$$\begin{pmatrix} u(s) \\ u'(s) \end{pmatrix} = \begin{pmatrix} 1 & L \\ 0 & 1 \end{pmatrix} \begin{pmatrix} u(0) \\ u'(0) \end{pmatrix} \quad (2.10)$$

and the matrix form of this element is given as;

$$M_{drift}(s|s_0) = \begin{pmatrix} 1 & L \\ 0 & 1 \end{pmatrix} \quad (2.11)$$

The other element is quadrupole magnet. This element is focusing the beam in one axis while defocusing in other axis. The total focusing of the beam can be determined by the combination of sequenced quadrupoles. For a focusing magnet whose length is L and magnetic field is

$$B_x = -g(s)y \quad B_y = -g(s)x \quad (2.12)$$

and magnetic gradient is (m^{-2})

$$k(s) = \frac{g(s)}{B_0\rho} \quad (2.13)$$

The transport matrix of the given quadrupole becomes;

$$\begin{pmatrix} u(s) \\ u'(s) \end{pmatrix} = \begin{pmatrix} \cos(\sqrt{k}L) & \frac{1}{\sqrt{k}}\sin(\sqrt{k}L) \\ \sqrt{k}\sin(\sqrt{k}L) & \cos(\sqrt{k}L) \end{pmatrix} \begin{pmatrix} u(0) \\ u'(0) \end{pmatrix} \quad (2.14)$$

If the magnetic field strength value k is greater than zero ($k > 0$), the quadrupole is focusing the beam and its matrix form is given;

$$M_{QF}(s|s_0) = \begin{pmatrix} \cos(\sqrt{k}L) & \frac{1}{\sqrt{k}}\sin(\sqrt{k}L) \\ \sqrt{k}\sin(\sqrt{k}L) & \cos(\sqrt{k}L) \end{pmatrix} \quad (2.15)$$

The other condition is the $k < 0$, therefore, transport matrix is given for quadrupole;

$$\begin{pmatrix} u(s) \\ u'(s) \end{pmatrix} = \begin{pmatrix} \cosh(\sqrt{k}L) & \frac{1}{\sqrt{k}}\sinh(\sqrt{k}L) \\ \sqrt{k}\sinh(\sqrt{k}L) & \cosh(\sqrt{k}L) \end{pmatrix} \begin{pmatrix} u(0) \\ u'(0) \end{pmatrix} \quad (2.16)$$

and its matrix form is given for defocusing quadrupole

$$M_{QD}(s|s_0) = \begin{pmatrix} \cosh(\sqrt{k}L) & \frac{1}{\sqrt{k}}\sinh(\sqrt{k}L) \\ \sqrt{k}\sinh(\sqrt{k}L) & \cosh(\sqrt{k}L) \end{pmatrix} \quad (2.17)$$

If $\sqrt{k}L$ is $\sqrt{k}L \rightarrow 0$, $M_{QF} = M_{QD}$ and for this situation matrix form becomes

$$M_{(QF,QD)} = \begin{pmatrix} 1 & 0 \\ -kL & 1 \end{pmatrix} \quad (2.18)$$

If the beam passes from several elements, the total transfer matrix is calculated by the multiplication of each matrix [Wiedemann 2007]. For example, a beam line, which is composed by 5 elements, the transfer matrix M is given as

$$M = M_5 \cdot M_4 \cdot M_3 \cdot M_2 \cdot M_1 \quad (2.19)$$

The coordinate of the particle, which is located at the starting point and move along the beam line, is determined by the equation

$$\begin{pmatrix} u(s) \\ u'(s) \end{pmatrix} = M(s|s_0) \begin{pmatrix} u(s_0) \\ u'(s_0) \end{pmatrix} \quad (2.20)$$

where s_0 represents the starting point, s is the final position. In Chapter 1, Figure 1.6, the parts of the BDS have been explained. The first section, which corresponds to the diagnostic section, contains a sequence of quadrupoles. In this section, the particle trajectories traveling along these quadrupoles on horizontal and vertical planes have been sketched in Figure 2.1. The particle coordinate and their trajectories have been simulated with BDSIM 6D tracking routines.

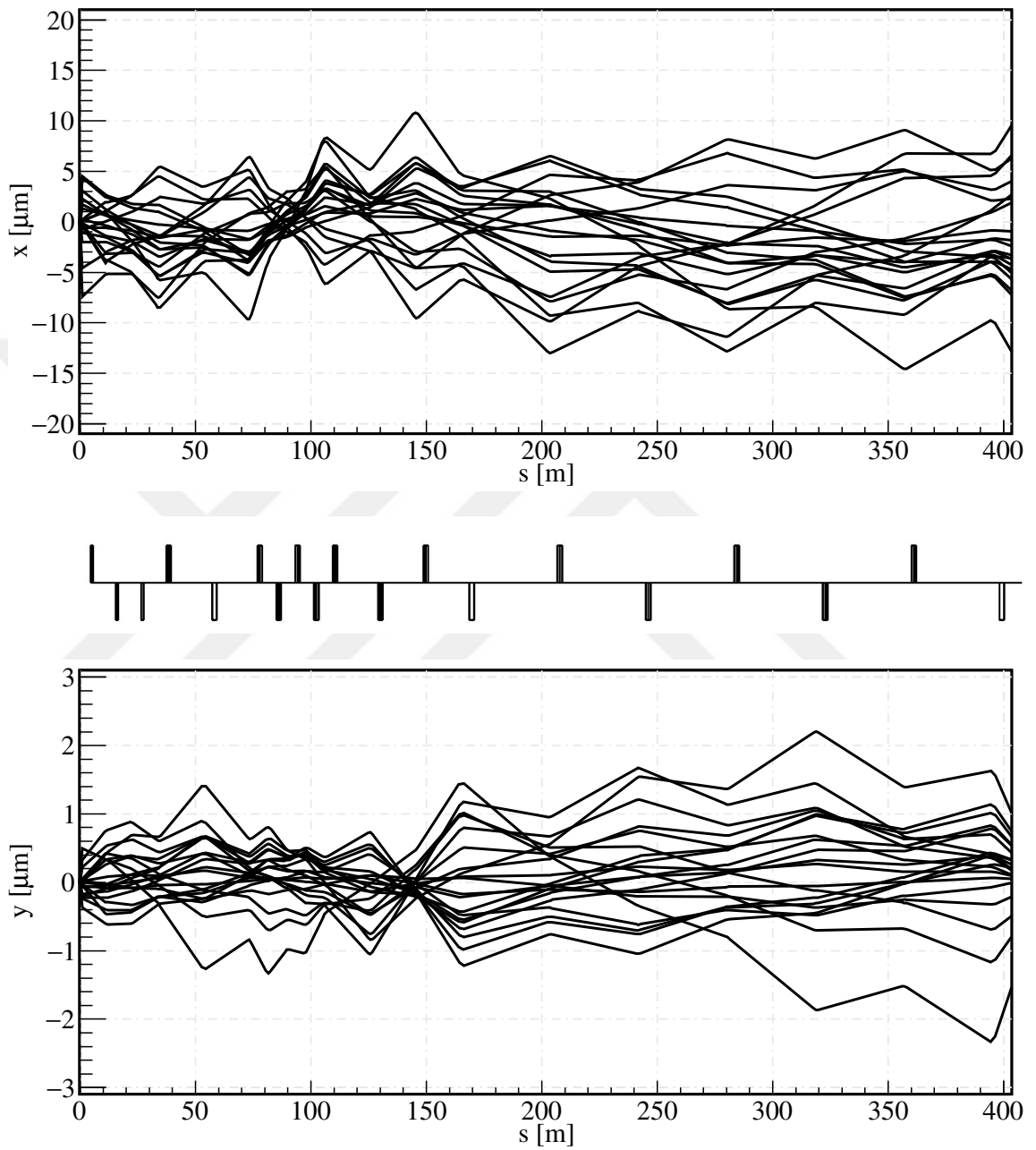


Figure 2.1. Overlapping trajectories of several particle while traversing in quadrupoles on the diagnostic section

2.3. Particle Beams and Phase Space

The tracking of a single charged particle in any magnetic field have been explained in the previous section. However, it is necessary that a bunch of particles should be followed/tracked in the simulations instead of tracking individual particles. In order to determine of the collective motion of particles, their dynamics have been observed in phase space [Wiedemann 2007, Schopper and Myers 2013].

Floquet theorem states that

$$u(s) = A\omega_s \cos(\psi_s + \psi_0) \quad (2.21)$$

where ω_s and ψ_s are periodic with the same period. The derivatives of it is given

$$u'(s) = A \cos(\psi_s + \psi_0) \omega_s' - A \omega_s \psi_s' \sin(\psi_s + \psi_0) \quad (2.22)$$

and

$$u''(s) = -A(\cos(\psi_s + \psi_0)(\omega_s \psi_s'^2 - \omega_s'') + \sin(\psi_s + \psi_0)(\omega_s \psi_s'' + 2\psi_s' \omega_s')) \quad (2.23)$$

Substituting Equation 2.3, the coefficients of sine and cosine should be equal to zero. Then it is concluded as below

$$\psi' = \frac{1}{\omega^2} \quad (2.24)$$

$$\omega'' + K\omega = \frac{1}{\omega^3} \quad (2.25)$$

Equation 2.25 represents the beam envelope equation for the betatron motion. Betatron functions are given as

$$\beta(s) \equiv \omega^2(s) \quad (2.26)$$

$$\alpha(s) \equiv \frac{-1}{2} \frac{d\beta(s)}{ds} \quad (2.27)$$

$$\gamma(s) \equiv \frac{1 + \alpha^2(s)}{\beta(s)} \quad (2.28)$$

These betatron functions ($\beta_{x,y}$, $\alpha_{x,y}$, $\gamma_{x,y}$) are also known as Courant-Snyder parameters and all of them define the linear motion of particles in phase space [Courant and Snyder 1958]. In beam dynamics, a beam traveling along s trajectory in phase space (u, u'), has an elliptic area.

$$\varepsilon = \gamma u^2 + 2\alpha u u' + \beta u'^2 \quad (2.29)$$

The Equation 2.29 represents Courant-Snyder invariant and ε is called beam emittance. The area of beam is equal to $\pi\varepsilon$. The area of the ellipse is a measure of how much the particle deviate from the ideal trajectory.

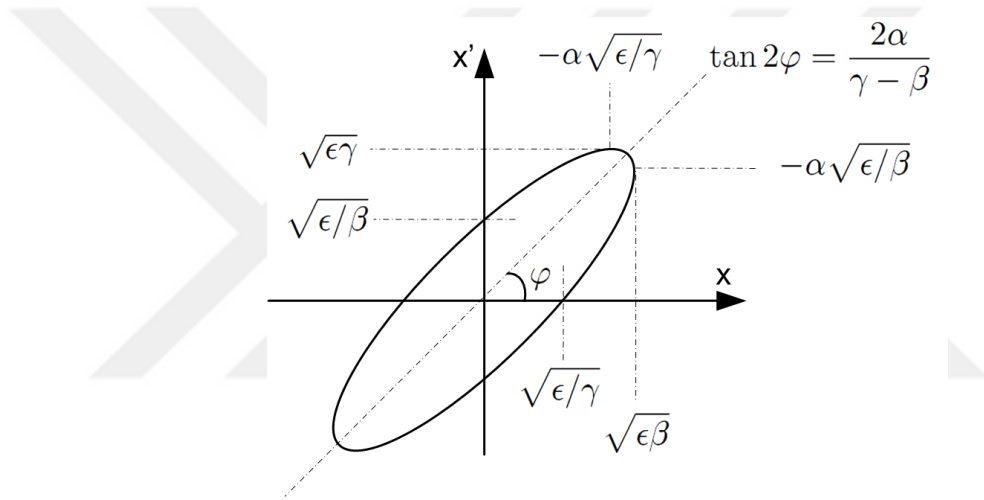


Figure 2.2. Courant Snyder ellipse parameters in phase space [Wiedemann 2007]

The beam-ellipse parameters and their relations are represented in Figure 2.2. Since the beam energy alters in the beam transport system, using normalized beam emittance values is more convenient than using their true values. The normalized beam emittance are given as

$$\varepsilon_N = \gamma\varepsilon \quad (2.30)$$

where $\gamma = E/m_e c^2$ represents the relativity factor. Normalized emittance value is constant even if the particle energy changes due to the acceleration process [Lee 2012].

Horizontal and vertical betatron functions for diagnostic section on BDS are represented in Figure 2.3. The betatron function in the lattice is mostly symmetric in the two planes,

and generally reaches its maximum and minimum values at the center of the quadrupoles.

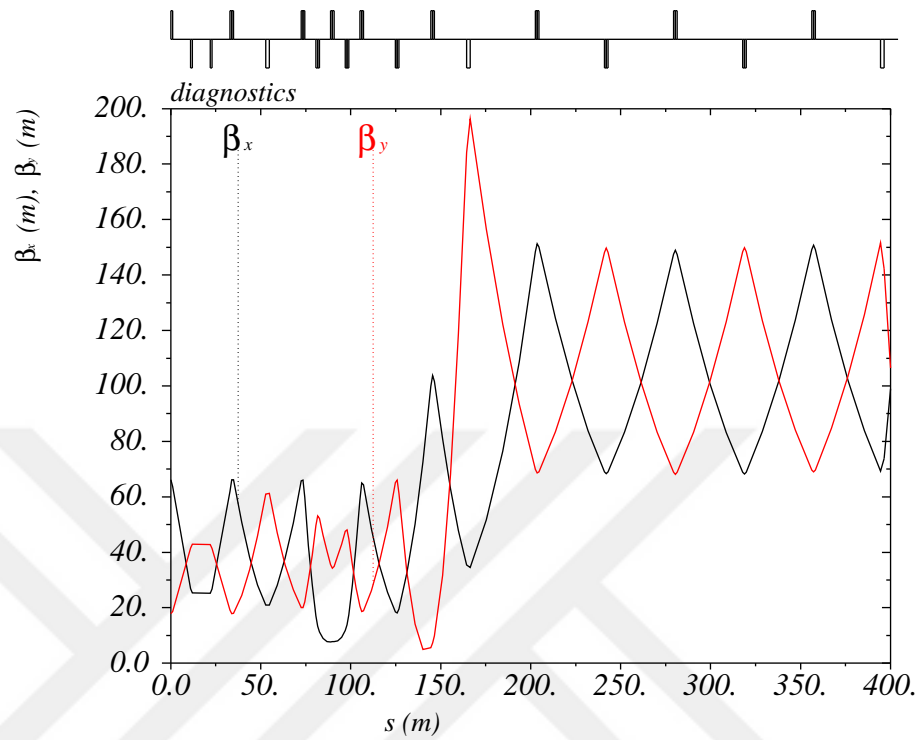


Figure 2.3. Betatron functions for diagnostic section on BDS

The other parameter about the particle motion in phase space is dispersion. Dispersion function is related to the particle which deviates from its original reference orbit and momentum, under magnetic field of the lattice element. A beam consists of particles with momenta of spreaded particles around a reference momentum p_0 . The particles, which have greater momentum, have a greater bending radius. The dispersion function is determined by the following equation [Lee 2012, Wiedemann 2007].

$$D(s) = \frac{p \cdot dx(s)}{dp} \quad (2.31)$$

In Figure 2.4, betatron and dispersion functions, which are called twiss parameters, have been calculated for BDS by using MAD-X (Methodical Accelerator Design) tool [CERN 2002]. Betatron functions are periodic in diagnostic section of the BDS. In the energy collimation section, where off-momentum particles have been removed, the betatron function increases from several hundred meters to km order. The third part is the betatron collimation section where the betatron functions have a periodical change along this section. The last part, which is the final focus section, has greater betatron function in both planes but the last quadrupoles, which have very strong magnetic fields, focus the beam to the desired parameters at the end of the BDS.

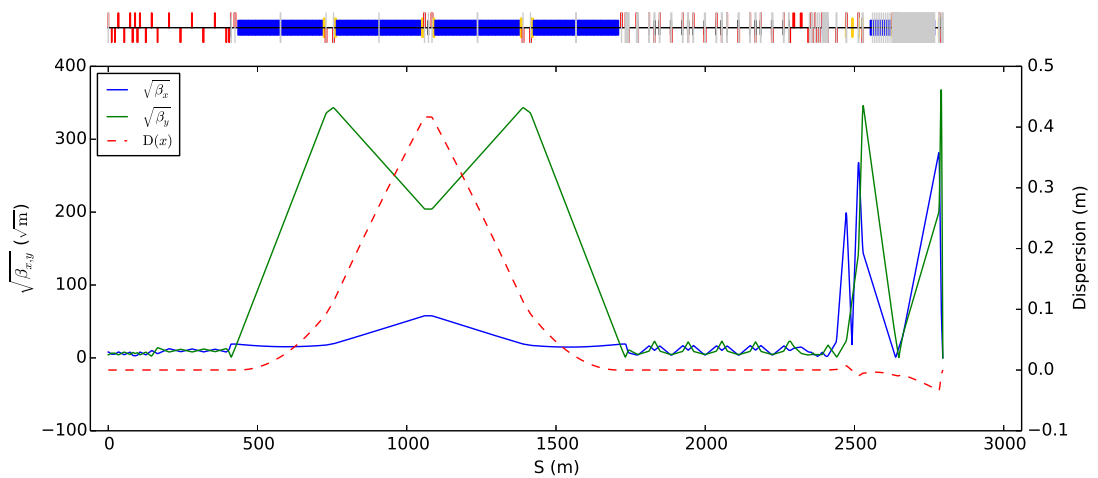


Figure 2.4. Betatron and dispersion functions through the BDS

2.4. Halo Particles and Generation Mechanisms

It is surely beyond doubt that the performance of accelerator depends on the elements of the system. The most important parts/elements of the system are the vacuum system elements. Accelerator systems need to work under perfect vacuum conditions but in the real world, there is no perfect vacuum system, yet. The residual gas in the vacuum system causes a degradation in the beam by generating halo particles around it. These halo particles negatively affect the beam quality by increasing the emittance of the beam.

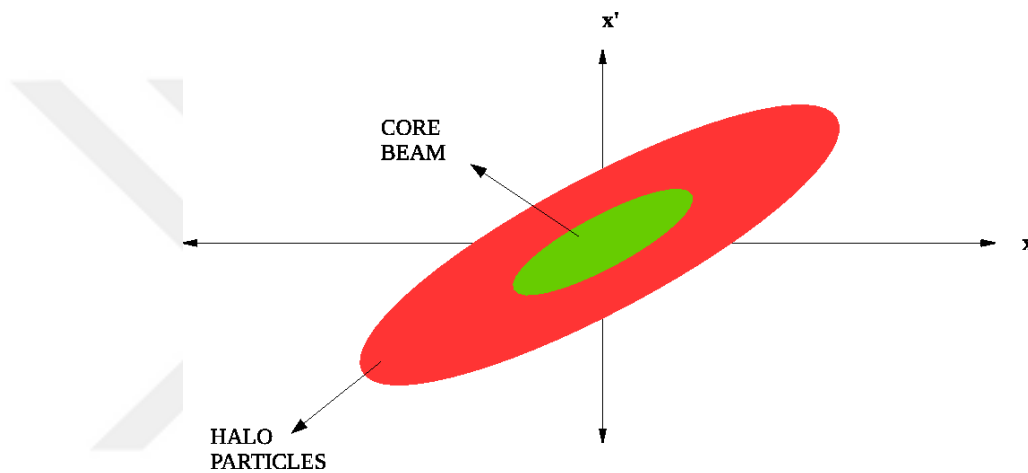


Figure 2.5. Schematical representation of halo and core beam

Especially for high-intensity beam accelerators, halo particles have a crucial importance. The halo particles can cause beam losses which is a critical subject for the high-intensity beams.

Indeed, halo particles are also beam particles but they have greater amplitude and/or less energy and intensity than core beam particles. The core beam or main beam and the halo particles around it are represented schematically in Figure 2.5. The beam and halo particles distributions vary continuously under strong space-charge forces along the acceleration path [Nghiem et al 2012]. Therefore, it is hard to predict the distribution of halo particles, since they do not follow any proper distribution.

Halo particles are generated mostly due to residual gas in the acceleration system and eventually they cause beam losses. For this reason, halo particles are unwanted beam

mechanism. There are many reasons for halo particle generation, hence we investigate them by dividing into three subtitles. The well-known and dominant process is beam-gas (residual gas) scattering. This scattering will be considered under the particle related processes class. Additionally, halo particles can be generated due to optic elements on the acceleration line. This process is classified as optic related process. There are also other processes or effects which contribute to the halo particle generation as vibrations, noise, drak current etc.

2.4.1. Particle Related Processes

The beam-gas (residual gas) interactions affect the beam lifetime and increase emittance of the beam. These effects are important factors to degrade the beam quality.

There are two types of interactions between beam and residual gas. The first one is beam-gas elastic scattering which means that the beam particles do not lose their energy, but change their usual path. The second one is the beam-gas inelastic scattering which means that the beam particles lose their energy significantly.

Beam-Gas Elastic Scattering: The beam particles are affected from the Coulomb field of the residual gas atoms/molecules and are deflected from their original path. This process is a special process which is called Mott scattering. Basically, the Mott scattering is similar to the Rutherford scattering. However, Rutherford scattering assumes that the scattered particles are not relativistic (non-relativistic $E \ll m$). On the other hand, in the Mott scattering, electrons are assumed to be relativistic $E \gg m$ and their helicity is conserved. Differential cross section for Rutherford scattering is given as

$$\frac{d\sigma}{d\Omega} = \left(\frac{Zr_e^2}{2\gamma\beta^2} \right)^2 \left(\frac{1}{\sin^4\left(\frac{\theta}{2}\right)} \right) \quad (2.32)$$

where Z is atomic number, r_e is electron radius and γ is Lorentz factor and θ is the angle between scattered electron and atom.

Considering the helicity conservation, differential cross section has been given as [Burkhardt

et al 2007]

$$\frac{d\sigma}{d\Omega} = \left(\frac{Zr_e^2}{2\gamma\beta^2}\right)^2 \left(\frac{1 - \beta^2 \sin^2(\frac{\theta}{2})}{\sin^4(\frac{\theta}{2})}\right) \quad (2.33)$$

where $\beta = 1$ and $\sin(\theta/2) \approx \theta/2$. $1 - \beta^2 \sin^2(\theta/2)$ and $\cos^2(\theta/2)$ represent the electron spin. In order to calculate the total cross section, it can be integrated over the solid angle. In Equation 2.33, θ represents the scattering angle and it is predicted that it exceeds the beam divergence. In this situation, the minimum scattering angle is given as [Burkhardt et al 2007]

$$\theta_{min} = \sqrt{\frac{\epsilon_N}{\gamma\beta_y}} \quad (2.34)$$

where ϵ_N is normalized emittance ($\epsilon_N = \gamma\epsilon$) and β_y represents the vertical betatron function.

$$\sigma_{mott} = 4\pi \cdot \frac{Z^2 r_e^2}{\gamma^2 \theta_{min}^2} \quad (2.35)$$

Total cross section of Mott scattering is given as

$$dn_p = \frac{\epsilon^2 d\epsilon}{\pi^2 c^3 \hbar^3 (e^{\epsilon/k_B T} - 1)} \quad (2.36)$$

The calculated total cross section values have been evaluated in Table 2.1. For these calculations, betatron function β_y and normalized emittance ϵ_{yN} are given as 100m, 2×10^{-8} m.rad, respectively.

Intra beam scattering and thermal photon scattering are other beam-gas elastic scattering related processes. Intra beam scattering is the beam-gas elastic scattering process which occurs due to multiple scattering of the beam particles with each other. This generates halo particles around the beam by increasing the amplitude of the particles. This process generally dominates for low energetic beams [Brugger et al 2013]. The other process is thermal photon scattering which basically can be defined as the inverse Compton Scattering. There is an inelastic scattering between electron and photon in this process. During the process, which is between electron and photon, the photon gains energy [Fitterer et al

2009, Di Domenico 1991]. Thermal photons are, in general, generated by the black body radiation in the acceleration system. Their intensity and energy distribution have been determined by Planck's formula [Telnov 1987],

$$dn_p = \frac{\varepsilon^2 d\varepsilon}{\pi^2 c^3 \hbar^3 (e^{\varepsilon/k_B T} - 1)} \quad (2.37)$$

where ε is photon energy, c is speed of light, k_B is Boltzmann constant and T represents temperature, in Kelvin (K). By integrating the Plank formula, photon number per unit volume can be given as [Fitterer et al 2009, Di Domenico 1991]

$$n_p = \frac{2.4(k_B T)^3}{\pi^2 c^3 \hbar^3} \quad (2.38)$$

where T is defined as absolute temperature. Therefore, at 300 K temperature, the number of photons n_p is found to be order of $20.2 T^3 \text{cm}^{-3}$ [Di Domenico 1991]. For thermal photon scattering, Compton scattering cross section is given as [Fitterer et al 2009, Di Domenico 1991]

$$\sigma_{compton} = 2\pi r_e^2 \frac{1}{x} \left(\left(1 - \frac{4}{x} - \frac{8}{x^2}\right) \ln(1+x) + \frac{1}{2} + \frac{8}{x} - \frac{1}{2(1+x)^2} \right) \quad (2.39)$$

where x is unitless parameter and

$$x = \frac{4E\varepsilon}{m^2 c^4} \cos^2 \frac{\alpha}{2} \quad (2.40)$$

where E is initial energy of electron, ε is initial energy of photon and α is collision angle. x value increases with increasing of E . If $x \gg 1$, which means that the process is relativistic, the cross section is given as

$$\sigma_{compton} = 2\pi r_e^2 \frac{1}{x} \left(\ln x + \frac{1}{2} \right) \quad (2.41)$$

For the relativistic energy case, total cross section decreases but energy loss of electrons

increases due to electron scattering. The energy fluctuation is given as

$$\frac{\Delta E}{E} = \frac{\varepsilon_{max}}{E} = \frac{x}{x+1} \quad (2.42)$$

Even if cross section value is lower, the energy loss of electron becomes rather greater.

2.4.2. Beam - Gas Inelastic Scattering

The core beam particles interact with the residual gas atoms and become halo particles by losing their energy. The energy loss is usually due to Bremsstrahlung process. The differential cross section of Bremsstrahlung process is given as

$$\frac{d\sigma}{dk} = 4\alpha r_e^2 \frac{1}{k} \left(\left(\frac{4}{3} - \frac{4}{3}k + k^2 \right) (Z^2(L_{rad} - f) + ZL'_{rad}) + \frac{1}{9}(1-k)(Z^2 + Z) \right) \quad (2.43)$$

where r_e is radius of electron, α is fine-structure constant and equal to $1/137$, f is Coulomb correction function, k represents the ratio of incoming particle energy to generated particle energy. The total cross section is given as [Burkhardt et al 2007, Brugger et al 2013, Tsai 1974]

$$\sigma_{bremss} = 4\alpha r_e^2 Z(Z+1) \log(287/\sqrt{Z}) \left(-\frac{4}{3} \ln(k) - \frac{5}{6} + \frac{4}{3}k - \frac{k^2}{2} \right) \quad (2.44)$$

The cross section of this process essentially depends on type and amount of the residual gas. Evaluated total cross section values for a given type of gas are calculated in Table 2.1 where k is equal to 0.01. Comparison of processes indicates that the cross section of Mott scattering is more dominant than bremsstrahlung .

Table 2.1. Total cross section values evaluated for Bremsstrahlung and Mott Scattering processes

Gas	σ_{bremss} [barn]	σ_{mott} [barn]
He	0.39	5.82×10^4
Ar	17.62	4.72×10^6

2.4.3. Processes Related to Optics

These processes are basically related to optic elements on beam line and their brief definitions are given as follows,

- **Mismatch** : The shape of transferring beam on the machine does not coincide the ellipse in the phase-space, this is called mismatched beam. If the acceptance covers the incoming beam, it is called matched beam. The matched and mismatched conditions have been represented in Figure 2.6. The mismatched beam causes to the dilution of beam particles in phase space.

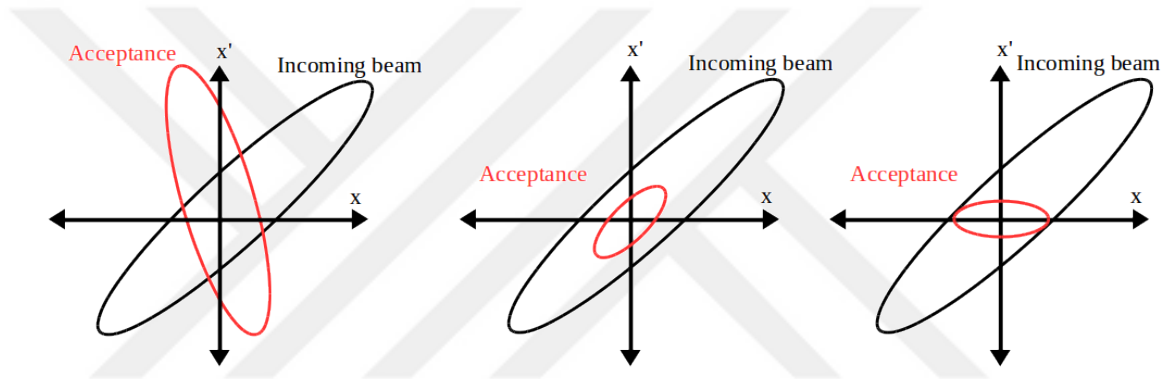


Figure 2.6. Match conditions in phase space from left to right; mismatch, perfect match and efficient match

- **Coupling** : This effect is described as motion in one plane with depending on the other plane. This is like a pair of coupled pendulum. For example, a particle passing through a skew quadrupole, which has a horizontal offset, is subjected to vertical kicks. This causes a coupling for both vertical and horizontal motion.
- **Nonlinearities** : This is mostly due to errors in magnetic fields. The elements on the beam line may have nonlinearities on their magnetic fields and this causes a change in particle motion equation which depends on the magnetic field. The nonlinearities in the particle motion might raise the generation of halo particles.
- **Misalignment** : Even an error at micron level on the alignment of the beam line element affects other elements, hence the particle motion on them. The deflection

of particles due to the misalignments induces the beam loss and increases the halo generation potential.

These briefly explained processes or effects are mainly known to have a potential subject to cause the halo generation.

2.4.4. Other Processes

Vibrations, noises, dark currents and others, like occurring due to external factors, might have a remarkable contribution to generation of halo particles [Fitterer et al 2009]. All types of vibrations may cause to initiate the oscillation of beam particles and increase the emittance. Noise generally comes from the electronic components of the system. This leads to oscillations of the beam and increase in emittance in phase space. Dark current is another unwanted effect which occurs due to emission of electron from wall structure of a cavity. These electrons can be accelerated with the other beam particles and it leads to a dark current. Vibration, noise and dark current are the external factors to affect halo generation. Additionally, they do not depend on the beam energy. In this study, only the beam-gas interactions have been considered because of their dominant distribution to halo particle generation.

3. ANALYSIS

In the first part of this section, the amount of halo particle generation have been investigated by using the HTGEN (Halo and Tail Generation) code [Ijaz Ahmed 2008]. Then, the muon production processes, which are the particular interest of this thesis, and the simulation of them with GEANT4 [Agostinelli et al 2003] Monte Carlo code are presented and discussed.

3.1. Simulations of Halo Particles

The halo particle production by Bremsstrahlung and Mott scattering, which have been described in previous section, have been determined with HTGEN code. HTGEN determines the halo population. HTGEN interface to PLACET (Program for Linear Accelerator Correction Efficiency Tests) have been used to estimate the amount of halo particles along the beam line in detail [Schulte 2000]. For the simulations, the beam energy value has been set to 1.5 TeV. The amount of halo particles around the core beam have been determined for each element. Figure 3.1 shows the estimated amount of halo particles and core beam along the BDS, horizontally (upper) and vertically (bottom). The green markers represent the core beam particles and red markers represent the halo particles around the core beam. At the horizontal plane halo particles start to be widened at the energy collimation section, which is located at about 1000 m, and at the final focus section located at about 2600 m. At the vertical plane halo particles tend to be broadened again at the energy collimation section and final focus section. For both planes, one should always bear in mind that the factor of broadening is at micron scale. The distribution of the halo particles alters with the shape of the core beam along the BDS.

The first vertical spoiler (YSP1) locates at about 1830 m to filter produced halo particles. The distribution of the halo particles at YSP1 can be seen in Figure 3.2 for both horizontal and vertical planes. The core beam has a narrow distribution. However, the halo particles do not fit a uniform distribution shape even if it seems to be Gaussian-like distribution.

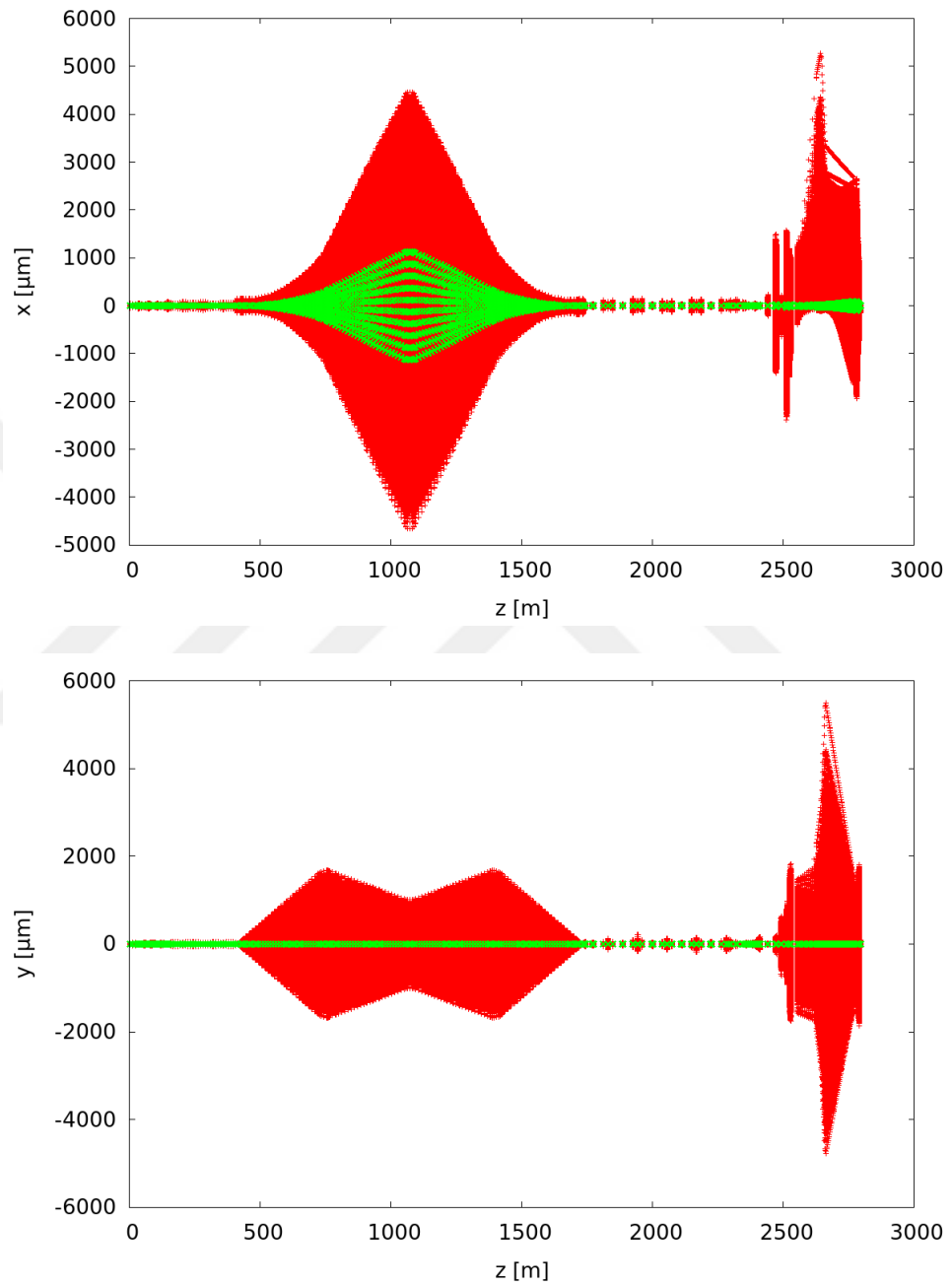


Figure 3.1. The estimated halo particles (red) and core beam (green) along the BDS

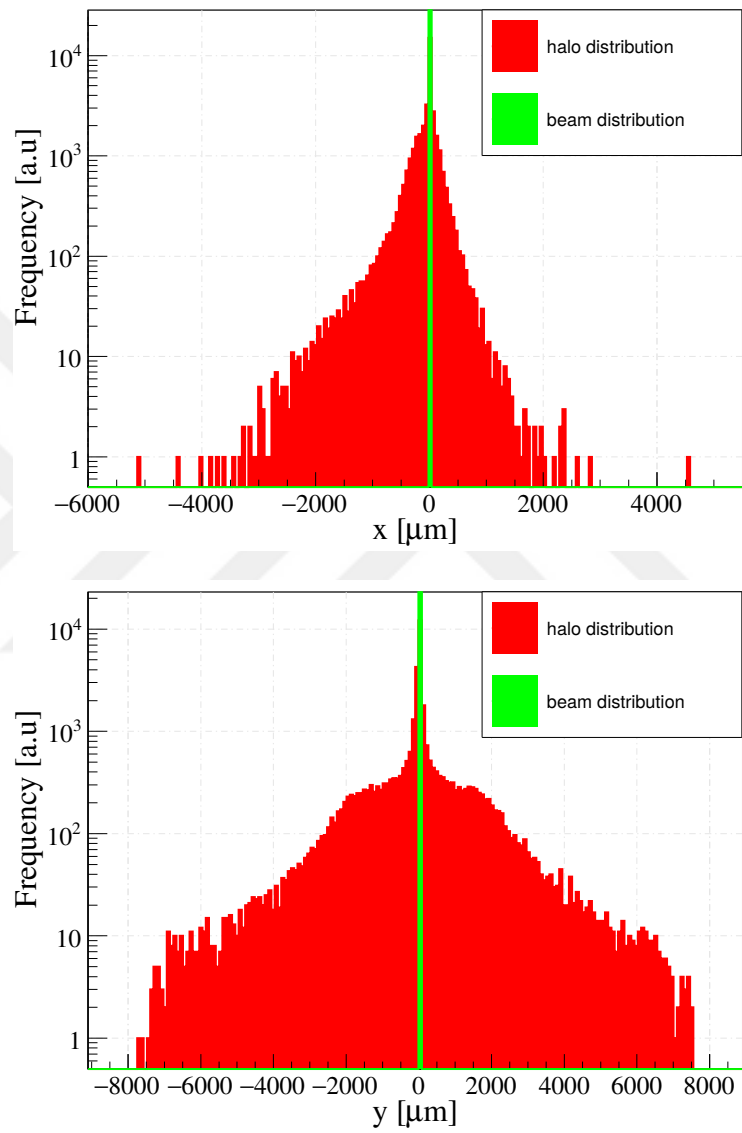


Figure 3.2. The distribution of halo particles at YSP1

3.2. Muon Production Mechanisms at High Energies

In the previous section the halo particle generation mechanism around the core beam have been investigated. Halo particles are of crucial importance for beam loss mechanism. They also effect the performance of the accelerator system. Therefore, the unwanted halo particles around the core beam have been removed by locating collimators along the beam line. When the energetic halo particles interact with the collimator material, they generate energetic photons and/or muon pairs as an unwanted background source. In this section, the muon production mechanisms and cross sections have been investigated. Their simulations by using electromagnetic package in GEANT4 have been performed.

High energy electrons, positrons and photons emit bremsstrahlung radiation which means that they emit energetic photons (γ) by interacting with matter. Then, the photon generates electron/positron pairs ($\gamma \rightarrow e^+ e^-$) by interacting with the nuclei. These pairs make another gamma emission and again cause to generate electron/positron pairs. This creates an electromagnetic shower. The schematic representation of pair production and Bremsstrahlung mechanism can be seen in Figure 3.3. Pair production does not mean only electron/positron pair production. It also contains the lepton pairs like μ , τ .

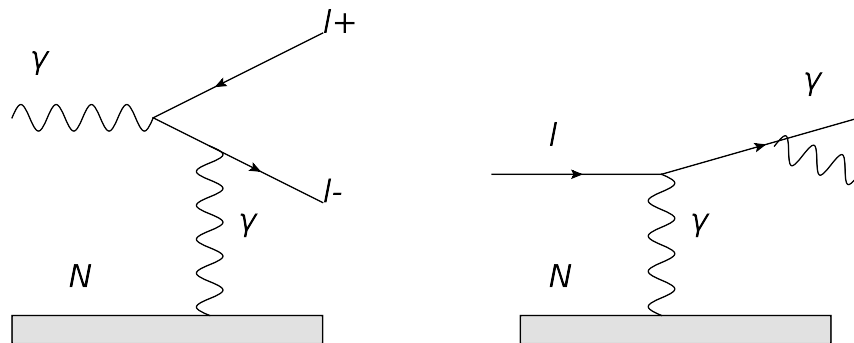


Figure 3.3. Schematics of pair production and Bremsstrahlung mechanisms

Energetic photons generate muon pair when they are affected by the Coulomb field of atomic nuclei. This process is defined as Bethe-Heitler muon pair production ($\gamma + N \rightarrow \mu^+ + \mu^- + N$) [Baur and Leuschner 1999, Burkhardt et al 2002a, Burkhardt et al 2002b]. $e^- + e^+ \rightarrow \mu^+ + \mu^-$ process occurs with annihilation of electron-positron into a virtual

photon and then creation of a muon pair with the enhanced s-channel production. These two mechanisms are direct muon production processes. Additionally, there is another process, which contributes to the muon production indirectly. Electrons annihilate with positrons and create also hadron pairs as well as lepton pairs. This process can be given as $e^+ + e^- \rightarrow \text{hadrons}$.

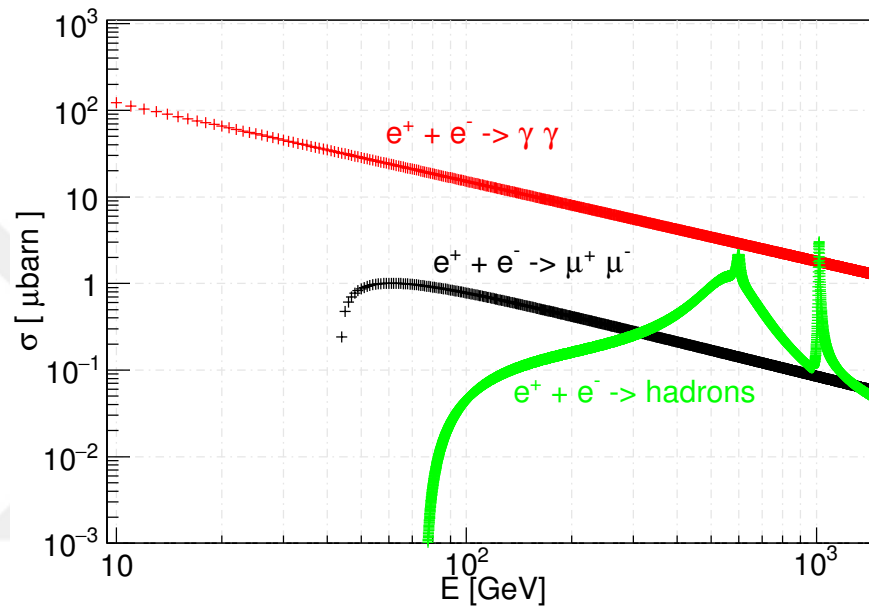


Figure 3.4. Cross sections of the muon production processes with respect to incident beam energy up to 1500 GeV

The cross section values with respect to the incoming beam energy have been given in Figure 3.4 for these muon pair production processes. The positron-electron annihilation into gamma process has been represented with the red markers in Figure 3.4. It is clear that the cross section value decreases by an increase of the incident beam energy. The black markers represent the positron-electron annihilation into muon process. For this process, the threshold energy is 43.69 GeV [Physics Reference Manual 2013]. The cross section values fall as the incident beam energy increases for positron-electron annihilation into gamma process. The green markers show the positron-electron annihilation into hadrons. For this process, there are no uniform changes for cross section values depending on the incident beam energy. There are three peaks; two of them are between 500 GeV and

600 GeV, the third one is at around 1000 GeV incident positron beam energy. These three peaks match with the resonance scales of $\rho(770)$, $\omega(782)$ and $\phi(1020)$ vector mesons, respectively.

3.2.1. Bethe - Heitler Muon Pair Production Process

Energetic photons create real photons through Bremsstrahlung process. The real photon can create lepton pairs as it is affected by the presence of electric field of the high-Z target nuclei ($\gamma + e \rightarrow e + \mu^+ \mu^-$) [Burkhardt et al 2002b]. This is called Bethe-Heitler process. In this process, the incoming photon shares its energy to produce muon pair. Schematic representation of this process is given in Figure 3.5. The differential cross section is given as

$$\frac{d^2\sigma}{d\Omega dx_+} = 4Z^2 \alpha r_c^2 \left(1 - \frac{4}{3}x_+x_-\right) \log(W), \quad x_+ + x_- = 1 \quad (3.1)$$

where Z is charge of the nucleus, α is the fine structure constant, r_c is radius of the produced particle and $x_+ = E_{\mu^+}/E_{\gamma}$ is the ratio of energy of the positively charged outgoing muon to the incoming photon, $x_- = E_{\mu^-}/E_{\gamma}$ is the energy fraction for negatively charged muon. In the formula, W term is the related to the screening effect of the field of the nucleus [Burkhardt et al 2002b, Kelner et al 1995].

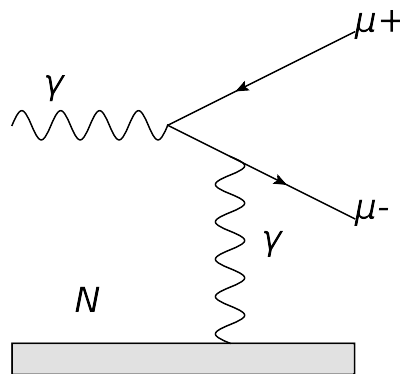


Figure 3.5. Schematic representation of muon production process with electromagnetic interaction

In Equation 3.1, the r_c term depends on the mass of the produced particle. So the probability of the production of the μ with respect to electron is given as $\left(\frac{m_e}{m_\mu}\right)^2 \approx 2.35 \times 10^{-5}$. In

this case, the muon production process is a very rare process in compared to the electron production. This process is defined as **GammaToMuPair** in GEANT4 [Agostinelli et al 2003] electromagnetic processes. Details about the implementation and parametrization can be found in ref [Burkhardt et al 2002b, Physics Reference Manual 2013].

The process is simulated with GEANT4 by interaction of photons with material. In Figure 3.6, the energy distribution of the muons is shown for 1000 GeV photons impinging on $1 X_0$ Carbon ($X_0 = 18.8$ cm) and Titanium ($X_0 = 3.6$ cm). Carbon has a low atomic number ($Z = 6$) so it can be an option for collimator material in beam pipe [Bogdanov et al 2006]. Another option is Titanium, which is proposed to use as collimator material coated with Copper in the BDS betatron collimation section, due to its high strong resistance against to heat and radiation damage [Aicheler et al 2012].

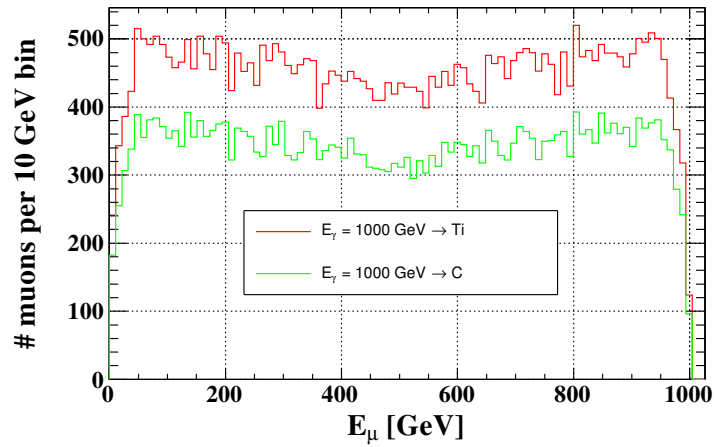


Figure 3.6. Energy distribution of muons which are produced with GammaToMuPair process

The produced muon energy distribution changes asymptotically as given in Figure 3.6. For the higher atomic number materials, the muon production rate increases with the square of atomic charge as given in Equation 3.1. Figure 3.7 shows the angular distribution of produced muon pairs in logarithmic scale, which is determined by GEANT4, in correlation with different incoming photon energy.

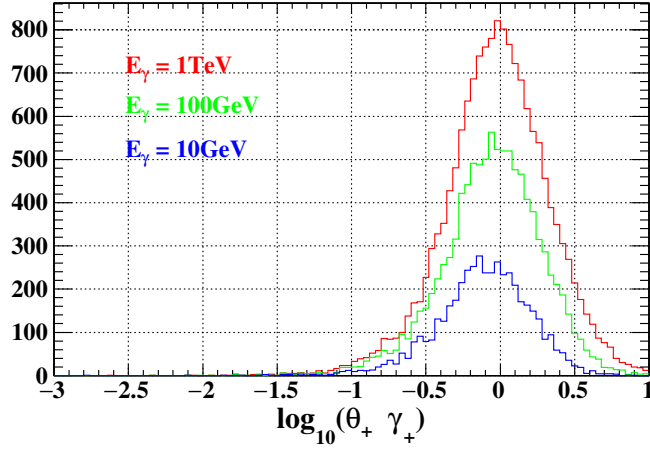


Figure 3.7. Angular distribution of muons for different photon energies

3.2.2. Electron-Positron Annihilation into Muon Pairs

Energetic positrons impinging on material annihilate with dressed electron in the material and create muon pairs, which is another electromagnetic process for the muon production. The lowest order diagram of the process ($e^+e^- \rightarrow \mu^+\mu^-$) is shown in Figure 3.8, where the photon exchange occurs in the s channel.

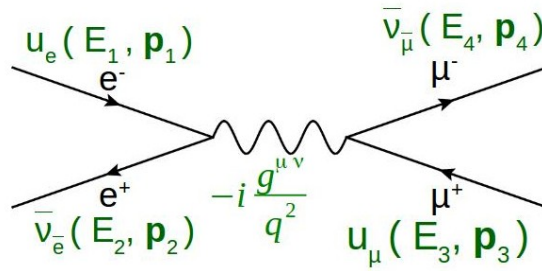


Figure 3.8. Diagram of annihilation into muon process

The differential cross section for this process can be defined as [Griffiths 1987, Bettini 2014]

$$\frac{d\sigma}{d\Omega} = \frac{1}{s \cdot 64\pi^2} \cdot \frac{|\vec{p}_f|}{|\vec{p}_i|} \cdot \overline{|M_{fi}|^2} \quad (3.2)$$

where s is the square of center of mass energy, the first two terms are phase space and delta functions, the last term is the squared matrix element. The matrix element can be written

from the diagram as

$$-iM = (p_2 \bar{v}_e i e \gamma^\mu u_e p_1) \cdot -i \frac{g^{\mu\nu}}{q^2} \cdot (u_\mu p_3 i e \gamma^\nu \bar{v}_\mu p_4) \quad (3.3)$$

and we can write the matrix element in terms of the electron and muon currents as in Equation 3.4.

$$M = \frac{-e^2}{s} g^{\mu\nu} j_e^\mu \cdot j_\mu^\nu \quad (3.4)$$

In general, the electron and positron are not polarized and for annihilation processes at higher energies fermions and anti-fermions have opposite helicities. Therefore, there are 4 helicity combinations in total for both initial state and final state.

$$\begin{aligned} M(\uparrow\downarrow\uparrow\downarrow) &= M(\downarrow\uparrow\downarrow\uparrow) = e^2(1 + \cos\theta) \\ M(\uparrow\downarrow\downarrow\uparrow) &= M(\downarrow\uparrow\uparrow\downarrow) = e^2(1 - \cos\theta) \end{aligned} \quad (3.5)$$

Helicity is a phenomenon which is equal to spin projection through the particle direction of motion division into the magnitude of the spin ($h = \frac{\vec{s} \cdot \vec{p}}{|\vec{s} \cdot \vec{p}|}$).

For instance, a spin -1/2 particle has a positive (+1) or negative (-1) helicity depending on the particle direction of motion as illustrated in Figure 3.9. When the spin direction and the particle motion direction is the same, it is called right-handed otherwise it is called left-handed. There are four possible spin combinations for initial state like $e_R^- e_L^+$, $e_R^- e_R^+$, $e_L^- e_L^+$, $e_L^- e_R^+$. Therefore, totally 16 combinations are possible for helicity like $e_R^- e_L^+ \rightarrow e_L^- e_L^+$, $e_R^- e_R^+ \rightarrow e_L^- e_L^+$.etc.

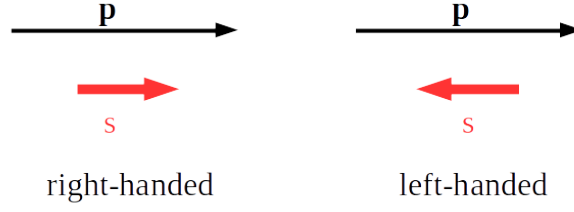


Figure 3.9. Helicity state of a spin $-1/2$ particle. The arrows with p represent the direction of motion of the particle and s_p shows spin of the particle

At high energies, this means $E \gg m$, only 4 non-zero helicity combinations come out. For $e_R^- + e_L^+ \rightarrow \mu_R^- + \mu_L^+$, the possible helicity combination is given as,

$$e_R^- e_L^+ : (j_e) = \bar{v}_\downarrow p_2 \gamma u_\uparrow p_1 = 2E(0, -1, -i, 0) \quad (3.6)$$

$$\mu_R^- \mu_L^+ : (j_\mu) = \bar{u}_\uparrow p_3 \gamma v_\downarrow p_4 = 2E(0, -\cos\theta, i, \sin\theta) \quad (3.7)$$

For this combination, matrix elements are represented as M_{RR} where the first subscript R defines the electron helicity and second subscript R gives the μ^- helicity.

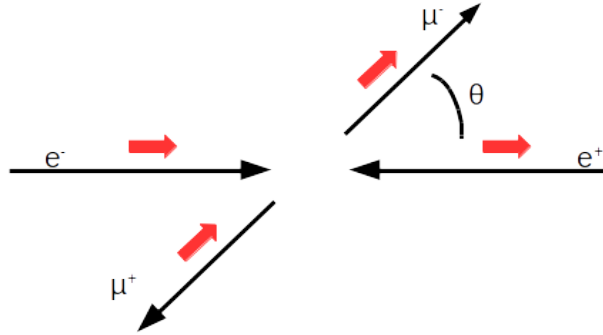


Figure 3.10. Schematic representation of the one of the helicity combination for the $e^+e^- \rightarrow \mu^+\mu^-$ process

In this case, matrix element is given as,

$$M_{RR} = -\frac{e^2}{s} [2E(0, -1, -i, 0) \cdot 2E(0, -\cos\theta, i, \sin\theta)] \quad (3.8)$$

$$M_{RR} = -4\pi\alpha(1 + \cos\theta), \quad \alpha = \frac{e^2}{4\pi} \approx \frac{1}{137} \quad (3.9)$$

where M_{RR} represents the initial state for e^- and final state for μ^- , θ is the emission or scattering angle. Similarly, for the other combination the matrix is given as in the following equation

$$M_{LR} = -4\pi\alpha(1 - \cos\theta) \quad (3.10)$$

When the sum of the square root of the matrix elements $|M_{RR}|^2 = |M_{LL}|^2$ and $|M_{LR}|^2 = |M_{RL}|^2$ is placed in Equation 3.2, it gives the differential cross section as in Equation 3.11.

$$\frac{d\sigma}{d\Omega} = \frac{\alpha^2}{4s}(1 + \cos^2\theta) \quad (3.11)$$

Total cross section is calculated by the integration over θ and ϕ for the process $e^+e^- \rightarrow \mu^+\mu^-$ as in Equation 3.12.

$$\sigma = \frac{\alpha^2}{4s} \int (1 + \cos^2\theta) d\Omega = \frac{\pi\alpha^2}{2s} \int_{-1}^{+1} (1 + \cos^2\theta) d\cos\theta = \frac{4\pi\alpha^2}{3s} \quad (3.12)$$

The total cross section equation is impressively in a good agreement with the PETRA (Positron-Elektron Tandem Ring Accelerator) experiment results [Gaillard 1985]. The PETRA experiment is an accelerator where electron and positron beams are accelerated up to 19 GeV.

Muon production with positron-electron annihilation have defined as **AnnihToMu** in GEANT4 electromagnetic package. In Figure 3.11, the energy distribution of muons, which have been generated by impinging on 1.5 TeV electrons and positrons to target material, is represented. In this simulation, the incoming particles impinge on Ti target, which has $1 X_0$ (radiation length is about 3.56 cm) thickness, and generate muon pairs with electromagnetic process. The energy distribution of muons generated by the annihilation (AnnihToMu) process have been represented by the red line and gamma conversion into muon pair (GammaToMuPair) production process has been represented by the black line in Figure 3.11. The dashed lines indicate that the incoming particle is electron. The solid

lines indicate that the incoming particle is positron. When the incident particle is positron, the AnnihiToMu process is dominated but the energy of generated muons is higher than the AnnihiToMu process.

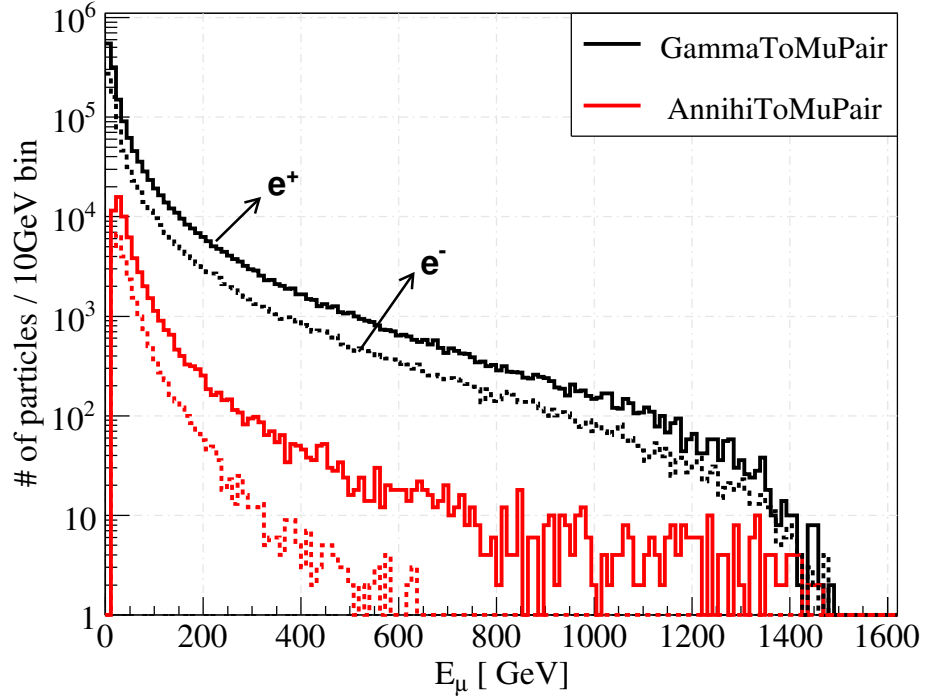


Figure 3.11. Energy distribution of muons from GammaToMuPair and AnnihiToMuPair process for 1.5 TeV electron and positron beam

3.2.3. Annihilation into Hadrons

Positron-electron annihilation into hadrons process contributes to muon production indirectly. In this process, the generated hadrons, which have short life time, may decay into muon pairs. Therefore, they contribute to energetic muon background source.

Energetic positrons annihilate with the atomic electron in collimator material and can create hadrons depending on incident beam energy. In GEANT4 electromagnetic package, this process is defined as **eeToHadrons** and five hadron production models are defined.

The energetic positron beam interacts with the electrons which are bounded in the collimator material. For these processes, the electron energy is relatively small in compared to the positron energy $E_{e^+} \gg m_{e^-}$. In this case, the center of mass energy for the interaction is

calculated with $\sqrt{2 \cdot m_{e^-} \cdot E_{e^+}}$. For the CLIC project, the highest beam energy have been planned as 1.5 TeV. Therefore, in Figure 3.12 and Figure 3.13 the highest center of mass energy becomes at about 1.3 GeV.

In Figure 3.12, the cross section values with respect to the center of mass energy have been given for the annihilation into hadrons ($e^+e^- \rightarrow \text{hadrons}$) process. The peaks correspond to mesons; $\rho(770)$, $\omega(782)$ ve $\phi(1020)$, respectively. The decay channels of these mesons are given in Table 3.1.

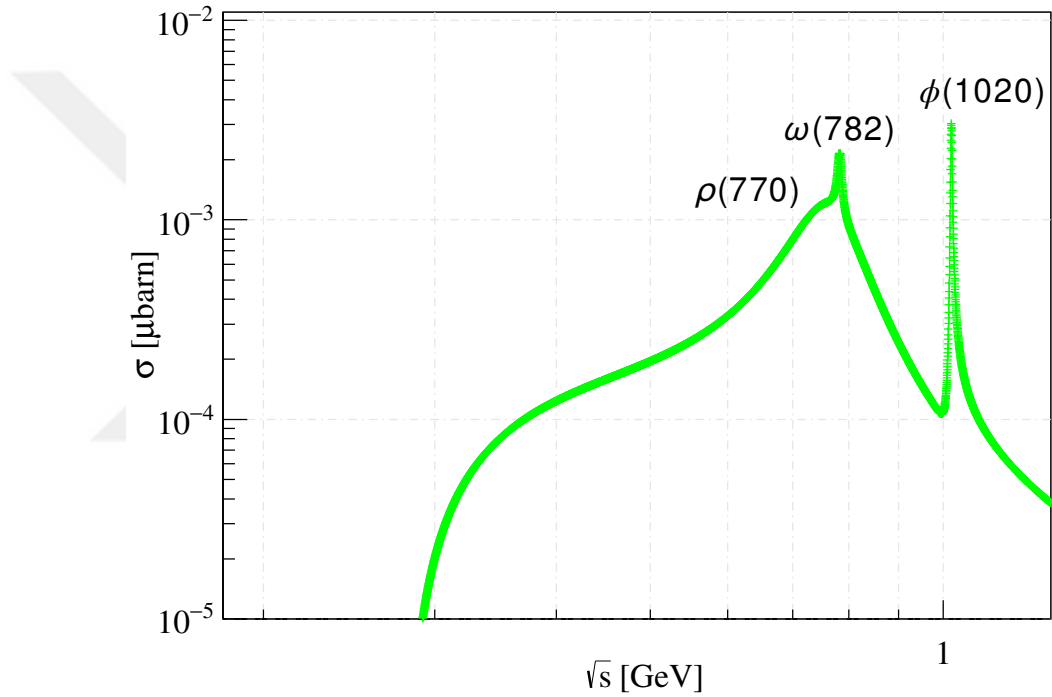


Figure 3.12. The cross section of annihilation into hadrons ($e^+e^- \rightarrow \text{hadrons}$) process with respect to center of mass energy values

In GEANT4 electromagnetic package, there are 5 different hadron models in **eeToHadrons** model. The cross section values for center of energy mass are given in Figure 3.13. eeToHadron process contains $\pi^+\pi^-$ (G4eeToTwoPiModel), $\pi^+\pi^-\pi^0$ (G4eeTo3PiModel), $\pi^0\gamma$ (G4eeToPGammaModel), $K_L^0K_S^0$ (G4ee2KNeutralModel), K^+K^- (G4ee2KChargedModel). Some information about the generated hadrons from eeToHadron process is given in Table 3.2 [Olive et al 2014]. According to Table 3.2, π^0 has the shortest life time amongst other hadrons and it decays into two gamma ($\pi^0 \rightarrow 2\gamma$) with a high probability (%98.8).

Table 3.1. Generated mesons properties

Particle	Quark structure	τ (s)	Decay channels
$\rho_0(770)$	$u\bar{u}, d\bar{d}$	0.4×10^{-23}	$\pi^+ \pi^-$
$\omega_0(782)$	$u\bar{u}, d\bar{d}$	0.8×10^{-22}	$\pi^+ \pi^- \pi^0$
$\phi(1020)$	$s\bar{s}$	20×10^{-22}	$K^+ K^- K_L^0 K_S^0$

This increases the energetic photons in system and may increase the muon background by GammaToMu process. According to Table 3.2, π^+ decays into muon ($\pi^+ \rightarrow \mu^+ \nu^\mu$) with %99.9 probability. This process also has a small contribution to the muon background in the system.

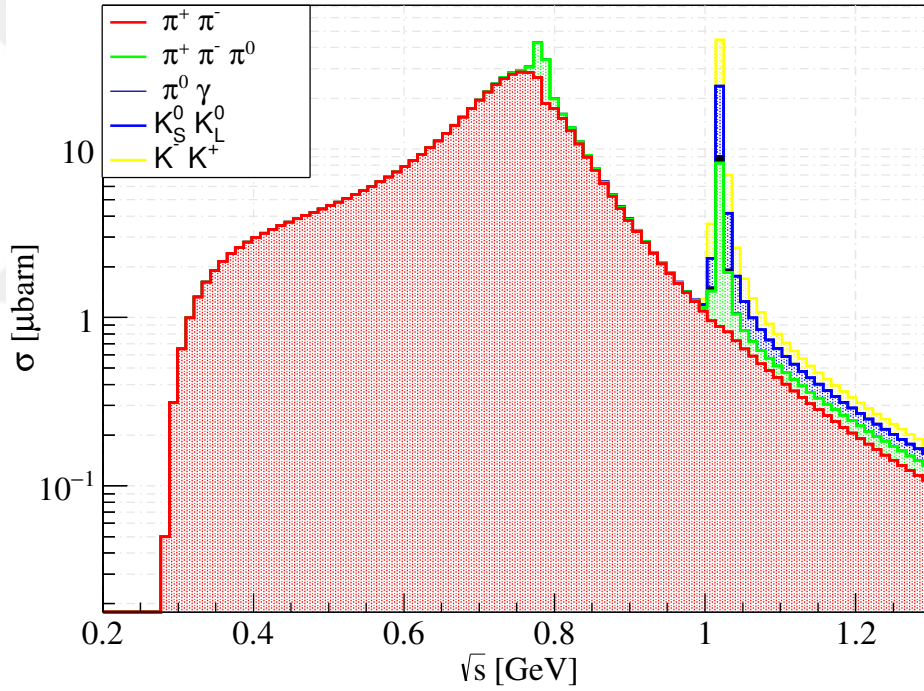


Figure 3.13. Hadron production processes and change in their cross section \sqrt{s}

Depending on lifetime of hadrons in Table 3.2 and their determined minimum energy for this decay, their decay length can be estimated. For the calculation of decay length, the equation have been used,

$$l = \gamma \cdot \tau \cdot c \quad (3.13)$$

where γ is assumed as $\gamma = E/m$, τ represents lifetime, c is speed of light. Therefore, the

Table 3.2. Lifetime of the generated hadrons from $e^+e^- \rightarrow$ hadrons process

Hadrons	τ (s)
π^+/π^-	2.60×10^{-8}
K^+/K^-	1.24×10^{-8}
K_L^0	5.11×10^{-8}
K_S^0	0.89×10^{-10}
π^0	8.52×10^{-17}

Table 3.3. Determined decay distance of generated hadrons from $e^+e^- \rightarrow$ hadrons process

Hadrons	E_{min} (GeV)	L (m)
π^+/π^-	15	838
K_L^0	300	924236
K_S^0	300	16.2
K^+ / K^-	300	2256

calculated minimum travel distance of hadrons have been given in Table 3.3 with the determined minimum energy values of hadrons. By considering the distance between the betatron collimation and interaction region, which is about 1 km long, π^+, π^-, K_S^0 have higher probability to decay. The simulation studies have showed that the other generated hadrons lose their energy easily without decaying in accelerator system.

The ratio of annihilation into muon pair ($e^-e^+ \rightarrow \mu^-\mu^+$) to annihilation into hadrons ($e^-e^+ \rightarrow$ hadrons) have been given in Figure 3.14. The peak values are corresponds to vector resonance masses. The first two peaks at around the 600 GeV represents $\rho(770)$ ve $\omega(782)$ mesons, respectively. The peak at around 1 TeV beam energy indicates $\phi(1020)$.

Consequently, generated muons from annihilations into hadrons as a background source increase slightly at the peak values which correspond to 500 GeV, 600 GeV and 1 TeV positron beam energy. The comparison of performed simulation results for cross section (Figure 3.14) with the cross section values in PDG (Particle Data Group), which have been given in Figure 3.15, shows a good agreement.

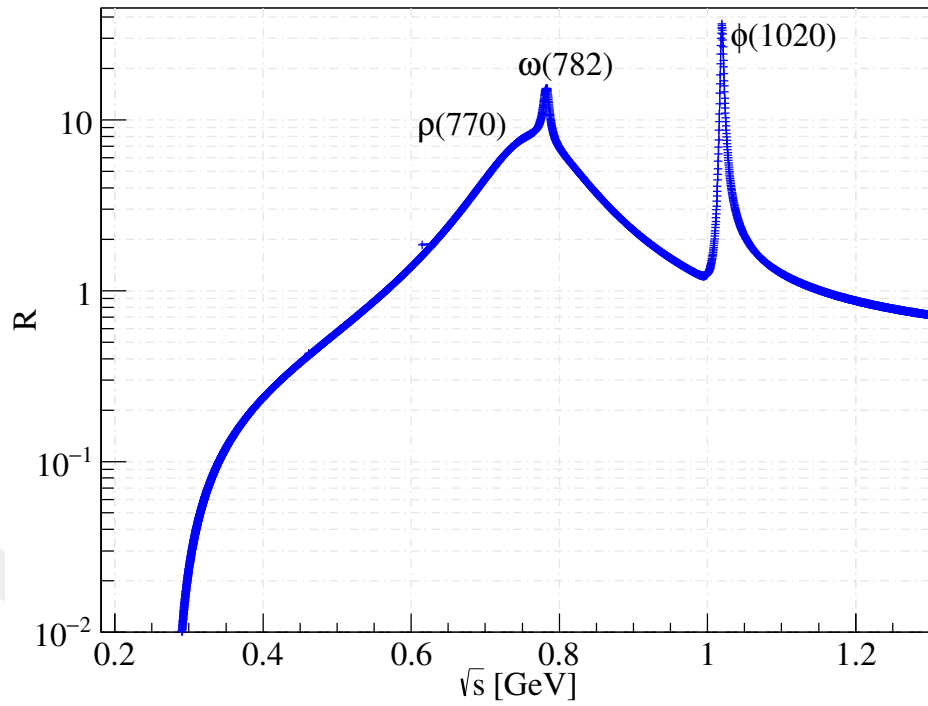


Figure 3.14. The ratio of cross sections as a function of center of mass energy.

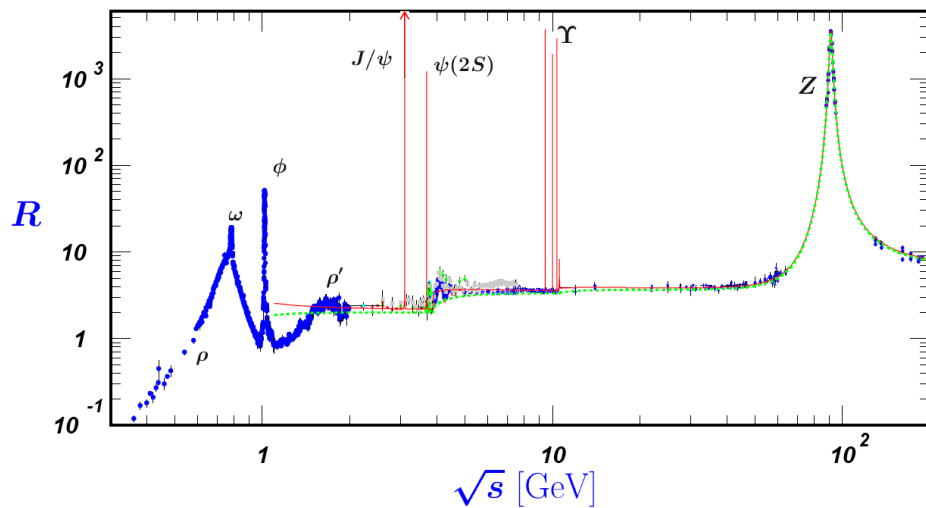


Figure 3.15. The cross section ratio values $R = (e^+e^- \rightarrow \text{hadrons}, s) / (e^+e^- \rightarrow \mu^+\mu^-, s)$ collected from the world wide experiments [Olive et al 2014]

4. SIMULATION RESULTS

In this section, Beam Delivery Simulation (BDSIM), which is a C++ based software and contains GEANT4 physics package, has been used to trace halo and/or beam particles through the BDS.

The whole BDS geometry, which is almost 2800 m long and consists of various magnets, have been constructed by taking the advantage of GMAD [Agapov 2006] (Geometry for Methodical Accelerator Design) geometry description language. Afterwards, the simulations have been performed to estimate the muon potential through the detector side. By this way, the amount of muons reaching to the end of the BDS have been estimated, computationally. As a second part, magnetized muon shielding modules have been placed in order to decrease the amount of generated muons, which may reach to the BDS. The magnetized muon shielding parameters (like magnetic field strength, dimensions and its position, etc.) have been optimized by means of simulations with BDSIM to reduce them effectively.

4.1. CLIC Beam Delivery System Simulation

After accelerating to the full beam energy in the LINAC, the beam enters the BDS which is about 2800 m long beam transfer line. The twiss parameters and the layout of out the BDS were shown graphically in Figure 1.6 and Figure 2.4, in Chapter 1 and in Chapter 2, respectively. First section of the BDS is diagnostic section which is roughly 450 m long, consists of focusing and defocusing quadrupoles to measure and correct the parameter of beam which is coming from main LINAC. The beam then traverses the energy collimation section, where off-momentum particles are removed. It is almost 1250 m long and contains dipole (bending magnet) sections and collimators to clear away off-momentum particles. Of particular interest for this study is the third section, the betatron collimation section, which is designed to remove halo particles. The betatron collimation section is placed before final focus and almost 400 m long. This section is important to eliminate halo

particles by using spoilers and absorbers, for both horizontal and vertical planes. The final focus section is placed after betatron collimation section to obtain clean beam in the interaction region. Finally, the cleaned beam from halo particles reaches to the final focus section to demagnify to the desired parameters with very strong magnets at the end of the BDS [Aicheler et al 2012].

A view of small portion of BDS have been shown in Figure 4.1 from BDSIM visualizer. BDSIM uses Open GL Qt as a default visualization driver. The red, blue and yellow elements indicates quadrupoles, bending magnets and sextupoles, respectively and the grey one residing very thin in central line is the beam pipe in Figure 4.1.

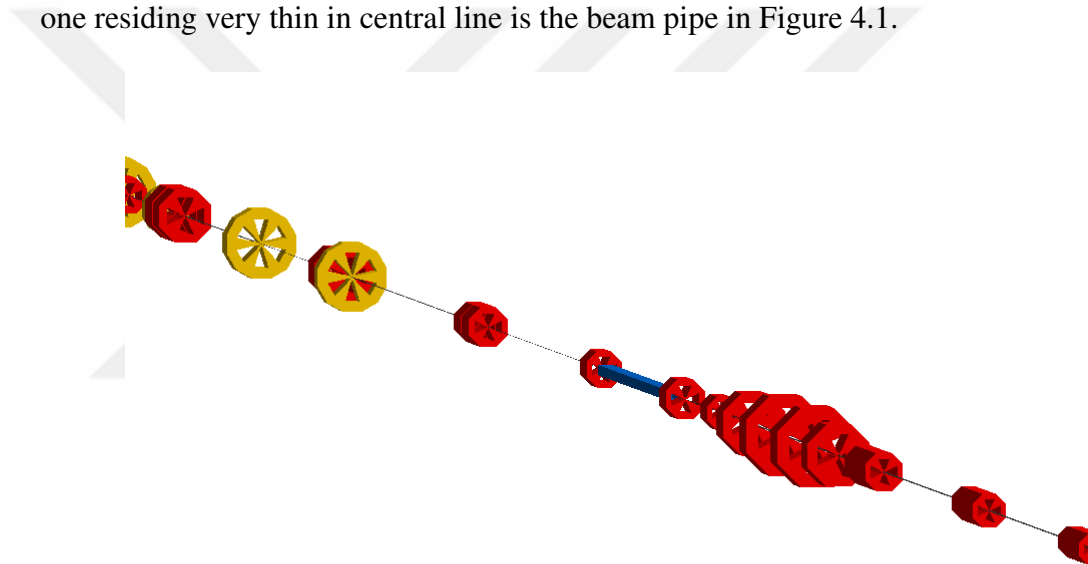


Figure 4.1. A part of BDS geometry which have been generated with BDSIM

The BDS was originally designed with MAD-X and mentioned in detail in CLIC CDR [Aicheler et al 2012]. By using the whole output of the program and help of the MAD-X to GMAD conversion parser of BDSIM, the designed beam line geometry can be converted to GMAD style easily in order to use in BDSIM. BDSIM uses GMAD, which is a MAD extension language, for the description of beam line components, beam and other properties [Agapov et al 2009]. The component definition format of the elements via text file in the GMAD

language have been given in Appendix 1. Various type of elements can be described with BDSIM. A detailed description about the other types of elements can be found in BDSIM Manual [BDSIM Collobration 2015].

4.2. Tracking and Optics

BDSIM typically uses 4th order Runge-Kutta method for the computation of magnetic field steppers as in GEANT4 and 6D tracking routines as in MAD-X for tracking of beam particles [Agapov et al 2009]. By doing in this way, the code can track the particles down to zero energy efficiently inside the beam pipe (depending on the production cuts) inside “The World” volume with enabling the GEANT4 processes.

The particles have been tracked by using the 6D tracking routines in vacuum. The RMS beam sizes horizontally and vertically have been determined for each components of the BDS. At the starting point, the beam parameters have been defined as in Appendix 2.

The particles have been tracked through the whole BDS with BDSIM. At the starting point of the BDS, RMS beam sizes, which means the end of the main LINAC, are 3.9 μm and 0.35 μm both horizontally and vertically. When the particles reach to the IP, the RMS beam sizes are roughly 41 nm and 1 nm both horizontally and vertically. The simulation results of the beam sizes are consistent with the required beam size parameters as mentioned in Ref [Aicheler et al 2012]. The RMS beam sizes for each element have been compared with the MAD-X results as shown in Figure 4.2. The RMS beam size values are in good agreement with MAD-X and BDSIM as shown in Figure 4.2. By this way, the construction of geometry with BDSIM have been verified.

The estimated trajectories of the particles along the BDS are shown in Figure 4.3. The betatron oscillations are significant especially at the energy collimation and final focus sections where long bending magnet parts are present.

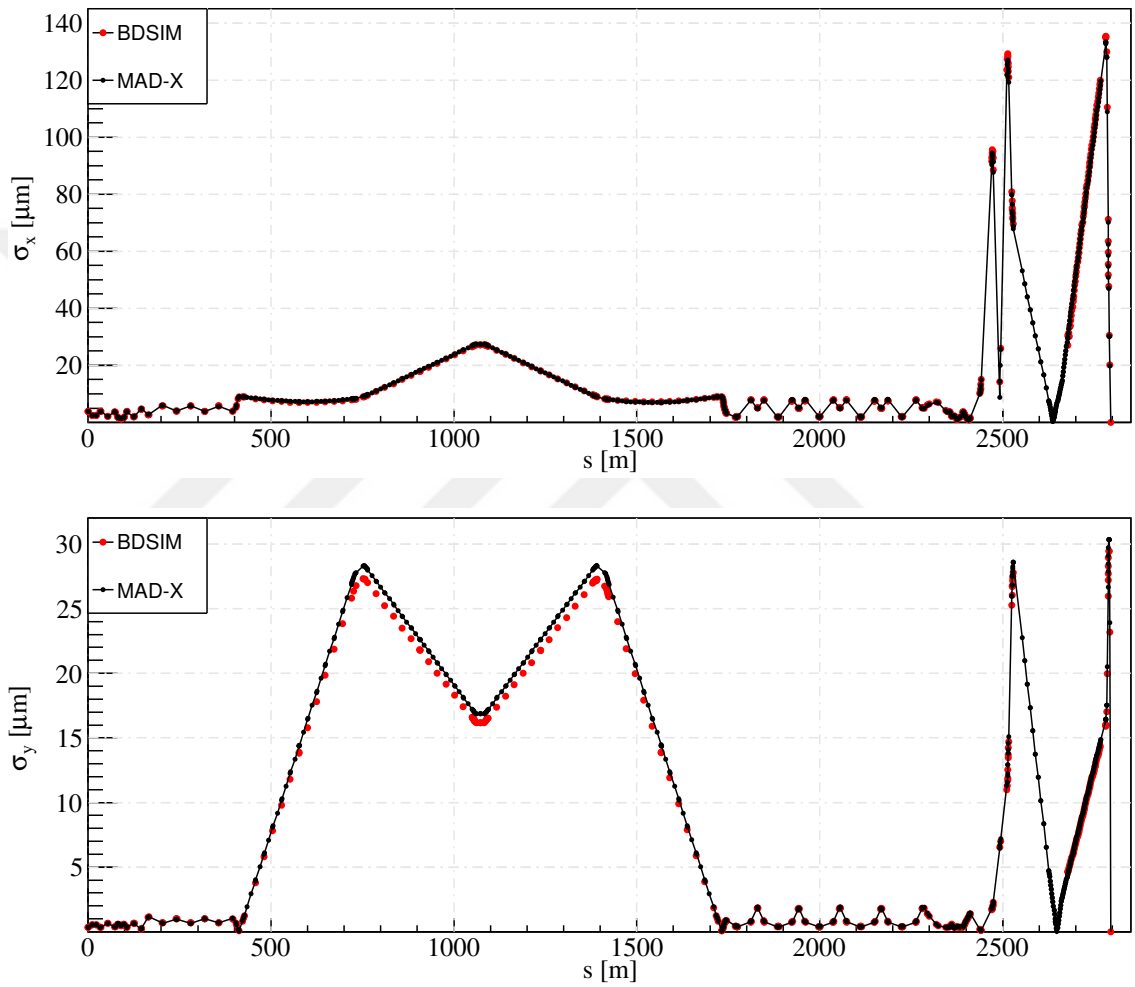


Figure 4.2. Comparison of horizontal and vertical RMS beam size results obtained from MAD-X and BDSIM along the beamline

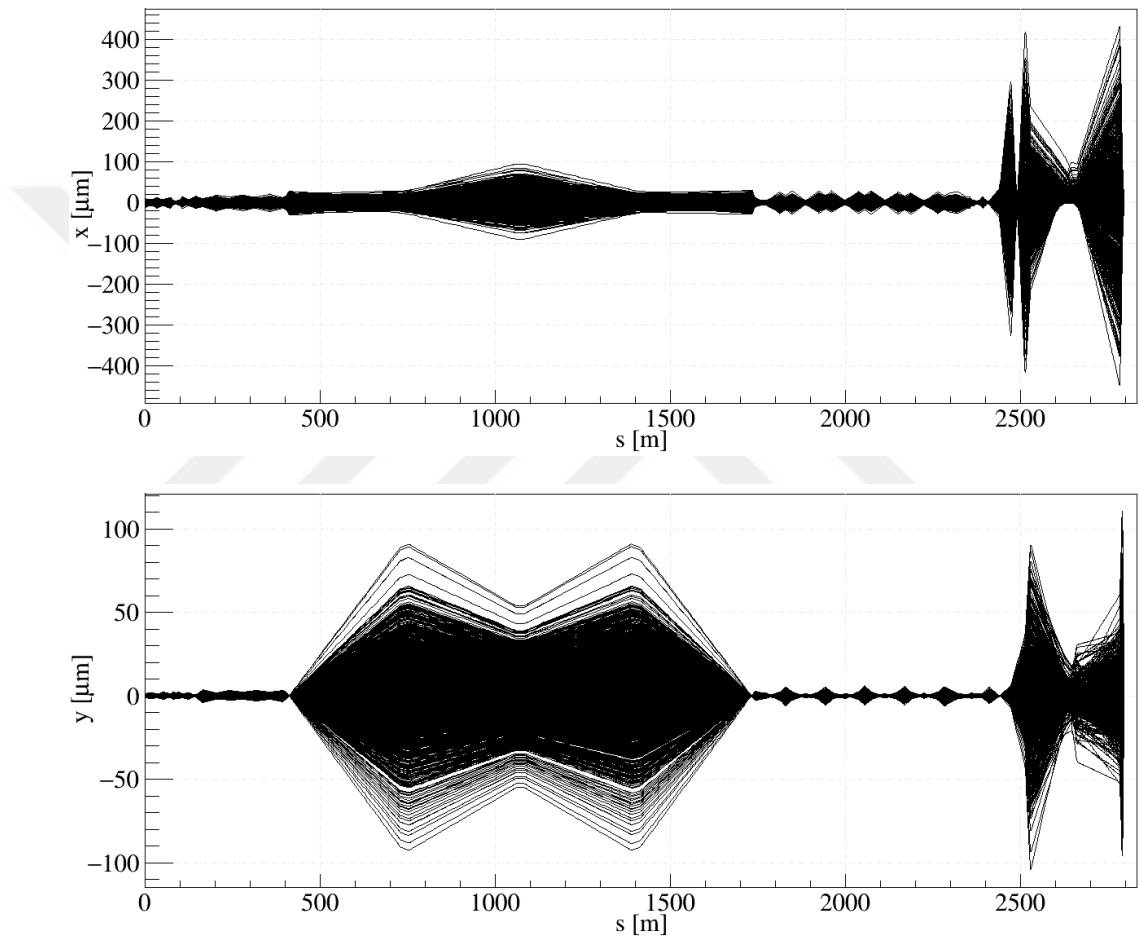


Figure 4.3. Estimated particles trajectories along the BDS by using BDSIM

4.3. Muon Tracks in BDS

The main source of muon background is the betatron collimation section due to cleaning away halo particles. The betatron collimation section consists of four sets of spoilers and absorbers. The schematics of the spoiler and absorber have been represented in Figure 4.4. The drawings in Figure 4.4 are not scaled proportionally and shown only for illustration purpose. The spoilers are thinner element when they are compared with absorbers. Spoilers are approximately 7.2 mm ($\sim 1 X_0$) thick and absorbers are 648 mm ($\sim 10 X_0$) thick. Table 4.1 shows the parameters of each spoilers and absorbers where a_x , a_y are half aperture values for them and L_T represents the thickness of absorber edges while L_F represents the thickness of absorber core.

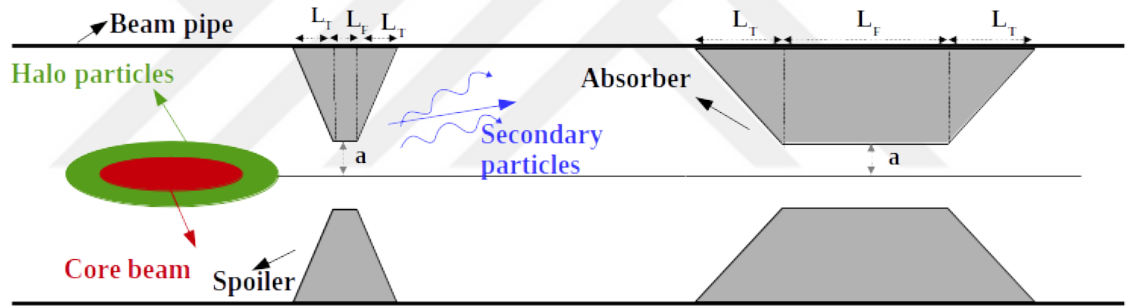


Figure 4.4. Schematics of the spoiler and absorber couple in betatron collimation section

In order to understand the muon generation and their behaviour along the beam line, preliminary assumption is to hit the halo particles to the edge of the first spoiler (YSP1) artificially by using BDSIM. For the simulations, radius of the tunnel walls has been taken

Table 4.1. Some parameters about spoilers and absorbers

Spoilers	a_x [mm]	a_y [mm]	L_T [mm]	L_F [mm]	Material
YSP1,2,3,4	8.0	0.1	90.0	7.2	Ti-Cu
XSP1,2,3,4	0.1	8.0	90.0	7.2	Ti-Cu
Absorbers	a_x [mm]	a_y [mm]	L_T [mm]	L_F [mm]	Material
XAB1,2,3,4	1.0	1.0	27	648	Ti
YAB1,2,3,4	1.0	1.0	27	648	Ti

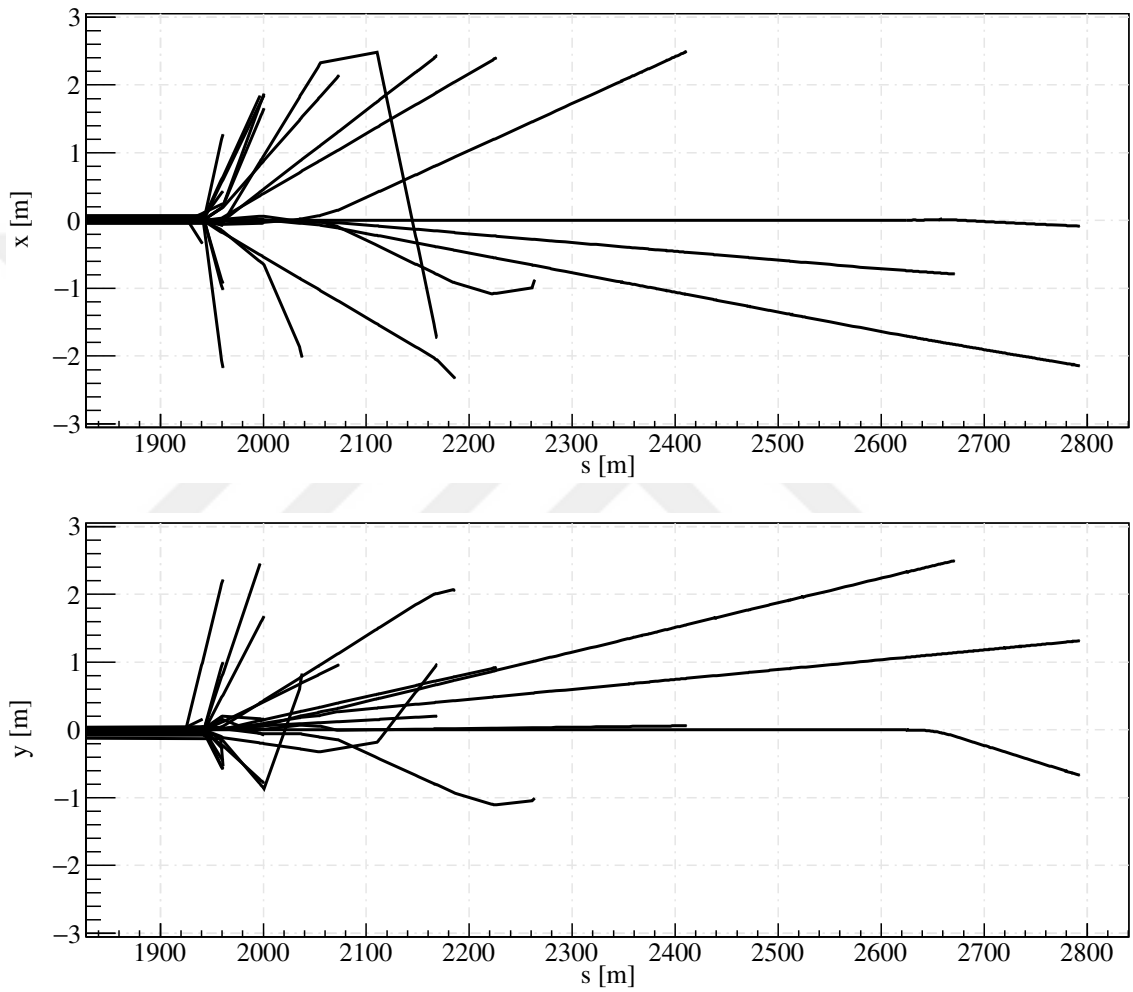


Figure 4.5. Sample muon tracks which are generated by hitting to the first spoiler YSP1 through the beamline

3 m as illustrated in Figure 4.5. When the halo particles hit to the first spoiler (YSP1), which is very thin object of several mm thickness, the halo particles are scattered by interacting the first spoiler through the absorber due to bremsstrahlung and/or ionization processes. The secondaries reach to the absorbers which are relatively thick objects of several hundred mm. The energetic secondary and/or halo particles, which reach the absorber, interact with the absorber material and cause to generate muons as a background source. The background muons lose a small amount of energy along the beam line. The trajectories of the background muons have been plotted in Figure 4.5 by tracing them along the beam line. The background muons mostly travel through the tunnel wall. However, a few of them, which are generally energetic muons, reach to the detector side inside the tunnel wall.

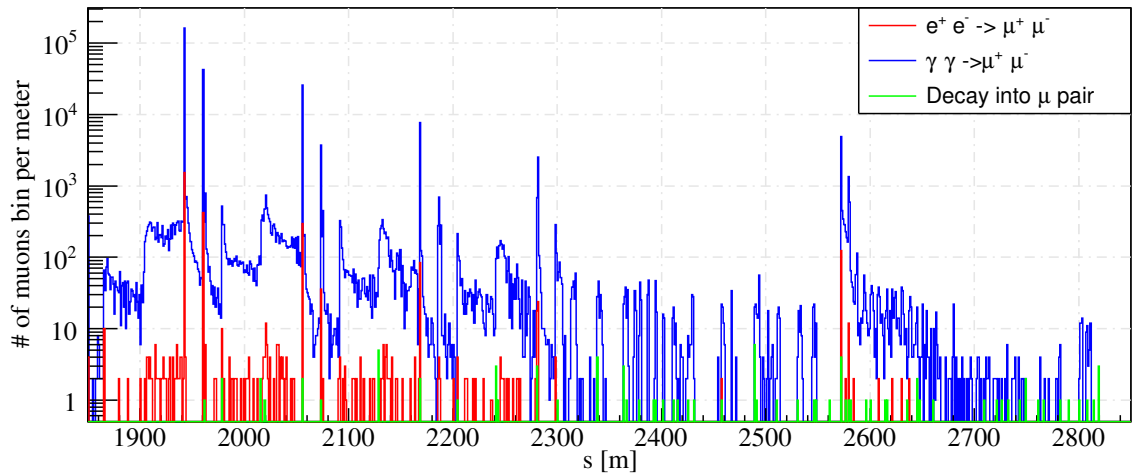


Figure 4.6. The origin of muons from betatron collimation section to end of BDS and their creation process

By hitting 10^9 halo particles (e^-) to the first spoiler, the muon generation points and their generation processes are specified as shown in Figure 4.6 by extracting their information from the help of the simulation with BDSIM. Energy distribution of the halo particles have been taken as 1.5 TeV and they have been hit to the edge of the first spoiler. The peak positions before 2300 m correspond to the positions of the absorbers in Figure 4.6. The peak about 2630 m matches up to starting point of the long bending part of the final

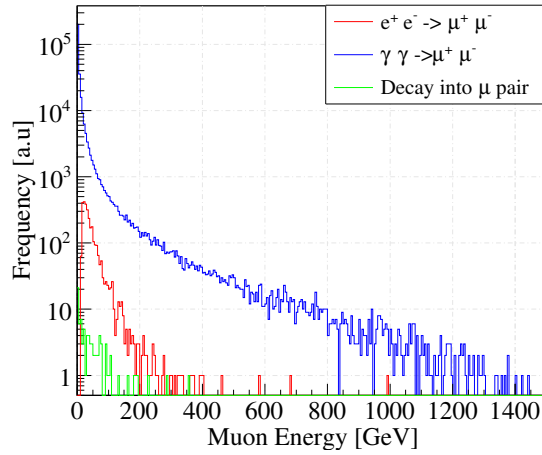


Figure 4.7. Energy distribution of of the generated muons

focus. In this part, the aperture size of the bending magnets are narrower thus this slightly increases the generation of muons. Otherwise, the gamma conversion into muon process ($\gamma + \gamma \rightarrow \mu^+ + \mu^-$) is more dominant process than others for e^- as shown in Figure 4.6. The energy distribution of the generated muons from different processes have been shown in Figure 4.7. Figure 4.7 also points out that their energy is mostly below 200 GeV but a few of them have higher energies up to about 1.5 TeV.

The amount of muons arriving at the surface of the each element are placed along the BDS, have been shown in Figure 4.8 for 312 bunch crossings. The first peak around 1900 m corresponds to position of the first absorber (XAB1) in Figure 4.8. This means that the hitting particles to the first spoiler result in the generation of muons around the first absorber. Thereafter, the amount of muons decrease exponentially through the end of the beam line. The last peak around 2600 m corresponds to the starting point of the bending magnets on final focus. The reason of this peak is that the energetic photons are not affected by the magnetic field. As they reach the starting point of these bending magnets, they hit them due to their narrower aperture. This process increases the muon production. Almost 40 muons reach to the end of the BDS.

If we evaluate the results statistically, each bunch have about 4×10^9 particles. The results from HTGEN show that 2×10^{-4} fraction of bunch particles hit the first spoiler (YSP1). This is roughly 8×10^5 halo particles for bunch crossings. The fraction of muon generation

from hitting particles to the first spoiler is roughly 1.5×10^{-3} . About %3.3 of muons reach to the end of the BDS from inner part of the tunnel wall.

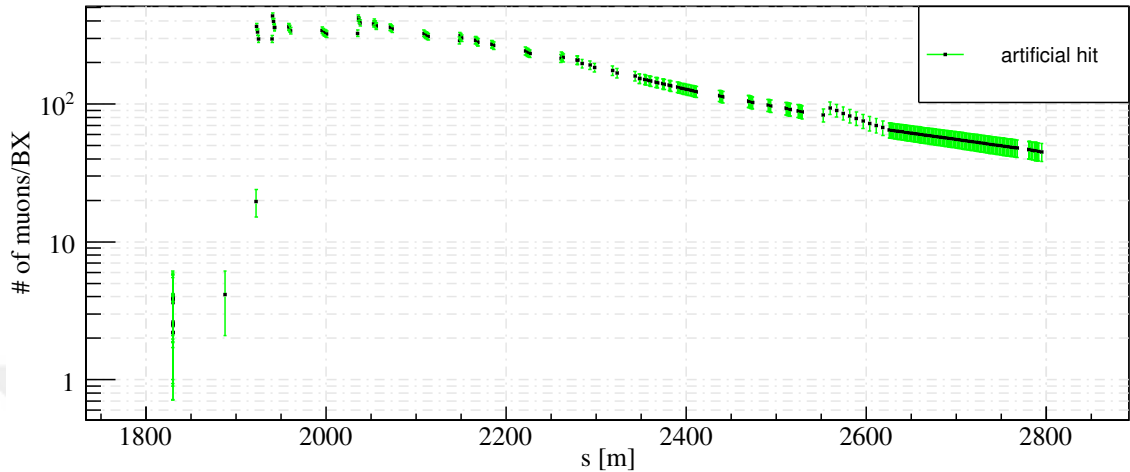


Figure 4.8. The amount of muons along the BDS

On the other hand, the distribution of halo particles, which is obtained from HTGEN, is shown in Chapter 3, Figure 3.2. In this work, the other scenario is to use this halo particle distribution at YSP1 as an input in BDSIM. The halo particles, which have a distribution as in Figure 3.2, hit the first spoiler YSP1. The muon distribution along the BDS have been shown in Figure 4.9.

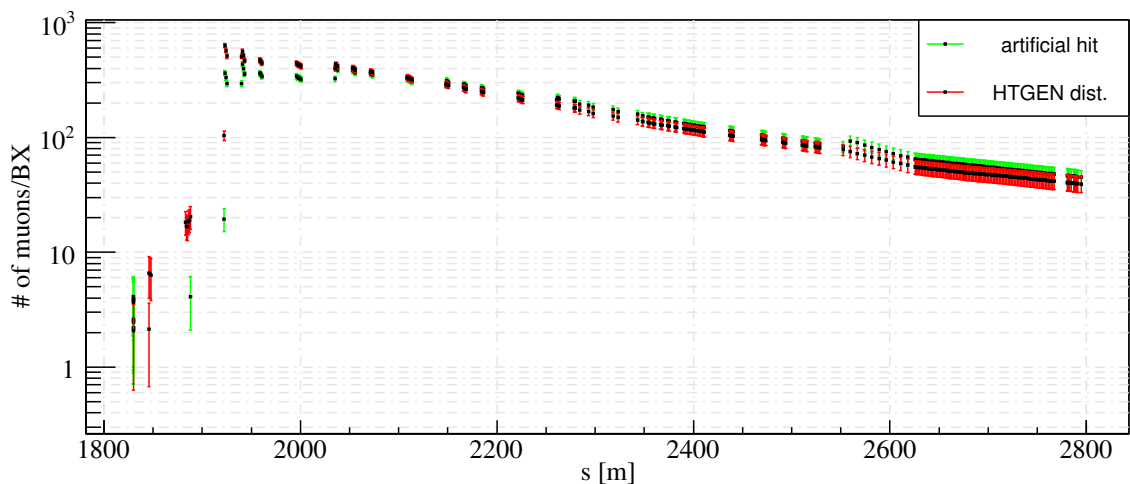


Figure 4.9. The comparison of the amount of muons in BDS for both case artificial hitting to first spoiler (green error bars) and using HTGEN distribution at first spoiler (red error bars)

Figure 4.9 shows that the amount of muons along the BDS. For both options the behavior of the muons is almost the same. According to the simulation results in Figure 4.9, the green markers indicate that almost 45 ± 7 muons reach to the end of the BDS while the red markers, which are the case when halo distribution has been used as the primary source of particles hitting to the first spoiler (YSP1), indicate that almost 40 ± 7 muons reach to the end of the BDS. All these estimated muon numbers above has been normalized to one bunch crossing.

4.4. Optimization of Magnetized Muon Shielding

In order to decrease the amount of muons, which may reach to the IP, the proposed magnetized shielding structure have been studied and simulated. These structures deflect the muons to the tunnel wall to reduce the number of muons at IP.

Their structure have a cylindrical shape and toroidal magnetic field inside. In this case, according to the Lorentz Law, a force which is perpendicular to the magnetic field, will be applied to the muons; therefore, they will be deflected to the tunnel wall by the effect of the magnetic field. The schematic of the magnetized shielding have been shown in Figure 4.10. The drawing does not have a proper ratio, it is only for illustration purpose.

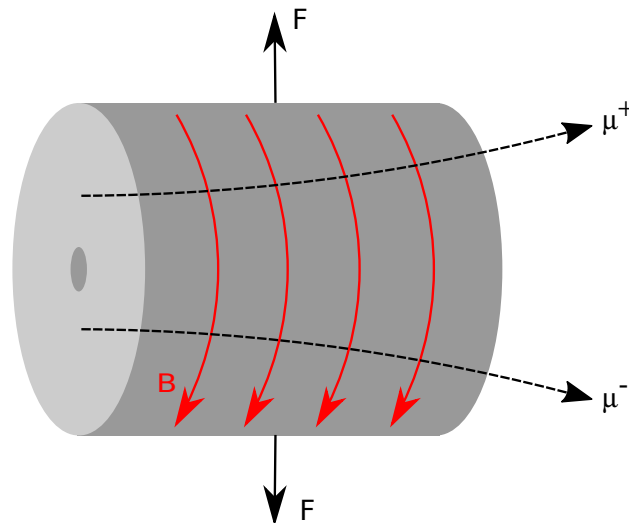


Figure 4.10. The schematic of the magnetized muon shielding which has a toroidal magnetic field

In order to place the magnetized shielding effectively, the origin of the muons simulated as in Figure 4.6 have been taken into account. The magnetized shieldings have been positioned to the existing drift spaces after the absorbers in betatron collimation section. The magnet parameters for the BDS can be found in Ref [Aloev and Modena 2012]. According to Ref. (CLIC Technical Note) [Aloev and Modena 2012], the outer radius of magnets in betatron collimation section alters around 35 cm. From this information, the deflection of muons by hitting to the magnetized muon shielding has been calculated. The radius of deflected muons can be calculated with Equation 4.1. The particles are relativistic so β is equal to 1.

$$R = 3.33 \cdot \frac{\beta \cdot p [GeV/c]}{B [T]} \quad (4.1)$$

The schematic of the deflected muons have been shown in Figure 4.11. In order to deflect muons properly, the distance between magnetized muon shielding and magnet should be considered. The betatron collimation section is a periodically aligned section. The distance between magnetized shielding and magnet is about 30 m. Considering this layout, the amount of deflection and deflection angle have been simulated for different muon energies. Figure 4.12 (left) shows the amount of deflection of muons with respect to the incident muon under different magnetic field strengths. For instance, a 5 m long massive shielding, which means that it has no field and represented with black markers, can deflect 60 GeV muons about 30 m after 35 m but muons, which have 200 GeV energy, can be deflected only 9 m after 35 m with the same massive shielding. The amount of deflection increases with magnetic field. By considering the energy distribution of muons as in Figure 4.7, most of the muons have energy less than 200 GeV. Figure 4.12 (right) shows the deflection angle of the muons with respect to the incident muon energy under different magnetic field strengths. Considering the muons with 200 GeV energy, the deflection angle varies from 3 mrad to 25 mrad for the cases of massive shielding and 3 T magnetic field, respectively.

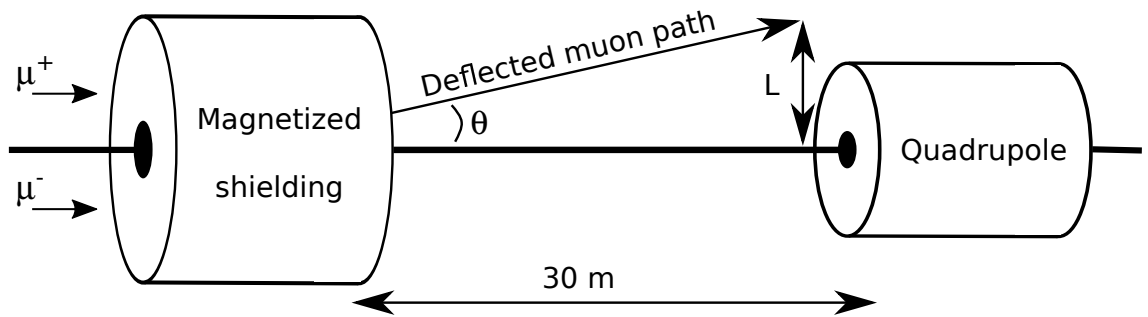


Figure 4.11. Schematic of the deflected muons from magnetized shielding

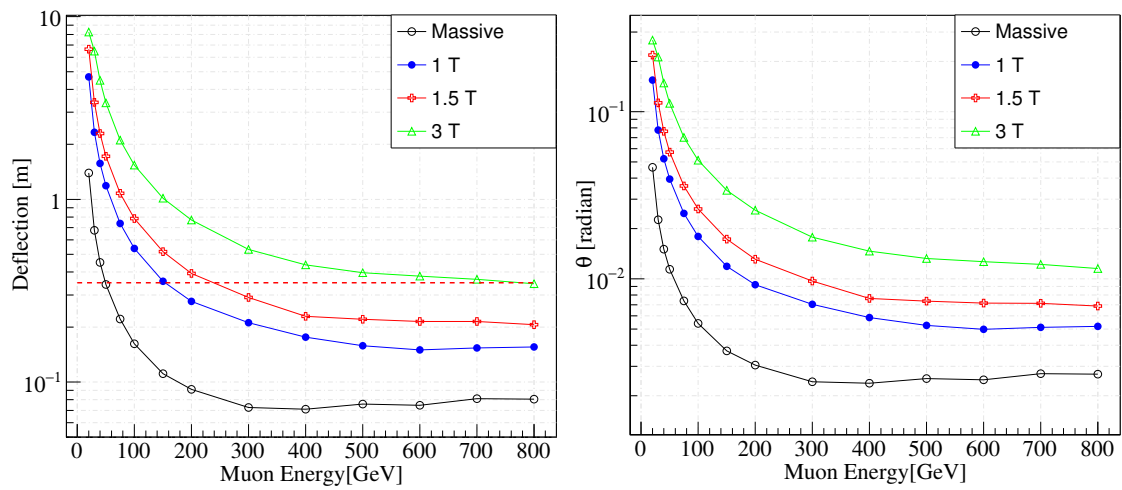


Figure 4.12. The amount of deflection (left) and deflection angle (right) depending on incident muon energy and magnetic field of shielding

It shows that 1 T magnetic field is enough to deflect muons, which have energy up to 200 GeV energy, through the tunnel wall. On the other side, the outer radius of the magnets in the BDS is around 40 cm. By considering this compact magnets, the magnetized shielding outer radius has been found around 60 cm instead of making them as tall as the tunnel wall. This option is both practical for deflection of muons and cost effective by comparing to tunnel filler option. The literature reviews show that magnetized muon shielding like tunnel filler have been used for SLAC (Stanford Linear Accelerator) [Keller 1993]. Tunnel fillers also require bypass lines for connection so these bypass lines increase the cost substantially.

According to simulation results, the outer and inner radius of the magnetized muon spoiler have been found 60 cm and 4 cm, respectively. They have been divided into 2.5 m long modules. The distance between the modules is 10 cm. The reasonable magnetic field values have been obtained with OPERA [OPERA 2016] simulations performed by A. Alov [Alov et al 2016]. In simulations, a cylindrical block with an inner radius of 4 cm and outer radius of 60 cm with 2.5 m length is considered as a magnetized shielding. Two magnet options for magnetized muon shielding have also been considered. One option is to use permanent magnets while the other option is to use normal conducting magnets. It is also important to know about the advantages and disadvantages of the following options. The permanent magnet option with Sm-Co blocks do not have power consumption however permanent magnet assemble is difficult and the average magnetic field value depends on the remanence of Sm-Co blocks. On the other hand, the normal conducting magnet is a power consuming magnet and it is around 120 W for as single 2,5 m module. Total current value is at about 2.2 kA ampere-turns (NI). The current density is 0.8 A/mm^2 and these values allow the air cooling system. Technically, the magnet requires gap between the vacuum chamber and the yoke inner radius to accommodate the coils. Therefore, the field is low in this gap.

For the changes of magnetic field values with respect to the radius of magnet have been

given in Figure 4.13. Sm-Co (Samarium-Cobalt) blocks have been used for simulations. In Figure 4.13, the change in magnetic field strength have been represented for 2, 4, 8 and 16 Sm-Co blocks. When two Sm-Co blocks have been used, the magnetic field strength varies between 0.7 T and 1.5 T. When the number of Sm-Co blocks is increased, the magnetic field fluctuation decreases. For the 16 Sm-Co blocks, magnetic field strength is of the order of 1.2 T and a small fluctuation around this value has been observed in the simulations.

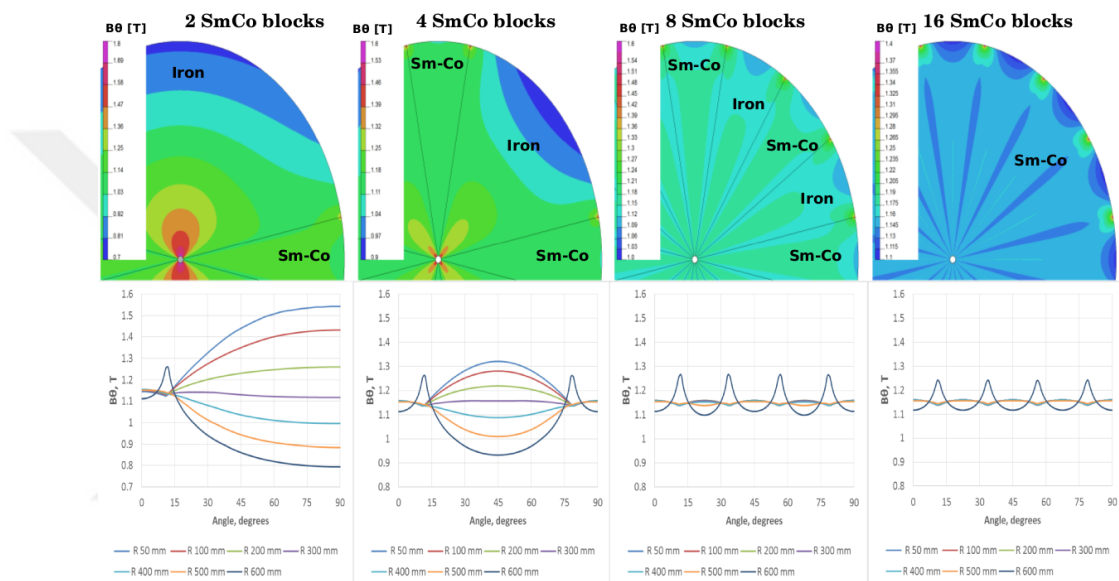


Figure 4.13. Changes in magnetic field for different number of Sm-Co (Samarium-Cobalt) blocks [Aloev et al 2016, Aloev et al 2015]

For the normal conducting magnet option, the magnetic field changes with the radius of magnet have been represented in Figure 4.14. Magnetic field decreases from inner to outer region. The magnetic field strength varies between 1.2 T and 1.7 T. When compared with the permanent magnet option, the normal conducting magnet option provides a better field homogeneity. The azimuthal field homogeneity ($B\theta$) is below 10^{-3} between the mentioned radius values.

As a result of the simulations, it has been obtained that the minimum magnetic field strength is around 0.7 T while the optimum magnetic field is around 1.2 T. Consequently, magnetic field strength for muon shielding has been chosen 0.7 T and 1.2 T for BDSIM

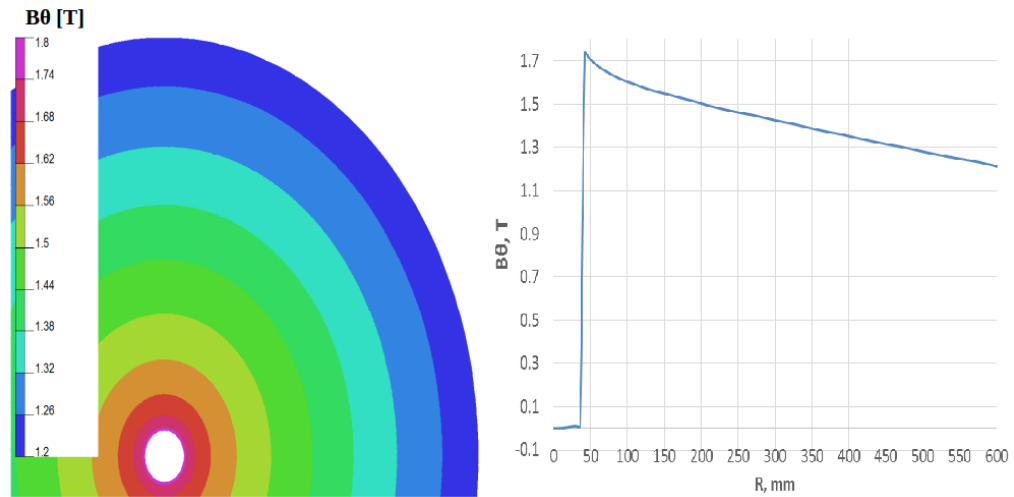


Figure 4.14. Magnetic field changes for normal conducting magnet option [Aloev et al 2016, Aloev et al 2015]

simulations.

4.5. Muon Sweeping

Prior to the implementation of the proposed designs and schematics of magnetized shielding in BDSIM, muon background studies previously performed by L.Deacon [Deacon et al 2012] have been investigated deeply. Some bugs in the previous version of the BDSIM have been pointed out and then fixed within successive release version (BDSIM version 6.5) and tested with the newer version of BDSIM. Additionally, different muon shielding options have been determined and the options have been compared with the previous work.

In Figure 4.15, the red elements are spoilers, the green elements are absorbers and the grey ones represent magnetized muon shielding. The upper line, which is called no shielding, represents the alignment of the first set of spoilers and absorbers (horizontal and vertical) in betatron collimation section on the BDS without any muon shielding. There are four sets of spoilers and absorbers in BDS. The middle line contains 10 m long magnetized muon shielding in the first set. This means that it contains totally 40 m shielding in the whole betatron collimation section. The 10 m long magnetized muon shielding is divided into four modules, which are 2.5 m long, due to ease of installation. Therefore, sixteen modules, each of them 2.5 m long, have been located in betatron collimation section as

in the previous work done by L.Deacon. In Figure 4.15, the bottom line contains more shielding modules than the middle line. In the first set of spoiler and absorber, first shielding have been placed after the first horizontal absorber (XAB1) and the second one has been placed after the second vertical spoiler (YSP2). Actually, it is planned to place the second magnetized shielding after the first vertical absorber (YAB1) but there is only two meter distance between the first vertical absorber (YAB1) and second vertical spoiler (YSP2). Hence the second shielding have been located in a suitable place between the second vertical spoiler (YSP2) and second horizontal spoiler (XSP2). The bottom line contains 32 modules, each of them 2.5 m long, and 80 m shielding in total till the end of the betatron collimation section.

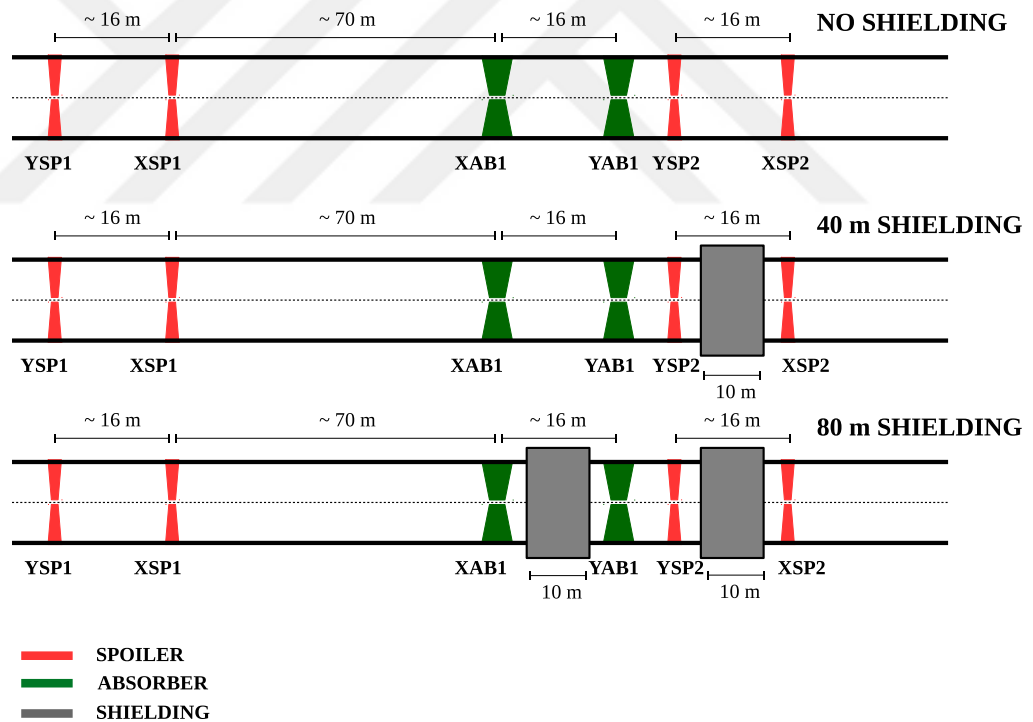


Figure 4.15. The layout of spoilers, absorbers and magnetized shielding for different options

The three options; no shielding, 40 m shielding, 80 m shielding, represented in Figure 4.15 have been simulated with BDSIM toolkit. 0.7 T and 1.2 T magnetic field values have

been considered for simulations. These magnetic field values have been determined in the consideration of the simulations performed with OPERA code [Aloev et al 2016].

The first assumption in the simulations is to hit the particles to the edge of the first spoiler, artificially. The energy of the incident halo particles to the first spoiler is 1.5 TeV. When the halo particles hit to the edge of the spoiler, they produce a secondary particle shower. In order to reduce CPU time, the production cut has been set to 1 GeV for the secondaries. This is a logical approach since we are only interested in the generated muons. Figure 4.15 schematically represents the layout of the spoilers and absorbers with different magnetized shielding options.

The muon fluxes starting from the betatron collimation section to the end of final focus has been quantitatively evaluated for 0.7 T magnetic field strength and 40 m shielding and 80 m shielding options as in Figure 4.16. The statistical calculation of error bars have been done over 500 bunch crossings. The first peak in Figure 4.16 corresponds to the position of the first absorber (XAB1). Then, some amount of muons starts to decrease exponentially because of their angular distribution. Most of the muons move towards to the tunnel wall.

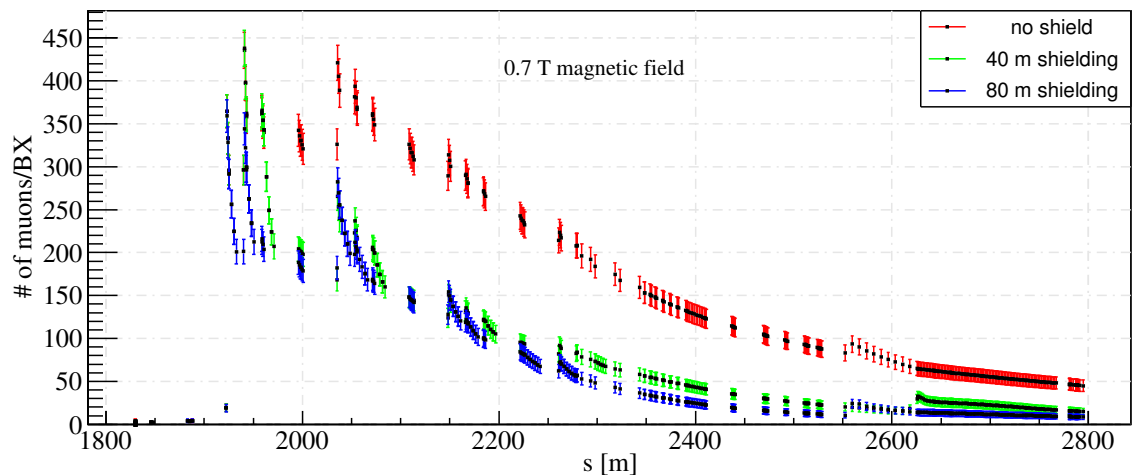


Figure 4.16. Muon fluxes for 0.7 T magnetized shielding when halo particles hit to the first spoiler

Only small amount of muons lose kinetic energy completely. Generally, the energetic muons barely lose their energy along the beam line. Almost 45 ± 7 muons reach to the

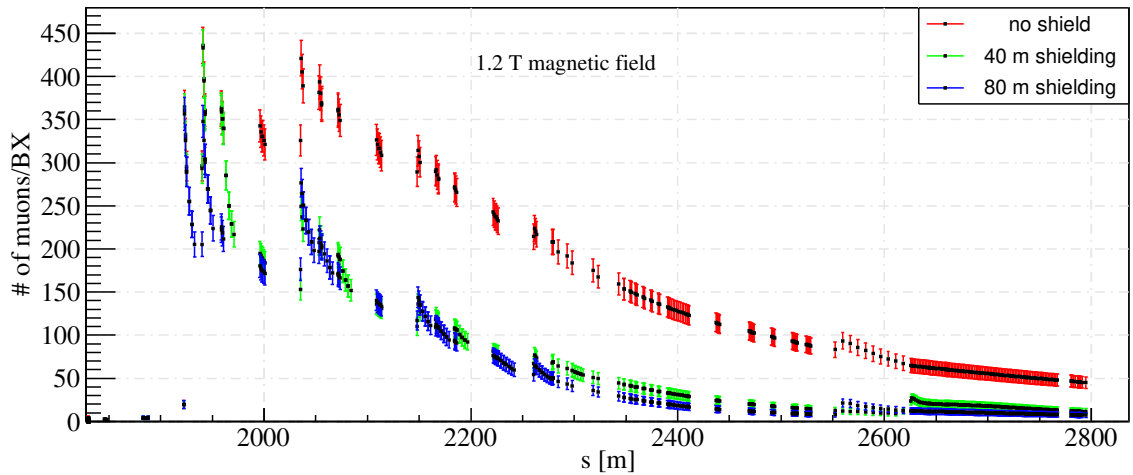


Figure 4.17. Muon fluxes for 1.2 T magnetized shielding when halo particles hit to the first spoiler

end of the BDS without using any muon shielding as shown in Figure 4.16 with the red markers. The magnetized muon shielding significantly decreases the amount of muons, which reach to the end of BDS. The green and blue markers in Figure 4.16 represent the muon fluxes for 40 m and 80 m shielding options, respectively. For 40 m shielding, almost 15 ± 4 muons reach to the end of BDS. For 80 m shielding, the number of muons decreases almost by half when compared to 40 m shielding option. Almost 8 ± 3 muons reach to the end of BDS as shown in Figure 4.16 with blue markers.

Figure 4.17 displays the behavior of muons produced along the BDS after increasing the magnetic field strength up to 1.2 T. This time, the number of muons reaching to the end of BDS is 11 ± 3 and 7 ± 3 for 40 m and 80 m shielding options, respectively. The increasing magnetic field for shielding purposes helps to decrease number of muons reaching to the end of BDS, which is summarized in Table 4.2, but not a significant decrease is obtained.

Table 4.2. The estimated amount of muons reaching to the end of BDS depending on the magnetized muon shielding parameters by using artificial hit to the YSP1

Total Length of muon shielding	magnetic field	# of muons
40 m	0.7 T	15 ± 4
40 m	1.2 T	11 ± 3
80 m	0.7 T	8 ± 3
80 m	1.2 T	7 ± 3

After all, the halo distribution, which has been obtained with HTGEN as given in Figure 3.2, has been used as a primary particle for the simulations. The results obtained from this case have been shown in Figure 4.18 and Figure 4.19. The estimated amount of muons have been given in Table 4.3. Figure 4.18 shows the muon fluxes under 0.7 T magnetic field strength. The green and blue markers indicate 40 m and 80 m shielding options. They are almost the same decrease shape. Almost 11 ± 3 and 6 ± 2 muons reach to the end of BDS for 40 m and 80 m shielding options, respectively. The increase in the amount of shielding material decreases the number of muons reaching to the end of BDS. In addition, the increase in magnetic field strength decreases the number of muons at the end. Figure 4.19 shows the muon fluxes at 1.2 T magnetic field for shielding. In this option, almost 3 ± 2 and 2 ± 1 muons come to the end of BDS for 40 m and 80 m shielding options, respectively.

Table 4.3. The estimated amount of muons reaching to the end of BDS depending on the magnetized muon shielding parameters by using halo distribution

Total Length of muon shielding	magnetic field	# of muons
40 m	0.7 T	11 ± 3
40 m	1.2 T	3 ± 2
80 m	0.7 T	6 ± 2
80 m	1.2 T	2 ± 1

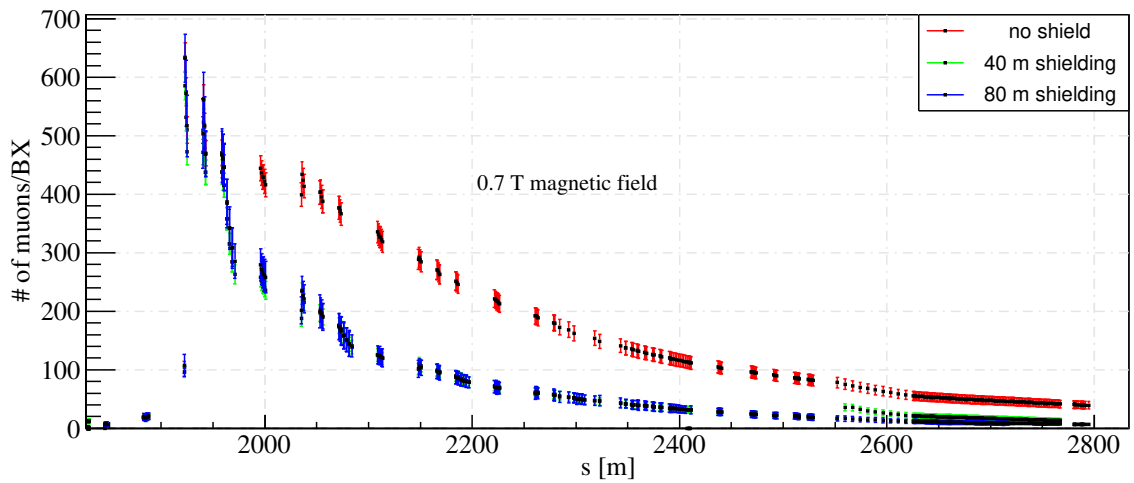


Figure 4.18. Muon fluxes for 0.7 T magnetized shielding when halo distribution, which is generated with HTGEN, is used.

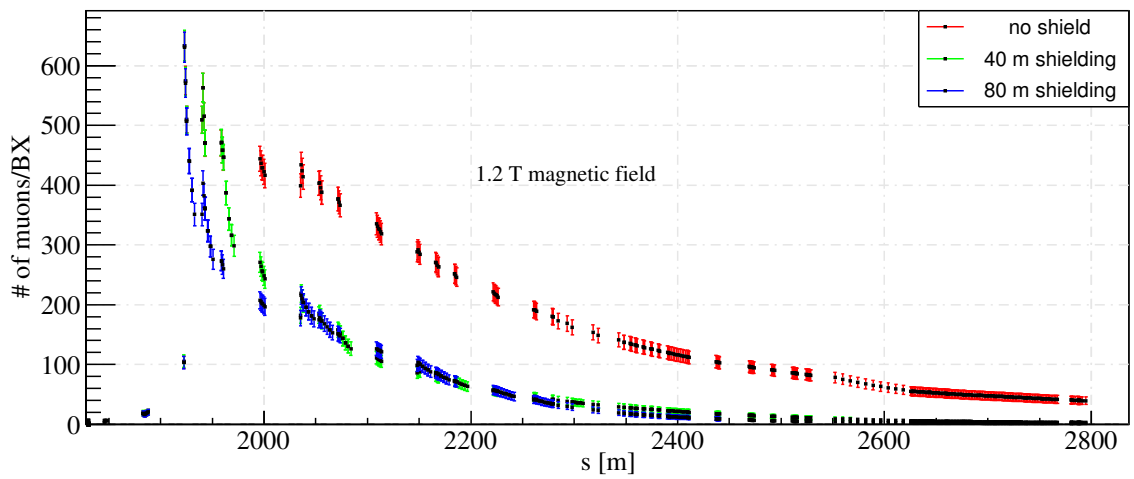


Figure 4.19. Muon fluxes for 1.2 T magnetized shielding when halo distribution, which is generated with HTGEN, is used.

5. CONCLUSION

The CLIC project has an innovative two beam acceleration system in order to collide electron and positrons up to 3 TeV center of mass energy. The last part of the acceleration system is the beam delivery system (BDS). The main interest of this work is in this part which is about 2.8 km long and transport beam from main linac to interaction region. The beam parameters of this part have been simulated with MAD-X. The all BDS line have been constructed with BDSIM and the particles tracks along the beam line have analysed.

The core beam may have halo particles around it while it is acceleration or transporting. Even in ideal conditions for a well corrected machine, there will always be a significant amount of beam halo generated by scattering on the residual gas in the system. The halo generation process have been performed with HTGEN code and the halo tracks in BDS and the amount of halo each elements on BDS have been performed by using HTGEN and PLACET codes together. Halo particles have higher amplitude than core particles. The halo particles have been removed from the core beam to obtain a clean collision at the interaction region. The betatron collimation section include collimators to remove halo particles around the core beam.

While halo particles are being cleaned from the core beam, they generate secondary particles including high energy muons. High energy muons lose little energy when they go through material, which makes them hard to stop such that they could reach the interaction region and deteriorate the physics potential for the detectors. The muon production mechanism and their tacks in BDS have been simulated by using GEANT4 and BDSIM codes. The muon rates on the BDS have been estimated.

Depending on the muon production rate and position, the magnetized muon shieldings have been designed and placed into the BDS. The muon reduction rates have been determined for different magnetized shielding parameters and they have been reported. The use of

magnetized shielding instead of tunnel fillers is more effective (both in performance and cost) to reduce background muons. We have obtained different reduction rates for different magnetized shielding options which have different parameter like thickness, magnetic field. The results of this study are important for the overall cost-performance optimization of the CLIC beam delivery system.

This muon background work is done for CLIC project which have been planned to built it at CERN. Besides, the simulation method of the background for accelerator will also give a support for future studies at Turkish Accelerator Center in Ankara. This study is also for more general importance for other high energy projects like in particular the Future Circular Collider (FCC) study at CERN in worldwide collaboration.

REFERENCES

Abramowicz, H., Abusleme, A., Afanaciev, K., Alexander, G., Alipour Tehrani, N., Alonso, O., Andersen, K. K., Arfaoui, S., Balazs, C., Barklow, T., Battaglia, M., Benoit, M., Bilki, B., Blaising, J.-J., Boland, M., Boronat, M., Božović Jelisavčić, I., Burrows, P., Chefdeville, M., Contino, R., Dannheim, D., Demarteau, M., Aurelio Diaz Gutierrez, M., Diéguez, A., Duarte Campderros, J., Eigen, G., Elsener, K., Feldman, D., Felzmann, U., Firlej, M., Firlu, E., Fiutowski, T., Francis, K., Gaede, F., García García, I., Ghenescu, V., Giudice, G., Graf, N., Grefe, C., Grojean, C., Gupta, R. S., Hauschild, M., Holmestad, H., Idzik, M., Joram, C., Kananov, S., Karyotakis, Y., Killenberg, M., Klempt, W., Kraml, S., Krupa, B., Kulis, S., Laštovička, T., LeBlanc, G., Levy, A., Levy, I., Linssen, L., Lucaci Timoce, A., Lukić, S., Makarenko, V., Marshall, J., Martin, V., Mikkelsen, R. E., Milutinović-Dumbelović, G., Miyamoto, A., Mönig, K., Moortgat-Pick, G., Moroń, J., Münnich, A., Neagu, A., Pandurović, M., Pappadopulo, D., Pawlik, B., Porod, W., Poss, S., Preda, T., Rassool, R., Rattazzi, R., Redford, S., Repond, J., Riemann, S., Robson, A., Roloff, P., Ros, E., Rosten, J., Ruiz-Jimeno, A., Rzehak, H., Sailer, A., Schlatter, D., Schulte, D., Sefkow, F., Seidel, K., Shumeiko, N., Sicking, E., Simon, F., Smith, J., Soldner, C., Stapnes, S., Strube, J., Suehara, T., Świentek, K., Szalay, M., Tanabe, T., Tesar, M., Thamm, A., Thomson, M., Trenado Garcia, J., Uggerhøj, U. I., van der Kraaij, E., Vila, I., Vilella, E., Villarejo, M. A., Alonso Vogel Gonzalez, M., Vos, M., Watson, N., Weerts, H., Wells, J. D., Weuste, L., Wistisen, T. N., Wootton, K., Xia, L., Zawiejski, L., Zgura, I.-S. 2013 Physics at the CLIC e+e- Linear Collider – Input to the Snowmass process 2013 *ArXiv e-prints* 1307.5288.

Agapov, I., Blair, G. A., Carter, J., Dadoun, O. 2006 BDSIM: Beamline simulation toolkit based on GEANT4 *Conf. Proc.* C060626 2212 [2212(2006)].

Agapov, I., Blair, G. A., Malton, S., Deacon, L. 2009 BDSIM: A particle tracking code for accelerator beam-line simulations including particle-matter interactions *Nucl. Instrum. Meth.* A606 708 doi:10.1016/j.nima.2009.04.040.

Agapov, I. V. 2006 GMAD Accelerator Description Language Tech. Rep. EUROTEV-MEMO-2006-003-1 EUROTeV URL <http://cds.cern.ch/record/972077>.

Agostinelli, S., Allison, J., Amako, K., Apostolakis, J., Araujo, H., Arce, P., Asai, M., Axen, D., Banerjee, S., Barrand, G., Behner, F., Bellagamba, L., Boudreau, J., Broglia, L., Brunengo, A., Burkhardt, H., Chauvie, S., Chuma, J., Chytráček, R., Cooperman, G., Cosmo, G., Degtyarenko, P., Dell'Acqua, A., Depaola, G., Dietrich, D., Enami, R., Feliciello, A., Ferguson, C., Fesefeldt, H., Folger, G., Foppiano, F., Forti, A., Garelli, S., Giani, S., Giannitrapani, R., Gibin, D., Cadenas, J. G., González, I., Abril, G. G., Greeniaus, G., Greiner, W., Grichine, V., Grossheim, A., Guatelli, S., Gumplinger, P., Hamatsu, R., Hashimoto, K., Hasui, H., Heikkinen, A., Howard, A., Ivanchenko, V., Johnson, A., Jones, F., Kallenbach, J., Kanaya, N., Kawabata, M., Kawabata, Y., Kawaguti, M., Kelner, S., Kent, P., Kimura, A., Kodama, T., Kokoulin, R., Kossov, M., Kurashige, H., Lamanna, E., Lampén, T., Lara, V., Lefebvre, V., Lei, F., Liendl, M., Lockman, W., Longo, F., Magni, S., Maire, M., Medernach, E., Minamimoto, K., de Freitas, P. M., Morita, Y., Mu-

rakami, K., Nagamatu, M., Nartallo, R., Nieminen, P., Nishimura, T., Ohtsubo, K., Okamura, M., O'Neale, S., Oohata, Y., Paech, K., Perl, J., Pfeiffer, A., Pia, M., Ranjard, F., Rybin, A., Sadilov, S., Salvo, E. D., Santin, G., Sasaki, T., Savvas, N., Sawada, Y., Scherer, S., Sei, S., Sirotenko, V., Smith, D., Starkov, N., Stoecker, H., Sulkimo, J., Takahata, M., Tanaka, S., Tcherniaev, E., Tehrani, E. S., Tropeano, M., Truscott, P., Uno, H., Urban, L., Urban, P., Verderi, M., Walkden, A., Wander, W., Weber, H., Wellisch, J., Wenaus, T., Williams, D., Wright, D., Yamada, T., Yoshida, H., Zschesche, D. 2003 Geant4—a simulation toolkit *Nuclear Instruments and Methods in Physics Research Section A: Accelerators, Spectrometers, Detectors and Associated Equipment* 506(3) 250 doi:[http://dx.doi.org/10.1016/S0168-9002\(03\)01368-8](http://dx.doi.org/10.1016/S0168-9002(03)01368-8) ISSN 0168-9002 URL <http://www.sciencedirect.com/science/article/pii/S0168900203013688>.

Aicheler, M., Burrows, P., Draper, M., Garvey, T., Lebrun, P., Peach, K., Phinney, N., Schmickler, H., Schulte, D., Toge, N. 2012 A Multi-TeV Linear Collider Based on CLIC Technology: CLIC Conceptual Design Report Tech. Rep. CERN-2012-007. SLAC-R-985. KEK-Report-2012-1. PSI-12-01. JAI-2012-001 Geneva URL <https://cds.cern.ch/record/1500095>.

Aloev, A., Burkhardt, H., Gatignon, L., Modena, M., Pilicer, B., Tapan, I. 2016 CLIC Muon Sweeper Design Tech. Rep. arXiv:1603.00005 comments: Talk presented at the International Workshop on Future Linear Colliders (LCWS15), Whistler, Canada, 2-6 November 2015, 7 pages, 6 figures URL <http://cds.cern.ch/record/2135570>.

Aloev, A., Modena, M. 2012 Preliminary Design of CLIC beam delivery System (CLIC BDS): Project Breakdown Structure (PBS): 4.1 Tech. Rep. CERN-OPEN-2013-028. CERN-ATS-Note-2012-097. CLIC-Note-984 CERN Geneva URL <https://cds.cern.ch/record/1615374>.

Aloev, A., Modena, M., Burkhardt, H. 2015 personal communication.

Baur, G., Leuschner, A. 1999 Bethe-Heitler cross-section for very high photon energies and large muon scattering angles *Eur. Phys. J. C* 8(hep-ph/9902245) 631 URL <http://cds.cern.ch/record/378582>.

BDSIM Collobration 2015 BDSIM Documentation Release 0.8.0 BDSIM.

Bettini, A. 2014 Introduction to elementary particle physics; 2nd ed. Cambridge University Press, Cambridge URL <https://cds.cern.ch/record/1611164>.

Bogdanov, A. G., Burkhardt, H., Ivanchenko, V. N., Kelner, S. R., Kokoulin, R. P., Maire, M., Rybin, A. M., Urban, L. 2006 Geant4 simulation of production and interaction of muons *IEEE Trans. Nucl. Sci.* 53 513 URL <http://cds.cern.ch/record/1020037>.

Boland, M. J., Felzmann, U., Giansiracusa, P. J., Lucas, T. G., Rassool, R. P., Balazs, C., Charles, T. K., Afanaciev, K., Emeliantchik, I., Ignatenko, A., Makarenko, V., Shumeiko, N., Patapenka, A., Zhuk, I., Abusleme Hoffman, A. C., Diaz Gutierrez, M. A., Gonzalez, M. V., Chi, Y., He, X., Pei, G., Pei, S., Shu, G., Wang, X., Zhang, J., Zhao, F., Zhou, Z., Chen, H., Gao, Y., Huang, W., Kuang, Y. P., Li, B., Li, Y.,

Shao, J., Shi, J., Tang, C., Wu, X., Ma, L., Han, Y., Fang, W., Gu, Q., Huang, D., Huang, X., Tan, J., Wang, Z., Zhao, Z., Laštovička, T., Uggerhoj, U., Wistisen, T. N., Aabloo, A., Eimre, K., Kuppert, K., Vigonski, S., Zadin, V., Aicheler, M., Baibuz, E., Brücken, E., Djurabekova, F., Eerola, P., Garcia, F., Haeggström, E., Huitu, K., Jansson, V., Karimaki, V., Kassamakov, I., Kyritsakis, A., Lehti, S., Meriläinen, A., Montonen, R., Niinikoski, T., Nordlund, K., Österberg, K., Parekh, M., Törnqvist, N. A., Väinölä, J., Veske, M., Farabolini, W., Mollard, A., Napoly, O., Peauger, F., Plouin, J., Bambade, P., Chaikovska, I., Chehab, R., Davier, M., Kaabi, W., Kou, E., LeDiberder, F., Pöschl, R., Zerwas, D., Aimard, B., Balik, G., Baud, J.-P., Blaising, J.-J., Brunetti, L., Chefdeville, M., Drancourt, C., Geoffroy, N., Jacquemier, J., Jeremie, A., Karyotakis, Y., Nappa, J. M., Vilalte, S., Vouters, G., Bernard, A., Peric, I., Gabriel, M., Simon, F., Szalay, M., van der Kolk, N., Alexopoulos, T., Gazis, E. N., Gazis, N., Ikarios, E., Kostopoulos, V., Kourkoulis, S., Gupta, P. D., Shrivastava, P., Arfaei, H., Dayyani, M. K., Ghasem, H., Hajari, S. S., Shaker, H., Ashkenazy, Y., Abramowicz, H., Benhammou, Y., Borysov, O., Kananov, S., Levy, A., Levy, I., Rosenblat, O., D'Auria, G., Di Mitri, S., Abe, T., Aryshev, A., Higo, T., Makida, Y., Matsumoto, S., Shidara, T., Takatomi, T., Takubo, Y., Tauchi, T., Toge, N., Ueno, K., Urakawa, J., Yamamoto, A., Yamanaka, M., Raboanary, R., Hart, R., van der Graaf, H., Eigen, G., Zalieckas, J., Adli, E., Lillestøl, R., Malina, L., Pflingstner, J., Sjobak, K. N., Ahmed, W., Asghar, M. I., Hoorani, H., Bugiel, S., Dasgupta, R., Firlej, M., Fiutowski, T. A., Idzik, M., Kopec, M., Kuczynska, M., Moron, J., Swientek, K. P., Daniluk, W., Krupa, B., Kucharczyk, M., Lesiak, T., Moszczyński, A., Pawlik, B., Sopicki, P., Wojtoń, T., Zawiejski, L., Kalinowski, J., Krawczyk, M., Żarnecki, A. F., Firu, E., Ghenescu, V., Neagu, A. T., Preda, T., Zgura, I.-S., Alov, A., Azaryan, N., Budagov, J., Chizhov, M., Filippova, M., Glagolev, V., Gongadze, A., Grigoryan, S., Gudkov, D., Karjavine, V., Lyablin, M., Olyunin, A., Samochkine, A., Sapronov, A., Shirkov, G., Soldatov, V., Solodko, A., Solodko, E., Trubnikov, G., Tyapkin, I., Uzhinsky, V., Vorozhtov, A., Levichev, E., Mezentsev, N., Piminov, P., Shatilov, D., Vobly, P., Zolotarev, K., Bozovic-Jelisavcic, I., Kacarevic, G., Lukic, S., Milutinovic-Dumbelovic, G., Pandurovic, M., Iriso, U., Perez, F., Pont, M., Trenado, J., Aguilar-Benitez, M., Calero, J., Garcia-Tabares, L., Gavela, D., Gutierrez, J. L., Lopez, D., Toral, F., Moya, D., Ruiz-Jimeno, A., Vila, I., Argyropoulos, T., Blanch Gutierrez, C., Boronat, M., Esperante, D., Faus-Golfe, A., Fuster, J., Fuster Martinez, N., Galindo Muñoz, N., García, I., Giner Navarro, J., Ros, E., Vos, M., Brenner, R., Ekelöf, T., Jacewicz, M., Ögren, J., Olvegård, M., Ruber, R., Ziemann, V., Aguglia, D., Alipour Tehrani, N., Alov, A., Andersson, A., Andrianala, F., Antoniou, F., Artoos, K., Atieh, S., Ballabriga Sune, R., Barnes, M. J., Barranco Garcia, J., Bartosik, H., Belder-Aguilar, C., Benot Morell, A., Bett, D. R., Bettoni, S., Blanchot, G., Blanco Garcia, O., Bonnin, X. A., Brunner, O., Burkhardt, H., Calatroni, S., Campbell, M., Catalan Lasheras, N., Cerqueira Bastos, M., Cherif, A., Chevally, E., Constance, B., Corsini, R., Cure, B., Curt, S., Dalena, B., Dannheim, D., De Michele, G., De Oliveira, L., Deelen, N., Delahaye, J. P., Dobers, T., Doebert, S., Draper, M., Duarte Ramos, F., Dubrovskiy, A., Elsener, K., Esberg, J., Esposito, M., Fedosseev, V., Ferracin, P., Fiergolski, A., Foraz, K., Fowler, A., Friebel, F., Fuchs, J.-F., Fuentes Rojas, C. A., Gaddi, A., Garcia Fajardo, L., Garcia Morales, H., Garion, C., Gatignon, L., Gayde, J.-C., Gerwig,

H., Goldblatt, A. N., Greife, C., Grudiev, A., Guillot-Vignot, F. G., Gutt-Mostowy, M. L., Hauschild, M., Hessler, C., Holma, J. K., Holzer, E., Hourican, M., Hynds, D., Inntjore Levinsen, Y., Jeanneret, B., Jensen, E., Jonker, M., Kastriotou, M., Kempainen, J. M. K., Kieffer, R. B., Klempt, W., Kononenko, O., Korsback, A., Koukovini Platia, E., Kovermann, J. W., Kozsar, C.-I., Kremastiotis, I., Kulis, S., Latina, A., Leaux, F., Lebrun, P., Lefevre, T., Linssen, L., Llopart Cudie, X., Maier, A. A., Mainaud Durand, H., Manosperti, E., Marelli, C., Marin Lacoma, E., Martin, R., Mazzoni, S., Mcmonagle, G., Mete, O., Mether, L. M., Modena, M., Munker, R. M., Muranaka, T., Nebot Del Busto, E., Nikiforou, N., Nisbet, D., Nonglaton, J.-M., Nuiry, F. X., Nürnberg, A., Olvegard, M., Osborne, J., Papadopoulou, S., Papaphilippou, Y., Passarelli, A., Patecki, M., Pazdera, L., Pellegrini, D., Pepitone, K., Perez, F., Perez Codina, E., Perez Fontenla, A., Persson, T. H. B., Petrič, M., Pitters, F., Pittet, S., Plassard, F., Rajamak, R., Redford, S., Renier, Y., Rey, S. F., Riddone, G., Rinolfi, L., Rodriguez Castro, E., Roloff, P., Rossi, C., Rude, V., Rumolo, G., Sailer, A., Santin, E., Schlatter, D., Schmickler, H., Schulte, D., Shipman, N., Sicking, E., Simoniello, R., Skowronski, P. K., Sobrino Mompean, P., Soby, L., Sosin, M. P., Sroka, S., Stapnes, S., Sterbini, G., Ström, R., Syratheev, I., Tecker, F., Thonet, P. A., Timeo, L., Timko, H., Tomas Garcia, R., Valerio, P., Vamvakas, A. L., Vivoli, A., Weber, M. A., Wegner, R., Wendt, M., Woolley, B., Wuensch, W., Uythoven, J., Zha, H., Zisopoulos, P., Benoit, M., Vicente Barreto Pinto, M., Bopp, M., Braun, H. H., Csatari Divall, M., Dehler, M., Garvey, T., Raguin, J. Y., Rivkin, L., Zennaro, R., Aksoy, A., Nergiz, Z., Pilicer, E., Tapan, I., Yavas, O., Baturin, V., Kholodov, R., Lebedynskyi, S., Miroshnichenko, V., Mordyk, S., Profatlova, I., Storizhko, V., Watson, N., Winter, A., Goldstein, J., Green, S., Marshall, J. S., Thomson, M. A., Xu, B., Gillespie, W. A., Pan, R., Tyrk, M. A., Protopopescu, D., Robson, A., Apsimon, R., Bailey, I., Burt, G., Constable, D., Dexter, A., Karimian, S., Lingwood, C., Buckland, M. D., Casse, G., Vosseveld, J., Bosco, A., Karataev, P., Kruchinin, K., Lekomtsev, K., Nevay, L., Snuverink, J., Yamakawa, E., Boisvert, V., Boogert, S., Boorman, G., Gibson, S., Lyapin, A., Shields, W., Teixeira-Dias, P., West, S., Jones, R., Joshi, N., Bodenstern, R., Burrows, P. N., Christian, G. B., Gamba, D., Perry, C., Roberts, J., Clarke, J. A., Collomb, N. A., Jamison, S. P., Shepherd, B. J. A., Walsh, D., Demarteau, M., Repond, J., Weerts, H., Xia, L., Wells, J. D., Adolphsen, C., Barklow, T., Breidenbach, M., Graf, N., Hewett, J., Markiewicz, T., McCormick, D., Moffeit, K., Nosochkov, Y., Oriunno, M., Phinney, N., Rizzo, T., Tantawi, S., Wang, F., Wang, J., White, G., Woodley, M. (CLIC and CLICdp collaborations) **2016** Updated baseline for a staged Compact Linear Collider Tech. Rep. CERN-2016-004. CERN-2016-004 Geneva comments: 57 pages, 27 figures, 12 tables URL <https://cds.cern.ch/record/2210892>.

Brugger, M., Burkhardt, H., Goddard, B. 2013 Interactions of Beams With Surroundings *Landolt-Börnstein* 21C 5 URL <https://cds.cern.ch/record/1625153>.

Burkhardt, H., Kelner, S. R., Kokoulin, R. P. 2002a Monte Carlo Generator for Muon Pair Production Tech. Rep. CERN-SL-2002-016-AP. CLIC-Note-511 CERN Geneva URL <http://cds.cern.ch/record/558831>.

Burkhardt, H., Neukermans, L., Latina, A., Schulte, D., Agapov, I., Blair, G. A., Jackson, F. 2007 Halo estimates and simulations for linear colliders Proceeding of

PAC07, Albuquerque, New Mexico, USA.

Burkhardt, H., et al 2002b Monte carlo generator for muon pair production *CERN-SL-2002-016 (AP) CLIC Note 511* URL <http://cds.cern.ch/record/558831/files/sl-2002-016.pdf>.

Butler, J., Contardo, D., Klute, M., Mans, J., Silvestris, L., on behalf of the CMS, C. (CMS Collaboration) 2015 CMS Phase II Upgrade Scope Document Tech. Rep. CERN-LHCC-2015-019. LHCC-G-165 CERN Geneva URL <http://cds.cern.ch/record/2055167>.

CERN 2002 Methodical Accelerator Design (MAD) tool by BE/ABP - Accelerator Beam Physics Group <http://mad.web.cern.ch/mad/> Accessed: 2017-04-15.

Courant, E. D., Snyder, H. S. 1958 Theory of the Alternating-Gradient Synchrotron *Ann. Phys.* 3 1 URL <https://cds.cern.ch/record/593259>.

Deacon, L., Blair, G. A., Burkhardt, H. 2012 Muon Background Reduction in CLIC in International Workshop on Future Linear Colliders (LCWS11) Granada, Spain, September 26-30, 2011 1202.6628 URL <http://inspirehep.net/record/1091078/files/arXiv:1202.6628.pdf>.

Di Domenico, A. 1991 Inverse Compton scattering of thermal radiation at LEP and LEP-200 *Part. Accel.* 39(CERN-PPE-91-144) 137 URL <https://cds.cern.ch/record/225610>.

Elsener, K. 2015 personal communication with H. Burkhardt.

Fitterer, M., Baumbach, T., Burkhardt, H., Müller, A.-S., Quast, G. 2009 Modelling of Halo and Tail Generation in Electron Beams Ph.D. thesis Karlsruhe U., Karlsruhe presented 24 Sep 2009 URL <http://cds.cern.ch/record/1552341>.

Gaillard, M. 1985 Book review *Foundations of Physics* 15(2) 243 doi:10.1007/BF00735298 ISSN 0015-9018 URL <http://dx.doi.org/10.1007/BF00735298>.

Griffiths, D. J. 1987 Introduction to Elementary Particles TextBook Physics Wiley, New York, NY URL <https://cds.cern.ch/record/1260972>.

HL 2016 High Luminosity LHC <http://hilumilhc.web.cern.ch/> Accessed: 2016-04-10.

Ijaz Ahmed, Helmut Burkhardt, M. F. 2008 User Manual for the Halo and Tail generator HTGEN EuroTeV.

Keller, L. P. 1993 Muon background in a 1-TeV linear collider in 5th International Workshop on Next-Generation Linear Colliders Stanford, California, October 13-21, 1993 URL <http://www-public.slac.stanford.edu/sciDoc/docMeta.aspx?slacPubNumber=SLAC-PUB-6385>.

Kelner, S. R., Kokoulin, R. P., Petrukhin, A. A. 1995 About cross-section for high-energy muon bremsstrahlung .

- Lee, S. Y. 2012** Accelerator physics; 3rd ed. World Scientific, Singapore URL <https://cds.cern.ch/record/1425444>.
- Linssen, L., Miyamoto, A., Stanitzki, M., Weerts, H. 2012** Physics and Detectors at CLIC: CLIC Conceptual Design Report *ArXiv e-prints* 1202.5940.
- Lukić, S. (FCAL) 2015** Physics highlights at ILC and CLIC in Proceedings, 12th International School-Seminar on The Actual Problems of Microworld Physics. Vol.1: Gomel, Belarus, July 22 - September 28, 2013 vol. 1 39–53 1406.4313 URL <https://inspirehep.net/record/1300818/files/arXiv:1406.4313.pdf>.
- Murayama, H. 1995** Physics prospects: Why do we want a linear collider? in Physics and experiments with linear colliders. Proceedings, 3rd Workshop, Morioka-Appi, Japan, September 8-12, 1995. Vol. 1, 2 1–23 hep-ex/9606001.
- Murayama, H., Peskin, M. E. 1996** Physics opportunities of e+ e- linear colliders *Ann.Rev.Nucl.Part.Sci.* 46 533 doi:10.1146/annurev.nucl.46.1.533 hep-ex/9606003.
- Nghiem, P., Chauvin, N., Uriot, D., W., S. 2012** Beam Halo Definitions and its Consequences <https://accelconf.web.cern.ch/accelconf/HB2012/papers/tho3a04.pdf>.
- Olive, K. A., et al (Particle Data Group) 2014** Review of Particle Physics *Chin. Phys.* C38 090001 doi:10.1088/1674-1137/38/9/090001.
- OPERA 2016** Magnet design software <http://operafea.com/home-page/>.
- Physics Reference Manual 2013** GEANT4 : Physics Reference Manual CERN Program Library Long Writeups URL <http://geant4.web.cern.ch/geant4/UserDocumentation/UsersGuides/PhysicsReferenceManual/fo/PhysicsReferenceManual.pdf>.
- Schopper, H. F., Myers, S. 2013** Elementary particles Landolt-Börnstein. New series. Group 1 Elementary particles, nuclei and atoms Springer, Berlin URL <https://cds.cern.ch/record/1593302>.
- Schulte, D. 2000** PLACET: a Program to Simulate Drive Beams *Particle Accelerator Conference, 2001. PAC 2001. Proceedings of the 2001* URL <https://cds.cern.ch/record/447689>.
- Siegrist, N. and Gerwig H. 2015** First look at a single CLIC detector in 3D Presented at MDI Meeting, CERN.
- Telnov, V. I. 1987** Scattering of Electrons on Thermal Radiation Photons in Electron - Positron Storage Rings *Nucl. Instrum. Meth.* A260 304 doi:10.1016/0168-9002(87)90093-3.
- Tsai, Y.-S. 1974** Pair production and bremsstrahlung of charged leptons *Review of Modern Physics* 46 815.
- Wiedemann, H. 2007** Particle accelerator physics in Particle accelerator physics; 3rd ed. Springer, Berlin chap. 5, 154–201.

APPENDICES

APPENDIX 1	Description of elements in BDS with GMAD format
APPENDIX 2	Beam parameters and some other parameters



APPENDIX 1

Description of elements in BDS with GMAD format;

```
SD4_1: sextupole, l=0.40739568*m, k2=-18.855199822, aper=0.00415*  
m, outR=416*1e-3*m;  
DRIFT_53_2: drift, l=0.24841166*m, aper=0.00404*m;  
QD4A: quadrupole, l=0.807339*m, k1=0.0186097700966, aper=0.00404*  
m, outR=208*1e-3*m;  
QD4A_1: quadrupole, l=0.807339*m, k1=0.0186097700966, aper  
=0.00404*m, outR=208*1e-3*m;  
DRIFT_55: drift, l=23.5748875*m;  
SFFB3: sbend, l=7.328154*m, angle=1.929415e-05, aper=0.00364*m,  
outR=88*1e-3*m;
```

APPENDIX 2

Beam parameters and some other parameters at starting point of the BDS in BDSIM code;

```
beam, distrType="gausstwiss",
      particle="e-",
      energy=1500.0*GeV,
      betx=66.14*m,
      bety=17.92*m,
      alfy=0.0*m,
      alfx=0.0*m,
      emitx=2.25e-13,
      emity=6.81e-15;

option, beampipeRadius = 8* mm, ! default drift radius
      boxSize = 0.5 * m,      ! outer radius of elements or set
      different for each element using outR parameter
      beampipeThickness = 0.2 *mm;

option, buildTunnel=1,
      buildTunnelStraight=1,
      tunnelType="circular",
      tunnelThickness=0.5*m,
      tunnelSoilThickness=6.5*m,
      tunnelMaterial="concrete",
      soilMaterial="soil",
      tunnelSensitive=1,
      tunnelAper1=3.0*m,
      tunnelAper2=3.0*m,
      buildTunnelFloor=0;
```

```
! tunnelSensitive=1, ! use with v0.8 and upper versions
! tunnelVisible=1, ! use with v0.8 and upper versions
  tunnelOffsetX=0.497*m,
  tunnelOffsetY=0.8*m,
! magnetGeometryType="cylindrical"; ! use with v0.8 and upper
versions
! magnetGeometryType="polescircular";! another type of
magnet geometry
```



CURRICULUM VITAE

Name Surname : Fatma Belgin PİLİÇER
Brith Place and Date : Zonguldak - 19.11.1987
Foreign Language : English
e-mail : belginpilicer@gmail.com, fatma.belgin.pilicer@cern.ch
Bachelor Degree : Abant İzzet Baysal University
Science - Art Faculty - Physics - 2009
Master Degree : Abant İzzet Baysal University
Institute of Natural and Applied Science - Physics - 2011

Experiences

- Radiation Hardness Tests with Laser, as a researcher, 28 January 2011, MAPRad, Perugia, Italy.
- Radiation Hardness Tests with Ion Beam, as a researcher, 1-5 February 2011, Istituto Nazionale Fisica Nucleare Laboratori Nazionali del Sud INFN, Catania, Italy.
- Muon Background Studies for CLIC project, as a researcher , September- December 2013, CERN, Geneve, Switzerland.
- Muon Background Studies on CLIC Beam Delivery Systems, for doctoral research, 14 September 2014 -14 September 2015, (TUBITAK 2214 Scholarship), CERN, Geneve, Switzerland.
- Laser Diode Systems and Their Optics Simulations, ERMAKSAN, High Technology R&D Center Optoelectronic Department, as a R&D Engineer, February – July, 2016, Bursa, Turkey.

Publications

- **F. B. Ergin**, R. Turan, S. T. Shishiyanu, E. Yilmaz “Effect of γ - radiation on HfO₂ based MOS capacitor”, Nuclear Instruments and Methods in Physics Research B vol.268, 1482–1485, 2010, DOI: 10.1016/j.nimb.2010.01.027.
- I. Tapan , **F. B. Pilicer**, “Silicon tracker simulation for the Turkish Accelerator Center Particle factory”, Nuclear Instruments and Methods in Physics Research Section A, 765, 240-243, 2014, DOI: 10.1016/j.nima.2014.05.100.
- **F. B. Pilicer**, H. Burkhardt, L. Gagnon, A. Latina, E. Pilicer, D. Schulte, İ. Tapan, and R. Tomas “Study of Muon Backgrounds in the CLIC Beam Delivery System”, in Proc. 6th International Particle Accelerator Conference, Richmond, VA, USA, paper TUPTY032, pp. 2075-2078, 2015.
- I. Tapan, E. Pilicer, **F.B. Pilicer** “Tracking parameter simulation for the Turkish accelerator center particle factory tracker system”, Nuclear Instruments and Methods in Physics Research Section A, 831, 389-393, 2016, DOI: 10.1016/j.nima.2016.04.064.
- E.E. Ermis, **F.B. Pilicer**, E. Pilicer, C. Celiktas “A comprehensive study for mass attenuation coefficients of different parts of the human body through Monte Carlo

methods”, Nuclear Science and Techniques. 27(3) , 1-9, 2016, DOI: 10.1007/s41365-016-0053-2.

- E. Pilicer, F. Kocak, A. Kilic, **F.B. Pilicer**, I. Tapan, “Radiation Effects of TAC-PF Electromagnetic Calorimeter”, Acta Physica Polonica, vol.131, 2017, DOI: 10.12693/APhysPolA.131.190.

